

MIXING AND TIME-DEPENDENT CP ASYMMETRIES IN E^+E^- ANNIHILATION

David B. MacFarlane*
University of California at San Diego
La Jolla, CA 92093-0319

ABSTRACT

This set of lectures is intended as an overview of the recent results from B Factory experiments on time-dependent CP asymmetries in B decays. They begin with a review of the basic requirements of such measurements, and the related studies of B lifetimes and B^0 - \bar{B}^0 mixing. A brief tour of the PEP-II and KEKB facilities and the $BABAR$ and Belle detectors is provided. We will examine the basic components of time-evolution measurements: exclusive reconstruction of B mesons, determination of the proper time difference between the decays of the two B mesons in the $\Upsilon(4S)$ events, and tagging the flavor of the b quark at the time of its decay. Armed with an understanding of these elements of the time-development analyses, we proceed to examine the latest measurements of lifetime, mixing, and mixing-induced CP violation in charmonium modes. These studies have led to the discovery of large amplitudes for CP violation in neutral B decays, as evidenced by the distinctly different time evolution of matter and anti-matter tagged B decays at $BABAR$ and Belle. The lectures conclude with a snapshot of the evolution of data samples and projected sensitivity at the B Factories over the next few years.

*Supported by DOE Contract DOE-FG03-97ER40546.

1 Introduction

CP violation has been a central concern of particle physics since its discovery in 1964.¹ Interest was heightened by Sakharov's observation² in 1967 that without CP violation, a universe that began as matter–anti-matter symmetric could not have evolved into the asymmetric one we now see. An elegant explanation of the CP -violating effects in K_L^0 decays is provided by the CP -violating phase of the three-generation Cabibbo-Kobayashi-Maskawa (CKM) quark-mixing matrix.³ However, existing studies of CP violation in neutral kaon decays and the resulting experimental constraints on the parameters of the CKM matrix⁴ do not provide a stringent test of whether the CKM phase describes CP violation.⁵ Moreover, the Standard Model does not, through the CKM phase, incorporate enough CP violation to explain the current matter–anti-matter asymmetry.⁶ Understanding CP violation thus remains a pressing challenge.

1.1 Seeds of an idea

With only the one observed instance of CP violation in neutral K decays, it is difficult to confront these fundamental questions. However, the experimental opportunities for further exploration of CP violation expanded dramatically following the discovery of the b quark in 1977⁷ and a series of new experiments were mounted to study its weak interaction properties. In particular, two key results emerged from this experimental work, which were quite surprising at the time. Nevertheless, they set the stage for a new round of CP violation studies at asymmetric-energy $e^+e^- B$ Factories.

In 1983, both MAC⁸ and Mark II⁹ reported measurements of b quark lifetimes. Using events with leptons at high- p_T with respect to the jet thrust axis to obtain event samples enriched in b decays, the two experiments studied the distribution of impact parameters with respect to the interaction point, reproduced in Figure 1, to determine average lifetimes τ_b of $(1.8 \pm 0.6 \pm 0.4)$ and $(1.2 \pm 0.4 \pm 0.3)$ respectively. The data available to the two experiments represented an integrated luminosity of about 100 pb^{-1} , recorded at a center-of-mass of 29 GeV, or equivalently about 3500 produced $b\bar{b}$ pairs. The final analysis samples consisted of about 300 high- p_T lepton candidates for each experiment. The lifetime results showed that the V_{cb} element of the CKM matrix was quite small and indeed was the basis for the empirical Wolfenstein parameterization¹⁰ that is commonly used. The implied suppression of the b decay rate by $\sin^2 \theta_C \sim \lambda^2$ suggested that other rare decays may be important and experimentally accessible.

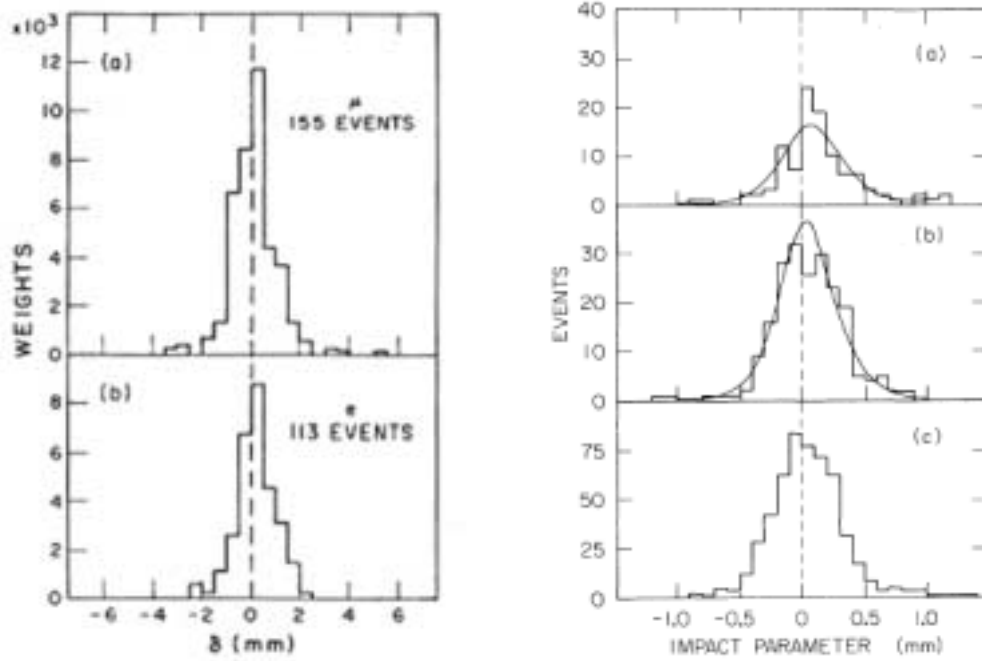


Fig. 1. First measurements of B lifetimes by MAC (left) and Mark II (right). For MAC, the distribution of signed impact parameter with respect to the interaction point is shown for high- p_T muons (a) and electrons (b). For Mark II, the combined high- p_T lepton impact parameter distributions are shown for a charm enriched region (a), a b enriched region (b), and for high- p_T hadrons as the dominant background source due to hadron misidentification.

While these first measurements of the b lifetime were being pursued by the PEP and PETRA experiments, the bulk of our basic knowledge of the b quark has come from the CLEO and CUSB experiments at Cornell and ARGUS and Crystal Ball at DESY. Perhaps the most surprising of these results was the discovery of B^0 - \bar{B}^0 mixing by ARGUS in 1987.¹¹ The observation consisted of three parts, all based on time-integrated techniques with a data sample equivalent to 103 pb^{-1} or 110000 produced $B\bar{B}$ meson pairs accumulated from 1983-1987. The first evidence was an excess of $24.8 \pm 7.3 \pm 3.8$ like-sign dilepton candidates over known background sources (50 candidates were seen in total), compared to about 270 opposite-sign dilepton events. On the $\Upsilon(4S)$, the additional constraint of the two-body final state allows one to reconstruct exclusive semileptonic decays by inference if the recoil mass against the charm hadron and observed lepton system is consistent with zero. ARGUS found 5 candidates (0.9

background) where the reconstructed semileptonic B meson had the same flavor as tagged by a lepton from the second B decay. Finally, in this same sample they were able to fully reconstruct the second B in the event, once again in a semileptonic channel. This event, shown in Figure 2, contains two reconstructed B^0 mesons, both seen in the channel $B^0 \rightarrow D^{*-}\pi^+\nu$. The large rate for B^0 - \bar{B}^0 mixing

$$\frac{\Gamma(B^0 \rightarrow \bar{B}^0 \rightarrow X')}{\Gamma(B^0 \rightarrow X)} = 0.21 \pm 0.08$$

came as a surprise in an era when the top quark was widely expected to have a mass around $30 \text{ GeV}/c^2$. More importantly, it implied that ideas for exploration of CP violation through interference of mixing and direct decay diagrams¹² might be experimentally feasible and, indeed, an excellent testing ground for the Standard Model picture of CP violation created by phases in the CKM matrix.



Fig. 2. An example of B^0 - \bar{B}^0 mixing from the original ARGUS observation, showing an $\Upsilon(4S)$ decay reconstructed as $B^0 B^0$.

Due to particle–anti-particle mixing, a particle that is purely B^0 at time $t = 0$ will oscillate between that state and \bar{B}^0 with a frequency Δm_d , the difference between the

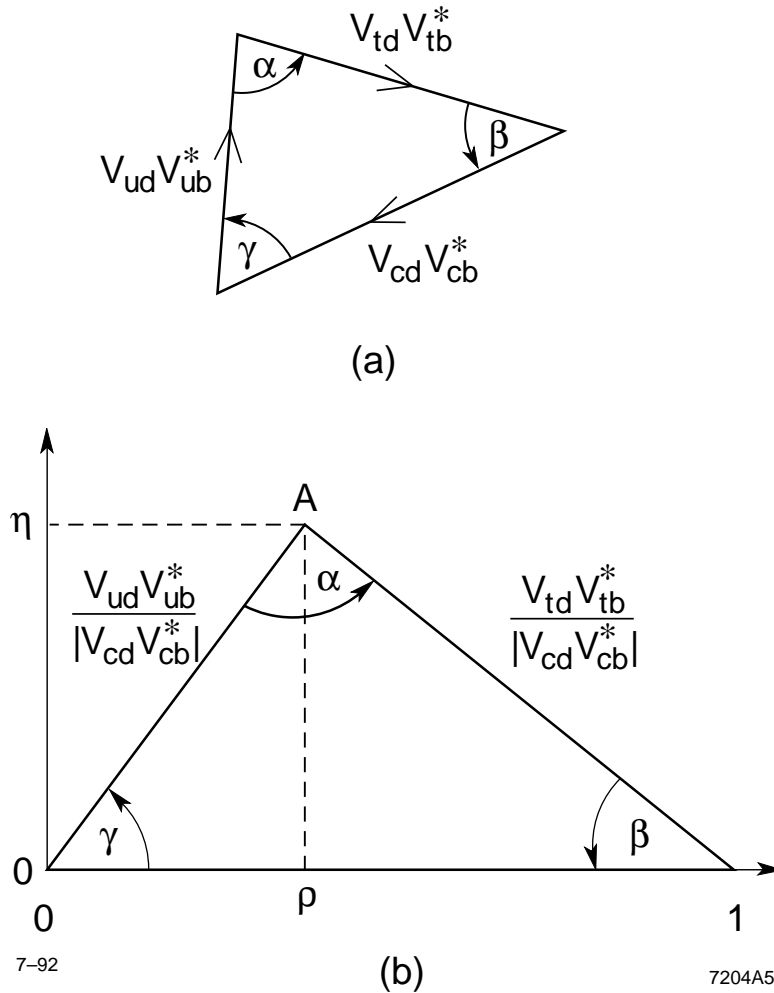


Fig. 3. Geometric representation in the complex plane of the unitarity relation from the CKM matrix most relevant for b decays.

masses of the two neutral B mass eigenstates. If decays to a CP eigenstate f are observed, any difference between the rates when starting with a B^0 or with a \bar{B}^0 is a manifestation of CP violation. In some circumstances, including those in the experiments described in these lectures, the fundamental parameters of CP violation in the CKM model can be measured from such time-dependent rate asymmetries, unobscured by strong interactions. For example, a state initially produced as a B^0 (\bar{B}^0) can decay to $J/\psi K_S^0$ directly or can oscillate into a \bar{B}^0 (B^0) and then decay to $J/\psi K_S^0$. With little theoretical uncertainty in the Standard Model, the phase difference between these amplitudes is equal to twice the angle $\beta = \arg[-V_{cd}V_{cb}^*/V_{td}V_{tb}^*]$ of the Unitarity Triangle.

The CP -violating asymmetry can thus provide a crucial test of the Standard Model.

The unitarity of the three-generation CKM matrix can be expressed in geometric form by six triangles of equal area in the complex plane. A nonzero area¹³ directly implies the existence of a CP -violating CKM phase. The most experimentally accessible of the unitarity relations, involving the two smallest elements of the CKM matrix, V_{ub} and V_{td} , has come to be known as the b quark Unitarity Triangle and is illustrated in Figure 3. Because the lengths of the sides of the Unitarity Triangle are comparable, the angles can be large, leading to potentially large CP -violating asymmetries from relative phases between CKM matrix elements.

Table 1. Predicted luminosity requirements for CP asymmetry measurement at an asymmetric-energy e^+e^- collider, as reported by the Snowmass summer study in 1988. At the time, the expectation for $\sin 2\beta$ ranged from 0.05 to 0.3. Integrated luminosity is reported in terms of \mathcal{L}_{peak} at full efficiency for 10^7 sec, i.e., accounts roughly for typically downtimes and running efficiencies.

Factor	Estimate
$\sigma(b\bar{b})$	1.1 nb
B^0 fraction	0.43
Reconstruction efficiency	0.61
Tagging efficiency	0.48
Wrong-tag fraction	0.08
Dilution	0.61
Required luminosity	$0.45\text{--}16 \times 10^{40} \text{ cm}^{-2}$

The prospect of large CP asymmetries in neutral B decays with, in many cases, well-controlled theoretical uncertainties created worldwide interest in devising experiments that could incisively test these ideas. There are a variety of usable sources of B mesons, with a range of sample purities, production rates, kinematic characteristics, and tagging prospects. One early look at the experimental options was undertaken at the Snowmass Summer Study in 1988.¹⁴ They examined a range of possible experiments, including e^+e^- collisions at the $b\bar{b}$ threshold or at the Z^0 , as well as fixed target and hadron colliders. Their conclusion was that asymmetric energy e^+e^- collisions at the center-of-mass energy of the $\Upsilon(4S)$ offered both a feasible technique for time-dependent CP asymmetry measurements and the best sensitivity of the available op-

tions. The requirements for the experiment looked daunting, but the study reproduced in Table 1 showed that a collider operating with peak luminosity of $3 \times 10^{33} \text{ cm}^{-2}\text{s}^{-1}$ could reasonably expect to observe CP violation over the entire range predicted within the Standard Model.

Five years later, the seeds planted on the basis of these early measurements and ideas bore fruit when both the PEP II and KEKB asymmetric-energy colliders were approved for construction at SLAC and KEK.

1.2 $\Upsilon(4S)$ as a coherent $B\bar{B}$ source

Much of what we know about B mesons comes from experiments that operate in e^+e^- storage rings near the threshold for $b\bar{b}$ production. The visible annihilation cross section for production of multihadron events is shown as a function of center-of-mass energy in Figure 4. Three narrow resonances the $\Upsilon(1S)$, $\Upsilon(2S)$, and $\Upsilon(3S)$ are visible, with widths dominated by the spread of the beam energies. The much broader $\Upsilon(4S)$ lies above the threshold for decays into $B\bar{B}$ meson pairs, and represents the most favorable source for B meson studies in terms of signal-to-background ratio. Table 2 lists the cross sections for $e^+e^- \rightarrow q\bar{q}$ at the $\Upsilon(4S)$ center-of-mass energy of 10.58 GeV.

In e^+e^- storage rings operating at the $\Upsilon(4S)$ resonance, a $B^0\bar{B}^0$ pair produced in an $\Upsilon(4S)$ decay evolves in a coherent P -wave state. If one of the B mesons, referred to as B_{tag} , can be ascertained to decay to a state of known flavor, *i.e.* B^0 or \bar{B}^0 , at a certain time t_{tag} , the other B , referred to as B_{rec} , *at that time* must be of the opposite flavor as a consequence of Bose symmetry. Consequently, the oscillatory probabilities for observing $B^0\bar{B}^0$, B^0B^0 and $\bar{B}^0\bar{B}^0$ pairs produced in $\Upsilon(4S)$ decays are a function of $\Delta t = t_{\text{rec}} - t_{\text{tag}}$, allowing mixing frequencies and CP asymmetries to be determined if Δt is known. The charges of identified leptons and kaons are the primary indicators of the flavor of the tagging B , but other particles also carry flavor information that can be exploited with a neural network algorithm. The reconstructed neutral B is found either in a flavor eigenstate ($B_{\text{rec}} = B_{\text{flav}}$) or a CP mode ($B_{\text{rec}} = B_{CP}$) by full reconstruction of its observed long-lived daughters.

At the asymmetric e^+e^- colliders, resonant production of the $\Upsilon(4S)$ provides a copious source of $B^0\bar{B}^0$ pairs moving along the beam axis (z direction) with an average Lorentz boost $\langle\beta\gamma\rangle$. Therefore, the proper decay-time difference Δt is, to an excellent approximation, proportional to the distance Δz between the two B^0 -decay vertices along the axis of the boost, $\Delta t \approx \Delta z/c \langle\beta\gamma\rangle$. For example, with an average

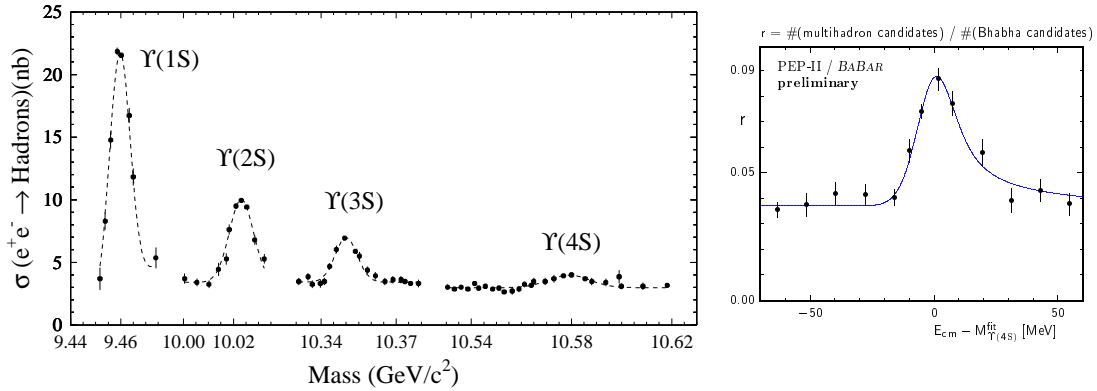


Fig. 4. Original CUSB¹⁵ scan (left) of the visible hadronic cross section in the region of 10 GeV in the center of mass, showing the three narrow $\Upsilon(1S)$, $\Upsilon(2S)$, and $\Upsilon(3S)$ resonances below the open beauty threshold and the $\Upsilon(4S)$, which decays into $B\bar{B}$ meson pairs. A recent BABAR scan (right) of the $\Upsilon(4S)$ resonance alone.

Table 2. Cross section components for production of multihadron events at the $\Upsilon(4S)$.

Component	Cross section [nb]
$b\bar{b}$	1.1
$c\bar{c}$	1.3
$d\bar{d}, s\bar{s}$	0.3
$u\bar{u}$	1.4

boost of $\langle\beta\gamma\rangle = 0.55$. the average separation between the two B decay vertices at BABAR is $\Delta z = \langle\beta\gamma\rangle c\tau_B = 260 \mu\text{m}$, while the RMS Δz resolution of the detector is about $180 \mu\text{m}$. At Belle, the beam energies are somewhat less asymmetric, leading to a smaller average boost of $\langle\beta\gamma\rangle = 0.425$ and decay vertex separation of $\sim 200 \mu\text{m}$. These distances are large enough to allow measurement with a precision that is sufficient to time resolve the order of the tagging and reconstructed B meson decays, which is a crucial ingredient of the CP asymmetry studies.

1.3 Measurement of B lifetimes

As already noted, one of the first surprises that emerged from measurements of the weak interaction properties of the b quark was its long lifetime. This reflects the relatively

small size of the V_{cb} element of the CKM matrix and forms the basis for the empirical Wolfenstein representation.

The simple spectator quark model predicts that the two charge states of a heavy flavor meson with one heavy quark Q ($Q\bar{u}$ and $Q\bar{d}$) have the same lifetime. In the charm sector this picture of decays dominated by simple spectator diagrams is not adequate; the lifetimes of the charged and neutral D meson differ by It is thought that other processes, such as weak annihilation or W exchange, or final-state rescattering, have an appreciable impact. However, the spectator model is expected to hold much better in the bottom sector since the b quark is significantly heavier than the c quark. In particular, deviations from this simple picture are expected to be proportional to $1/m_Q^2$.^{16,17} Therefore, any lifetime differences are anticipated to be much smaller for mesons containing b quarks. Indeed, various models^{16,17} predict that the the B^+ and B^0 meson lifetimes should be same to within about to 10%.

Since the initial measurements by MAC and Mark II, increasingly more precise results have become available, particularly from experiments operating near the Z and at the hadron colliders. Prior to contributions from the B Factory experiments, the world averages for the B^0 and B^+ meson lifetimes and their ratio were determined¹⁸ to be $\tau_{B^0} = 1.548 \pm 0.032$ ps; $\tau_{B^+} = 1.653 \pm 0.028$ ps; $\tau_{B^+}/\tau_{B^0} = 1.062 \pm 0.029$.

For most previous lifetime measurements, the point of origin of the b quark is defined by the interaction point. Therefore, the experimental distribution is simply a single-sided exponential distribution convolved with a nearly Gaussian experimental resolution function. Such a situation is illustrated in the upper two panels of Figure 5, where it is evident that the resolution function can be determined from the distribution of events at negative times, allowing a relatively clean separation of lifetime and resolution effects.

At the B Factory experiments, one of the B mesons in an event, denoted B_{rec} , can be fully reconstructed in a variety of two-body charm and charmonium final states. The decay point of the other B in the event, denoted B_{tag} , can be reconstructed inclusively. The probability density of the (signed) difference $\Delta t = t_{\text{rec}} - t_{\text{tag}}$ between the proper decay times of the B mesons is given by

$$g(\Delta t; \tau) = \frac{1}{N} \cdot \frac{dN}{d(\Delta t)} = \frac{\Gamma}{2} e^{-\Gamma|\Delta t|}. \quad (1)$$

The challenge of the measurement is to disentangle the resolution in Δz , 190 μm rms, from the effects of the B lifetime, since both contribute to the width of the Δt distribution as pictured in the lower panels of Figure 5. In the absence of background, the

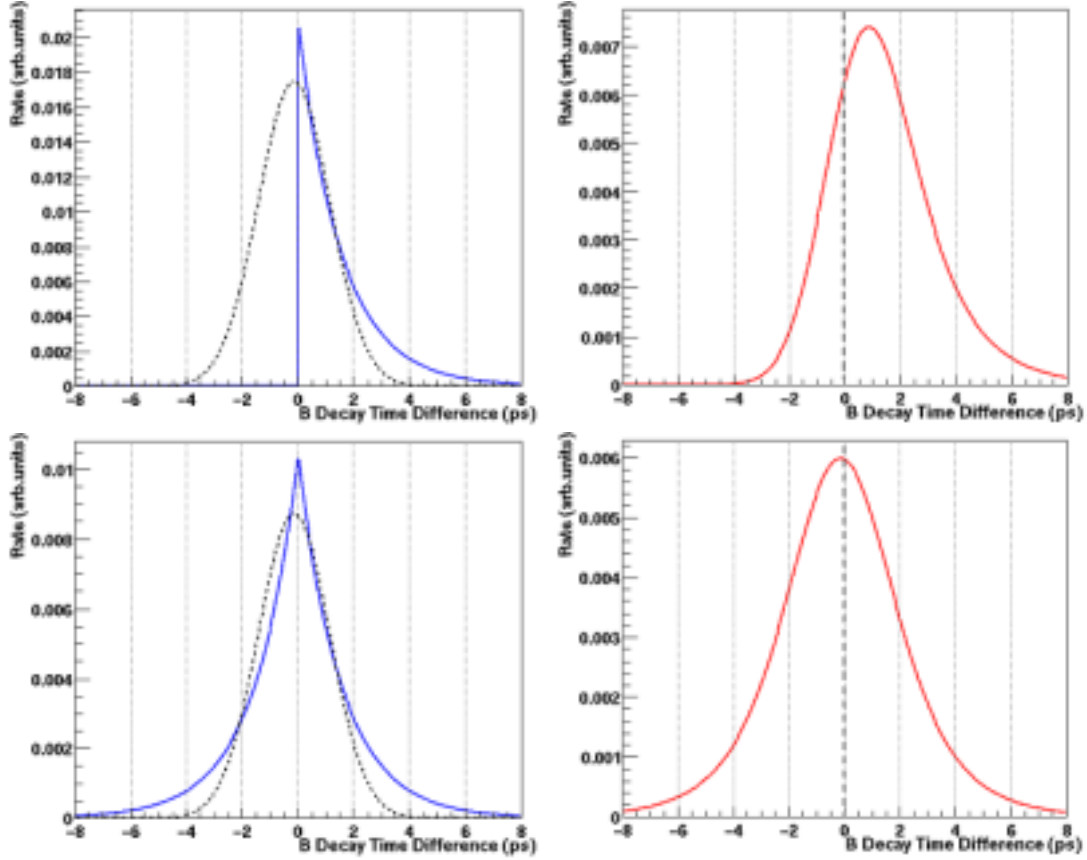


Fig. 5. Illustration of lifetime measurements at LEP/CDF (upper plots) and at the B Factories (lower plots). For the former, the underlying physics distribution is a one-sided exponential (left) convolved with a Gaussian time resolution function (right). For the latter, the underlying physics distribution is a two-sided exponential (left) convolved with a Gaussian time difference resolution function (right).

measured Δt distribution is described by the probability density function (PDF)

$$\mathcal{G}(\Delta t; \tau, \hat{a}) = g(\Delta t_{\text{true}}; \tau) \otimes \mathcal{R}(\delta_t; \hat{a}), \quad (2)$$

where $\mathcal{R}(\delta_t = \Delta t - \Delta t_{\text{true}}; \hat{a})$ is the time-difference resolution function with parameters \hat{a} . The advantage of a B Factory experiment is the very large data sample, with excellent control of the B meson sample through full reconstruction allowing a good understanding of the small backgrounds and measurement errors.

1.4 Measurement of B^0 flavor oscillations

The phenomenon of particle–anti-particle mixing in the neutral B meson system was first observed almost fifteen years ago.^{19,11} The oscillation frequency in B^0 - \bar{B}^0 mixing has been extensively studied with both time-integrated and time-dependent techniques.¹⁸ By interchanging $b\bar{d}$ with $\bar{b}d$, B^0 - \bar{B}^0 mixing changes the additive bottom quantum number by two units, *i.e.*, $|\Delta B| = 2$. In the Standard Model, such a process is the result of ordinary $|\Delta B| = 1$ weak interactions in second order involving the exchange of virtual charge-2/3 quarks, with the top quark contributing the dominant amplitude. A measurement of Δm_d is therefore sensitive to the value of the CKM matrix element V_{td} . At present the sensitivity to V_{td} is not limited by experimental precision on Δm_d , but by theoretical uncertainties in the calculation, in particular the quantity $f_B^2 B_B$, where f_B is the B^0 decay constant, and B_B is the so-called bag factor, representing the $\Delta B = 2$ strong-interaction matrix element. There may also be contributions from interactions outside the Standard Model

Beyond these questions of fundamental interest, since the measurement of Δm_d incorporates all elements of the analysis for time-dependent CP asymmetries, including B reconstruction, tagging, and Δt determination and resolution, it is an essential test of our understanding of these aspects of the $\sin 2\beta$ measurement.

For the measurement of Δm_d , one neutral B (B_{flav}) is fully reconstructed in a flavor eigenstate²⁰ as $D^{(*)-}\pi^+/\rho^+/a_1^+$ or $J/\psi K^{*0}$ ($K^{*0} \rightarrow K^+\pi^-$), while the second is tagged by its decay products. For the neutral B system produced on the $\Upsilon(4S)$, the probability for obtaining a *mixed*, $B^0 B^0$ or $\bar{B}^0 \bar{B}^0$, or *unmixed*, $B^0 \bar{B}^0$, final state is a function of Δm_d and the proper time difference Δt between the two B decays:

$$\text{Prob}(B^0 \bar{B}^0 \rightarrow B^0 B^0 \text{ or } \bar{B}^0 \bar{B}^0) = \frac{\Gamma}{4} e^{-\Gamma|\Delta t|} (1 - \cos \Delta m_d \Delta t) \quad (3)$$

$$\text{Prob}(B^0 \bar{B}^0 \rightarrow B^0 \bar{B}^0) = \frac{\Gamma}{4} e^{-\Gamma|\Delta t|} (1 + \cos \Delta m_d \Delta t), \quad (4)$$

where $\tau_{B^0} = 1/\Gamma$ is the B^0 lifetime. The final state can be classified as mixed or unmixed depending on whether the reconstructed flavor-eigenstate $B_{\text{rec}} = B_{\text{flav}}$ has the same or the opposite flavor as the tagging $B = B_{\text{tag}}$. These underlying physics distributions for the time development of mixed and unmixed events can be seen in Figure 6a. In this ideal situation there are no mixed events at $\Delta t = 0$, which then develop only of a time scale governed by the mixing frequency Δm_d . If the Δt resolution and flavor

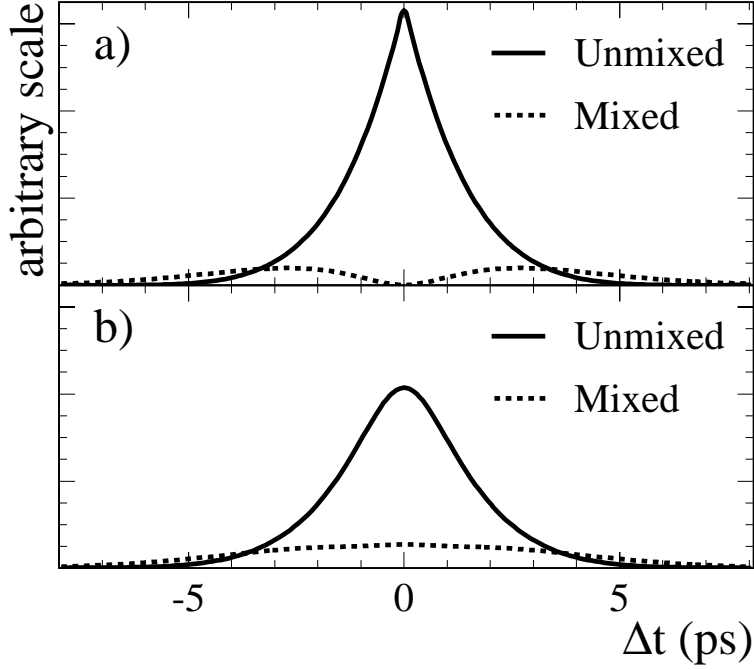


Fig. 6. Expected Δt distribution for mixed and unmixed events a) with perfect tagging and Δt resolution, and b) with typical mistag rates and Δt resolution.

tagging were perfect, the asymmetry as a function of Δt

$$A_{\text{mixing}}(\Delta t) = \frac{N_{\text{unmix}}(\Delta t) - N_{\text{mix}}(\Delta t)}{N_{\text{unmix}}(\Delta t) + N_{\text{mix}}(\Delta t)} \quad (5)$$

would describe a cosine function with unit amplitude. The asymmetry goes through zero near $2.1 B^0$ proper lifetimes and the sensitivity to Δm_d , which is proportional to $\Delta t^2 e^{-\Gamma|\Delta t|} \sin^2 \Delta m_d \Delta t$, reaches a maximum in this region. If the tagging algorithm incorrectly identifies the tag with a probability w , the amplitude of the oscillation is reduced by a dilution factor $\mathcal{D} = (1 - 2w)$. When more than one type of flavor tag is used, each has its own mistag rate w_i .

Neglecting any background contributions, the probability density functions (PDFs) for the mixed ($-$) and unmixed ($+$) events, \mathcal{H}_{\pm} , can be expressed as the convolution of the underlying oscillatory physics distribution

$$h_{\pm}(\Delta t; \Gamma, \Delta m_d, w) = \frac{\Gamma}{4} e^{-\Gamma|\Delta t|} [1 \pm \mathcal{D} \cos \Delta m_d \Delta t] \quad (6)$$

with a time-difference resolution function $\mathcal{R}(\delta_t = \Delta t - \Delta t_{\text{true}}; \hat{a})$ to give

$$\mathcal{H}_{\pm}(\Delta t; \Gamma, \Delta m_d, w, \hat{a}) = h_{\pm}(\Delta t_{\text{true}}; \Gamma, \Delta m_d, w) \otimes \mathcal{R}(\delta_t; \hat{a}), \quad (7)$$

where Δt and Δt_{true} are the measured and the true time differences, and \hat{a} are parameters of the resolution function. Figure 6b illustrates the impact of typical mistag and Δt resolution effects on the Δt distributions for mixed and unmixed events.

A fit to the proper time distribution of mixed and unmixed neutral flavor-eigenstate events can be used to extract the mistag fractions w_i and resolution parameters \hat{a}_i and, simultaneously, the mixing rate Δm_d . The fitted mistag fractions and resolution parameters can then be used for extracting $\sin 2\beta$ with the CP -sample. The correlation between the extracted values for w_i and Δm_d is small, because the rate of mixed events near $\Delta t = 0$, where the B^0 - \bar{B}^0 mixing probability is small, is principally governed by the mistag rate. Conversely, the sensitivity to Δm_d increases at larger values of Δt ; when Δt is approximately twice the B lifetime, half of the neutral B mesons will have oscillated.

1.5 Measurement of CP asymmetries

For the measurement of CP asymmetries, one B (B_{CP}) is fully reconstructed in a CP eigenstate with eigenvalue $\eta_{CP} = -1$ ($J/\psi K_s^0$, $\psi(2S)K_s^0$, $\eta_c K_s^0$ or $\chi_{c1} K_s^0$) or $+1$ ($J/\psi K_L^0$), while the second is tagged with its decay products just as for the mixing measurement. The B_{CP} sample can be further enlarged by including the mode $J/\psi K^{*0}$ ($K^{*0} \rightarrow K_s^0 \pi^0$). However, due to the presence of even ($L = 0, 2$) and odd ($L = 1$) orbital angular momenta in the $J/\psi K^{*0}$ system, there are $\eta_{CP} = +1$ and -1 contributions to its decay rate, respectively. When the angular information in the decay is ignored, the measured CP asymmetry in $J/\psi K^{*0}$ is reduced by a dilution factor $D_{\perp} = 1 - 2R_{\perp}$, where R_{\perp} is the fraction of the $L = 1$ component. This fraction has been measured at *BABAR*²¹ and *Belle*,²² and leads to an effective $\eta_{CP} \sim 65\%$ for the $J/\psi K^{*0}$ mode.

The expected time evolution for the tagged B_{CP} sample depends both on B^0 - \bar{B}^0 mixing and on the decay amplitudes of B^0 and \bar{B}^0 to the final state f through a single complex parameter λ . Mixing generates a lifetime difference as well as a mass difference between the two neutral B meson mass eigenstates, but the lifetime difference is expected to be small since it is a consequence of common final states in B^0 and \bar{B}^0 decays. Such common states, which include the CP eigenstates studies here, make up a very small fraction of the decay width. Dropping these, and thus ignoring any lifetime difference, results in a simple expression for λ in terms of the $|\Delta B = 1|$ and $|\Delta B = 2|$ interactions,

$$\lambda = -\frac{\langle B^0 | \mathcal{H}_{\Delta B=2} | \bar{B}^0 \rangle \langle f | \mathcal{H}_{\Delta B=1} | \bar{B}^0 \rangle}{\langle B^0 | \mathcal{H}_{\Delta B=2} | B^0 \rangle \langle f | \mathcal{H}_{\Delta B=1} | B^0 \rangle}. \quad (8)$$

Redefining the states for B^0 and \bar{B}^0 by multiplying them by two different phases has no effect on λ , which is thus phase-convention independent, as every physical observable must be. The decay distributions are

$$f_{\pm}(\Delta t) = \frac{\Gamma}{4} e^{-\Gamma|\Delta t|} \left\{ 1 \pm \mathcal{D} \left[\frac{2\text{Im}\lambda}{1+|\lambda|^2} \sin \Delta m_d \Delta t - \frac{1-|\lambda|^2}{1+|\lambda|^2} \cos \Delta m_d \Delta t \right] \right\}, \quad (9)$$

where the $+$ or $-$ sign indicates whether the B_{tag} is tagged as a B^0 or a \bar{B}^0 , respectively. The dilution factor $\mathcal{D} = 1 - 2w$ accounts for the probability w that the flavor of the tagging B is identified incorrectly.

The distributions are much simpler when $|\lambda| = 1$, which is the expectation of the Standard Model for decays like $B^0 \rightarrow J/\psi K_s^0$. If all the mechanisms that contribute to the decay have the same weak phase then the ratio of the weak decay amplitudes in Eq. 8 is just $\eta_{CP} e^{2i\phi_{\text{dec}}}$, where ϕ_{dec} is the weak phase for $\bar{B}^0 \rightarrow f$; ϕ_{dec} is convention dependent and unobservable. The remaining factor introduces a phase due to B^0 - \bar{B}^0 mixing. The combination of these phases is convention independent and observable.

For decays such as $B^0 \rightarrow J/\psi K_s^0$, or more generally $(c\bar{c})K_s^0$ and $(c\bar{c})K_L^0$, an explicit representation for λ can be found from the ratio of the amplitude for $\bar{B}^0 \rightarrow (c\bar{c})\bar{K}^0$ to the interfering process $\bar{B}^0 \rightarrow B^0 \rightarrow (c\bar{c})K^0 \rightarrow (c\bar{c})\bar{K}^0$. The decay $B^0 \rightarrow (c\bar{c})K^0$ involves a $\bar{b} \rightarrow \bar{c}\bar{c}\bar{s}$ transition with an amplitude proportional to $[V_{cb}^*V_{cs}]$, while $\bar{B}^0 \rightarrow (c\bar{c})\bar{K}^0$ provides analogously a factor $\eta_{CP}[V_{cb}V_{cs}^*]$. Because $\bar{B}^0 \rightarrow B^0$ mixing is dominated by the loop diagram with a t quark, it introduces a factor $[V_{td}^*V_{tb}/V_{td}V_{tb}^*]$, while $K^0 \rightarrow \bar{K}^0$ mixing, being dominated by the c -quark loop, adds a factor $[V_{cd}V_{cs}^*/V_{cd}^*V_{cs}]$. Altogether, for transitions of the type $b \rightarrow c\bar{c}s$,

$$\begin{aligned} \lambda &= \eta_{CP} \left(\frac{V_{td}V_{tb}^*}{V_{td}^*V_{tb}} \right) \left(\frac{V_{cb}V_{cs}^*}{V_{cb}^*V_{cs}} \right) \left(\frac{V_{cd}^*V_{cs}}{V_{cd}V_{cs}^*} \right) \\ &= \eta_{CP} \left(\frac{V_{cb}V_{cd}^*}{V_{tb}V_{td}^*} \right) \left(\frac{V_{tb}^*V_{td}}{V_{cb}^*V_{cd}} \right) \\ &= \eta_{CP} e^{-2i\beta}. \end{aligned} \quad (10)$$

The time-dependent rate for decay of the B_{CP} final state is then given by

$$f_{\pm}(\Delta t; \Gamma, \Delta m_d, w, \sin 2\beta) = \frac{\Gamma}{4} e^{-\Gamma|\Delta t|} [1 \mp \eta_{CP} \mathcal{D} \sin 2\beta \sin \Delta m_d \Delta t]. \quad (11)$$

These underlying physics distributions can be seen in Figure 7a, where constructive (destructive) sinusoidal interference effects can be seen at positive Δt for B^0 (\bar{B}^0)-tagged CP eigenstate decays and vice versa at negative Δt . In the limit of perfect

determination of the flavor of the fully-reconstructed B in the B_{flav} sample, which we assume throughout, the dilution here and in the mixed and unmixed amplitudes of Eq. 6 arise solely from the B_{tag} side, allowing the values of the mistag fractions w_i to be determined by studying the time-dependent rate of B^0 - \bar{B}^0 oscillations.

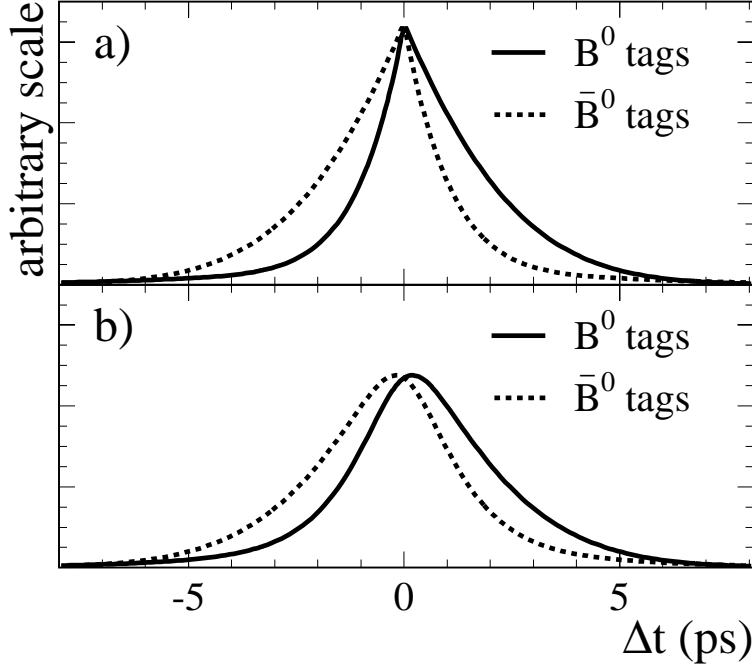


Fig. 7. Expected Δt distribution for B^0 - and \bar{B}^0 -tagged CP events with $\sin 2\beta = 0.7$ and either a) perfect tagging and Δt resolution, or b) typical mistag rates and Δt resolution.

To account for the finite resolution of the detector, the time-dependent distributions f_{\pm} for B^0 and \bar{B}^0 tagged events (Eq. 11) must be convolved with a time resolution function $\mathcal{R}(\delta_t = \Delta t - \Delta t_{\text{true}}; \hat{a})$ as described above for mixing,

$$\mathcal{F}_{\pm}(\Delta t; \Gamma, \Delta m_d, w, \sin 2\beta, \hat{a}) = f_{\pm}(\Delta t_{\text{true}}; \Gamma, \Delta m_d, w, \sin 2\beta) \otimes \mathcal{R}(\delta_t; \hat{a}), \quad (12)$$

where \hat{a} represents the set of parameters that describe the resolution function. In practice, events are separated into the same tagging categories as in mixing, each of which has a different mistag fraction w_i , determined individually for each category. Figure 7 illustrates the impact of typical mistag and Δt resolution effects on the Δt distributions for B^0 - and \bar{B}^0 -tagged CP events.

It is possible to construct a CP -violating observable

$$\mathcal{A}_{CP}(\Delta t) = \frac{\mathcal{F}_+(\Delta t) - \mathcal{F}_-(\Delta t)}{\mathcal{F}_+(\Delta t) + \mathcal{F}_-(\Delta t)}, \quad (13)$$

which, neglecting resolution effects, is proportional to $\sin 2\beta$:

$$\mathcal{A}_{CP}(\Delta t) \propto -\eta_{CP} \mathcal{D} \sin 2\beta \sin \Delta m_d \Delta t. \quad (14)$$

Since no time-integrated CP asymmetry effect is expected, an analysis of the time-dependent asymmetry is necessary. The interference between the two amplitudes, and hence the CP asymmetry, is maximal after approximately $2.1 B^0$ proper lifetimes, when the mixing asymmetry goes through zero. However, the maximum sensitivity to $\sin 2\beta$, which is proportional to $e^{-\Gamma|\Delta t|} \sin^2 \Delta m_d \Delta t$, occurs in the region of 1.4 lifetimes.

1.6 Overview of these lectures

It is clear that the three measurements discussed above are interrelated through their common use of fully reconstructed B meson samples and time-dependent distributions. The lifetime measurements are the most precise, but only involve vertex separation and not tagging. Mixing incorporates the need for tagging and allows an exploration of the time development of asymmetries with B mesons samples that are 10 times larger than available for the CP violation study. Searches for time-dependent CP violation in the CP sample build on the solid foundation formed by these measurements.

These lectures provide an overview of recent studies of the time development of B mesons produced in asymmetric energy e^+e^- collisions at the $\Upsilon(4S)$: lifetimes of charged and neutral B mesons,^{23,24} $B^0-\bar{B}^0$ flavor oscillations^{25,26} and CP -violating asymmetry^{27,28} in the neutral B meson system. There is already a vast literature on this subject, making it nearly impossible to do justice to the body of work that is underway in this area. The reader should consult the bibliography for original sources and further details. It has also not been possible to address the full array of experimental activity, such as partial reconstruction approaches to time-dependent asymmetry measurements, so the interested reader should be aware that the techniques reported here are just part of the repertoire. Finally, both *BABAR* and Belle have been very active in exploring time-dependent asymmetries in B decays. Since the techniques and illustrations from the former are more accessible and familiar to me, I will draw examples to a large extent from *BABAR*, while pointing out the beautiful measurements also available from Belle.

This is merely a practical expedient, but the reader should keep in mind the equally creative and thorough work that underlies the Belle measurements.

With these significant limitations in mind, the discussion will be developed as follows:

- Section 2: The B factory colliders.** Brief review of B factories and recent operational experience;
- Section 3: The B factory detectors.** Basic design criteria and implementation at *BABAR* and Belle;
- Section 4: Reconstructing B mesons.** Techniques for reconstruction of B mesons on the $\Upsilon(4S)$ both in flavor eigenstate and CP modes;
- Section 5: Determining proper time differences.** Measurement of the distance Δz between the two B^0 decay vertices along the $\Upsilon(4S)$ boost axis, and its conversion to Δt ;
- Section 6: Measuring B lifetimes.** Measurement of B lifetimes from the proper decay time distribution of B mesons in the B_{flav} sample;
- Section 7: Determining B flavor.** Techniques for determining the flavor of the second B_{tag} meson in $\Upsilon(4S)$ events;
- Section 8: Fitting techniques.** Construction of a log-likelihood function to describe the time evolution of signal and background events in the presence of mixing and CP asymmetry;
- Section 9: Measurement of B^0 mixing.** Measurement of the mixing rate Δm_d , mistag fractions w_i , and vertex resolution parameters \hat{a}_i for the different tagging categories i , with an unbinned maximum-likelihood fit to the B_{flav} sample;
- Section 9: Observation of CP violation.** Extraction of a value of $\sin 2\beta$, or more generally $Im\lambda/|\lambda|$ and $|\lambda|$, from the amplitude of the CP asymmetry, the mistag fractions w_i , and the vertex resolution parameters \hat{a}_i for the different tagging categories i , with fits to the B_{flav} and B_{CP} samples.
- Section 13: Prospects and summary.** Brief discussion of plans for improved luminosity and enlarged data samples. Summary of projections for precision measurements of CP violation asymmetries.

2 The B factory colliders

The B Factory projects at SLAC²⁹ and KEK³⁰ are high-luminosity e^+e^- colliding beam storage ring facilities designed to operate at a center-of-mass energy of 10.58 GeV, equivalent to the mass of the $\Upsilon(4S)$ resonance, with asymmetric energy beams. The need for asymmetric energy beams, which allow a determination of the proper time difference between the decays of the two B mesons produced at the $\Upsilon(4S)$, has already been discussed. The requirement of peak luminosity in excess of $3 \times 10^{33} \text{ cm}^{-2}\text{s}^{-1}$ has also been motivated. The luminosity of a colliding beam machine is given by

$$\mathcal{L} = \frac{N_+ N_- f}{A} \quad (15)$$

where N_+ and N_- are the number of particles per bunch, f is the collision frequency, and A is the effective collision area. Therefore, the high luminosity required by the B Factories demands a combination of a large number of particles per bunch, high collision frequency, and small collision area. In each of these parameters there are practical or physical limits to how far the design can be pushed. For example, there are limits imposed on the number of particles per bunch by the broadband impedance of the vacuum system. In addition, the total current $I_{\pm} = N_{\pm} f$ in the storage ring is generally limited by the narrowband impedance principally of the RF cavities, synchrotron and electromagnetic heating of vacuum system elements, gas desorption due to synchrotron radiation, and ion trapping.

The electromagnetic focusing of one beam by the passage of the other beam, quantified in terms of the beam-beam tune shift, imposes a constraint on efforts to reduce the beam area at the IP. The non-linear nature of beam-beam forces at large N leads to empirical limits on the maximum tune shift with stable beams. The tune shift does not limit the vertical focusing of the beam β_y^* , which is instead restricted by increases in chromaticity and hence reduction in the aperture for stable beams. Likewise, beam-beam effects become stronger when β_y^* approaches the bunch length, which can only be reduced in turn by significant increases in RF voltage.

The frequency f is set by the spacing of the bunches in the machine. Parasitic collisions outside the interaction point would of course contribute additional tune shift. Therefore, the maximum frequency is set by the ability to separate the beams. In this case, the separation of the beams is actually facilitated by their asymmetric energies. Separation schemes with a finite crossing angle have been implemented at KEKB, while PEP-II uses magnetic separation with head-on collisions.

Under conditions of energy-transparency, whereby the beam-beam behavior of the asymmetric energy beams is made as similar to a symmetric collider as possible, the additional constraint

$$\left(\frac{EI}{\beta_y^*}\right)^+ = \left(\frac{EI}{\beta_y^*}\right)^- \quad (16)$$

applies. In this case the luminosity can be written

$$\mathcal{L} = (2.17 \times 10^{34} \text{ cm}^{-1} \text{ s}^{-1}) \xi_y \left(\frac{EI}{\beta_y^*}\right)^\pm \quad (17)$$

where E is in GeV, I in Amperes, and β_y^* is in cm. Thus, adopting typical B Factory design values for the collider, e.g., maximum tune shift (0.03-0.06), vertical focusing at the IP ($\beta_y^* \sim 1$ cm), and beam currents ($I_{\text{HER}} \sim 0.75$ A), leads to luminosities in the desired range of $4\text{--}8 \times 10^{33} \text{ cm}^{-1} \text{ s}^{-1}$. It should be noted that at in current operation both PEP-II and KEKB violate the energy transparency condition, mainly due to blow-up of the LER beam size due to electron cloud effects. This has led to an need to store more HER current to compensate for the degraded performance.

With these considerations, the B Factory colliders are led to designs involving the circulation of large numbers of conventional bunches that reach 1–2 A circulating currents, each bunch being brought into collision at a single interaction point to minimize beam-beam interactions, and final focus quadrupoles imbedded close to the IP to achieve $\beta_y^* \sim 1$ cm with sufficient rf power to have correspondingly short bunch lengths.

2.1 PEP-II at SLAC

One of two facilities built on these principles is the PEP-II project, an e^+e^- colliding beam storage ring complex designed to produce a luminosity of at least $3 \times 10^{33} \text{ cm}^{-2} \text{ s}^{-1}$, with asymmetric energy beams of 3.1 for the positrons and 9.0 GeV for the electrons. The facility was approved for construction in the fall of 1993 and achieved first collisions for physics in late May 1999.

Figure 8 shows a schematic view of the accelerator complex at SLAC, including the 2200 m PEP tunnel. The SLAC linac serves as a powerful injector for the PEP-II storage rings. This allows short fill and top-off times, resulting in a average to peak luminosity ratio of about 75% at PEP-II versus 62% at KEKB. Electron and positron bunches at the circulation energies of 9.0 and 3.1 GeV respectively are extracted at appropriate points along the linac, transported the remaining length of the linac tunnel



Fig. 8. Artist's view of the accelerator complex involved with the SLAC *B* Factory. The SLAC Linac is used to accelerate electrons and positrons to injection energy, where the beams are extracted and injected into a double storage ring contained in the PEP tunnel.

and then injected into the PEP-II rings via two separate transfer lines. Both the High Energy Ring (HER) and the Low Energy Ring (LER) are housed in the original PEP tunnel. Each ring consists of 6 arc sections and 6 long straight sections, with the HER mounted close to the floor and the LER above. The HER uses refurbished PEP dipole, quadrupole and sextapole magnets for the 192 half-cells that form the arc sections, while the LER incorporates new short-dipole, quadrupole and sextapole magnets.

A copper vacuum chamber is employed for the HER, with relatively low gas photo-desorption allows the arc vacuum to reach 10 nTorr, despite the the large synchrotron light load from the high currents. For the LER, the synchrotron light created in the short bending magnets is absorbed outside the magnets in a copper lined anti-chamber.

The rf system for PEP II is based on a warm copper cavity design with higher-order mode (HOM) damping provided by three waveguides that terminate in rf absorbers at the ends. The original design called for 20 cavities powered by 5 klystrons for the HER

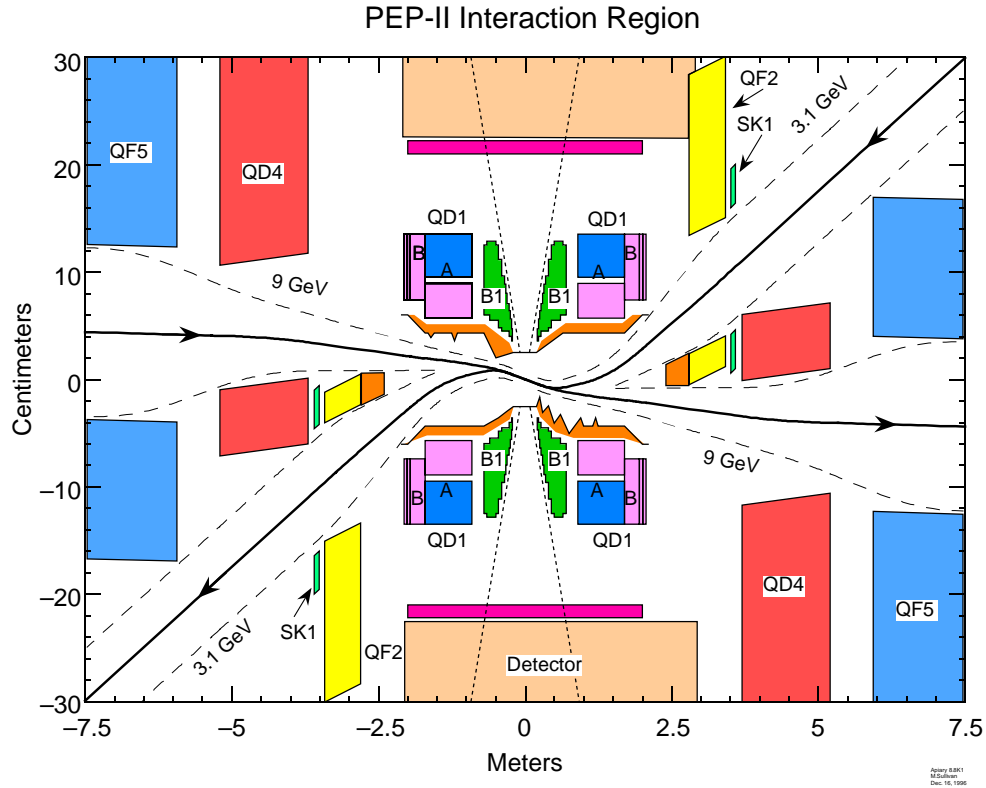


Fig. 9. Schematic layout of the PEP-II interaction region, showing the S-bend scheme that brings the low and high energy beams into head-on collision and then separates them again with a dipole magnet close to the IP. Note that the distorted transverse and longitudinal distance scales in this schematic of the layout.

and an additional 10 cavities for the LER. Additional rf stations are scheduled to come online in the coming years, since rf power is the main limitation for HER current and therefore peak luminosity. The additional rf will allow reduction of the bunch length and the reduction of β_y^* to as small as 8 mm.

As already noted, the two rings need to be brought into collision at the interaction point and then separated again, without introducing additional parasitic crossings. This is accomplished with a head-on collision scheme at PEP-II, where the initial separation kick is achieved with a samarium-cobalt dipole magnet about 20 cm away from the IP. Additional separation is provided by off-axis quadrupole field. The layout of the interaction region is shown schematically in Figure 9. Note that this is an accelerator view of the experiment, with very different horizontal and vertical axis scales. The beams are brought into collision and then exit the IP along an S-bend orbital path. This facil-

Table 3. Original PEP-II design parameters and achieved performance to date.

	Design		Achieved	
	e^-	e^+	e^-	e^+
Beam energies [GeV]	9	3.1		
Currents [A]	0.75	2.14	1.05	2.14
Number of bunches	1658		830	
$L [\times 10^{33} \text{ cm}^{-2} \text{ s}^{-1}]$	3.0		4.6	
Bunch spacing [m]	1.26		2.52	
β_x^*, β_y^* [cm]	50/1.5	50/1.5	50/1.25	50/0.9
ξ_x, ξ_y	0.03	0.03	0.070/0.029	0.062/0.056
Bunch currents [mA]	0.45	1.29	1.28	2.20
Beam stored energy [kJ]	49	49	69	41
Beam power [GW]	6.7	6.7	9.4	5.6
Beam rf power [MW]	1.8	1.7	2.5	1.4

itates the design of shielding for the synchrotron light generated in the magnetic field bends. In particular, the light generated by the HER ring as it is brought into collision passes through the IP and is dumped over 5 m away on the far side of the interaction region. By this means and careful masking schemes, the potential backgrounds from synchrotron light are minimized, so that beam particle interactions, mostly near the interaction region, are the main source of backgrounds in the detector.

Some of the main design parameters of the PEP II machine are shown in Table 3, along with the performance records achieved to date.

2.2 KEKB at KEK

The other facility built on these principles is the KEKB project, an e^+e^- colliding beam storage ring complex designed to produce a luminosity of at least $10 \times 10^{33} \text{ cm}^{-2} \text{ s}^{-1}$, with asymmetric energy beams of 3.5 for the positrons and 8.0 GeV for the electrons. Just like PEP-II, the facility was approved for construction in the fall of 1993 and achieved first collisions for physics in late May 1999.

Figure 10 shows a schematic view of the accelerator complex at KEK, including the 3016 m Tristan tunnel. The specialized 8 GeV linac was constructed as an injector.

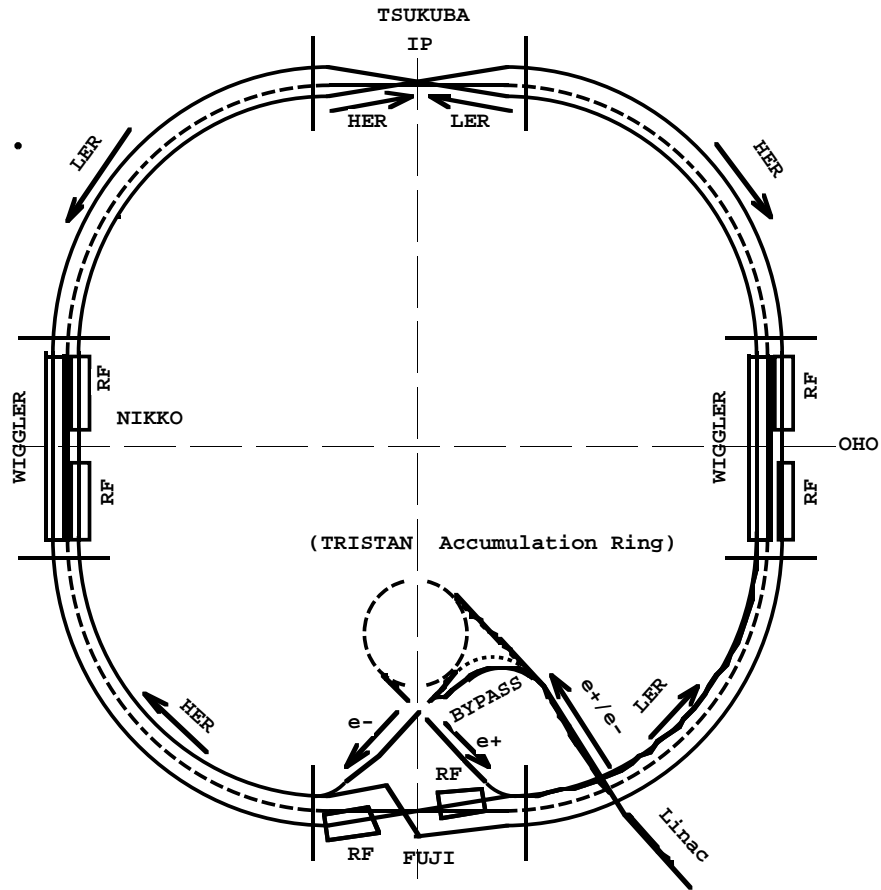


Fig. 10. Artists view of the accelerator complex involved with the KEK *B* Factory. A dedicated linac is used to accelerate electrons and positrons to injection energy, where the beams are extracted and injected into a double storage ring contained in the Tristan tunnel.

Electron and positron bunches at the circulation energies of 8.0 and 3.5 GeV respectively are injected into the KEKB rings via two separate transfer lines. Both the High Energy Ring (HER) and the Low Energy Ring (LER) are housed in the original Tristan tunnel, which is wide enough to house the beams side-by-side. For half the ring the HER occupies the inside position and for the other half it trades places with the LER. This insures that the orbit lengths are identical. Each ring consists of 4 arc sections and 4 long straight sections. A copper vacuum chamber is employed for both the HER and LER, since it is self-shielding and has a relatively low gas photo-desorption rate

The rf system for KEKB is based on two systems: a normal conducting 3-cavity design (ARES) with a large energy-storage cell and a single cell superconducting cavity

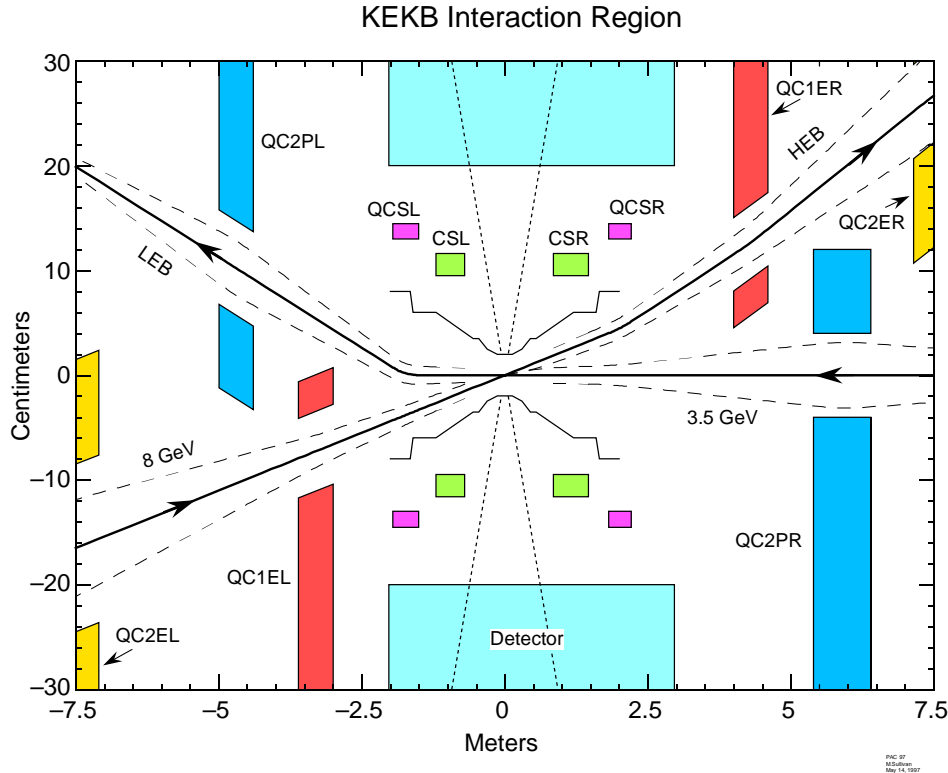


Fig. 11. Schematic layout of the KEKB interaction region, showing the angled crossing scheme that brings the low and high energy beams into collision and then allows separation without a dipole magnet near the IP.

(SCC) attached to large aperture beam pipe with ferrite rf absorbers to remove HOM. The original design called for 20 ARES cavities powered by 10 klystrons for the LER and an additional 8 SCC (12 ARES) cavities for the HER with 8 (6) klystrons. Additional rf stations are scheduled to come online in the coming years, since again rf power is the main limitation for HER current and therefore peak luminosity.

The beams are brought into collision with an angled crossing of ± 11 mrad, so magnetic separation is not required near the IP. Originally there was some concern that the crossing angle would lead to additional beam-beam instability, but this has not proven to be the case in practice. The layout of the interaction region is shown schematically in Figure 11. The final focus for the LER is provided by a superconducting quadrupole magnet (QCS-R), with the solenoid compensation coil (S-R) mounted in the same cryostat. Again this is an accelerator view of the experiment, with very different horizontal and vertical axis scales. The beams are brought straight into collision and then exit

Table 4. Original KEKB design parameters and achieved performance to date.

	Design		Achieved	
	e^-	e^+	e^-	e^+
Beam energies [GeV]	8	3.5		
Currents [A]	1.1	2.6	0.92	1.37
Number of bunches	5000		1223	
$L [\times 10^{33} \text{ cm}^{-2} \text{ s}^{-1}]$	10.0		7.35	
Bunch spacing [m]	1.2		2.4	
β_x^*, β_y^* [cm]	33/1.0	33/1.0	59/0.62	61/0.7
ξ_x, ξ_y	0.039/0.052	0.039/0.052	0.074/0.041	0.080/0.048
Bunch currents [mA]	0.22	0.52	0.75	1.12
Beam stored energy [kJ]	90	92	73	49
Beam power [GW]	9	9	7	5
Beam rf power [MW]	4.0	4.5	2.5	1.4

with a bend on the far side of the IP. Without a dipole magnet near the IP, synchrotron radiation is only generated when the beams pass through quadrupole magnets off-axis. This makes synchrotron backgrounds inherently smaller, so that here too beam particle interactions, mostly near the interaction region, are the main source of backgrounds in the detector.

Some of the main design parameters of the KEKB machine are shown in Table 4, along with the performance records achieved to date.

2.3 Data Samples

The record of integrated luminosity delivered at PEP-II and KEKB are shown in Figures 12 and 13. The very successful start for the two colliders is clearly a remarkable accomplishment. PEP-II reached its design luminosity in the fall of 2000, barely one year after first collisions. Since the fall of 2001 it has routinely been delivering peak luminosity at 50% greater than design and daily integrated rates that are a factor of two over expectations. By March 2001, KEKB had achieved a peak luminosity that surpassed PEP-II and still holds the record luminosity by a significant margin at $7.25 \times 10^{33} \text{ cm}^{-1} \text{ s}^{-1}$. A summary of the current luminosity performance of both ma-

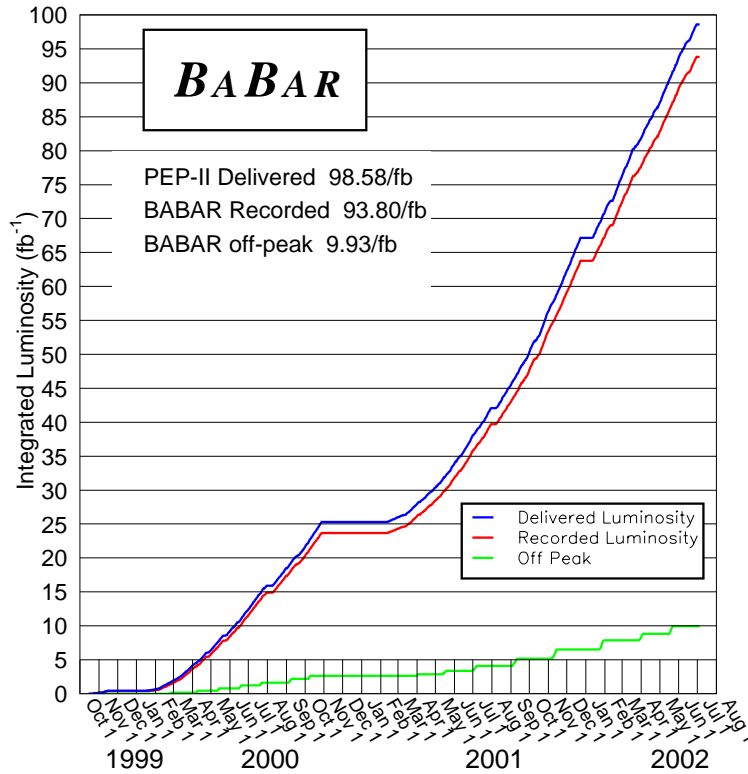


Fig. 12. History of integrated luminosity delivered by PEP-II and recorded by *BABAR*.

chines is provided in Table 5.

The data samples used for the *BABAR* measurements of *CP* asymmetries were recorded at the PEP-II collider in the period October 1999–June 2002. The total integrated luminosity of the data set is equivalent to 81.9 fb^{-1} collected near the $\Upsilon(4S)$ resonance. The corresponding number of produced $B\bar{B}$ pairs is estimated to be about 88 million. Belle measurements are based on a sample, recorded at KEKB through June 2002, that is equivalent to 78 fb^{-1} or 85 million $B\bar{B}$ pairs. In both cases, some of the other measurements discussed here, such as lifetime and mixing, were published prior to the summer of 2002 and consequently use a subsample of the full available dataset.

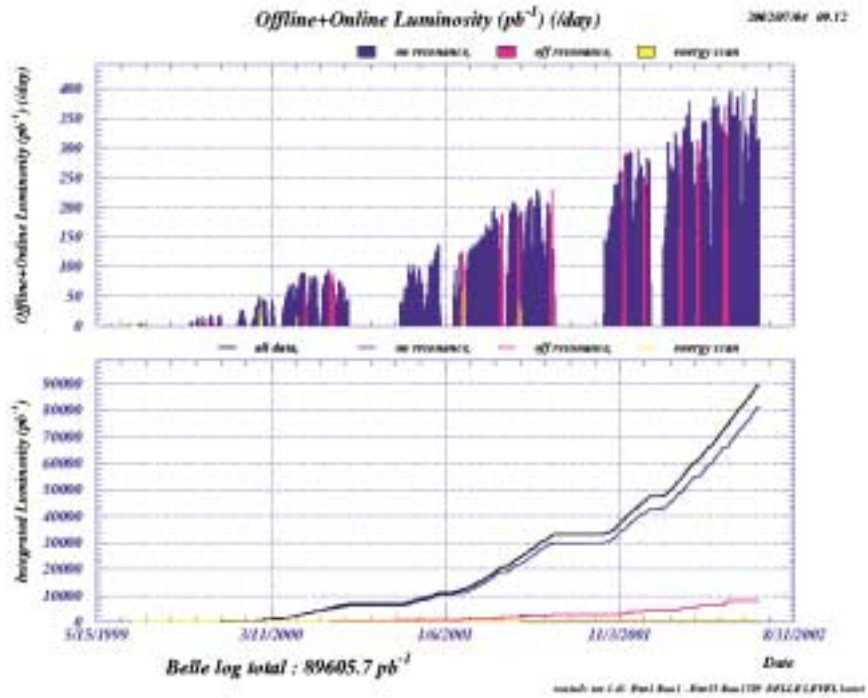


Fig. 13. History of integrated luminosity delivered by KEKB and recorded by Belle.

3 The B Factory Detectors

3.1 Design Requirements

In order to address the primary physics goal of measuring CP asymmetries in B decays the B Factory detectors need to be optimized^{31,32}:

- To reconstruct B mesons in a wide range of exclusive final states with high efficiency and low background;
- To tag the flavor of the other B meson in the event with high efficiency and purity; and
- To measure the proper time between the decays of the two B mesons.

The CP decay modes of interest generally have branching fractions below 10^{-4} . These channels involve observing anywhere from two to six charged particle daughters and often one or more π^0 mesons. Geometric acceptance, *i.e.*, the volume where full performance of the detector is achievable, to a large extent defines the efficiency for recon-

Table 5. B Factory luminosity performance to date.

	PEP-II Records	KEKB Records
Peak luminosity	$4.6 \times 10^{33} \text{ cm}^{-1}\text{s}^{-1}$	$7.25 \times 10^{33} \text{ cm}^{-1}\text{s}^{-1}$
Best shift	108.3 pb ⁻¹	129.5 pb ⁻¹
Best 24 hours	308.8 pb ⁻¹	377.2 pb ⁻¹
Best 7 days	1.865 fb ⁻¹	2.207 fb ⁻¹
Best month	6.66 fb ⁻¹	7.25 fb ⁻¹
Integrated logged	93.8 fb ⁻¹	89.6 fb ⁻¹

structuring such events. The boosted center-of-mass system at the asymmetric colliders makes it somewhat more difficult to maintain high single particle acceptance. Furthermore, the demands of high-luminosity lead to the placement of magnetic elements for beam focusing within the detector volume, significantly impacting forward and background acceptance.

3.1.1 Geometric acceptance requirements

Figure 14 illustrates the dependence of the reconstruction efficiency on detector acceptance limits in polar angular and momentum for several CP modes of interest. Although this is for the average boost at PEP-II, similar considerations hold at KEKB. The dependence on the forward polar angle can be seen to be particularly steep. The physical space occupied by magnetic elements generally precludes tracking below about 400 mrad or $\cos \theta_{min} < 0.92$. As a result, geometric efficiencies are reduced by 20% for two-body modes and substantially more for higher multiplicity final states. Given the rather soft momentum distribution for a typical B decay daughter, another important design criterion is the minimum detectable momentum (Figure 14c). This is important both for kaons used for tagging purposes and for channels that involve a $D^{*-} \rightarrow D^0 \pi^+$ transition, where the p_T spectrum all lies below 200 MeV/ c .

Many of the same considerations hold for the detection of neutral hadrons. However, since it is the two photons from the decay of π^0 mesons that are seen in the detector, the energy spectrum is largely dominated by photons below 400–500 MeV, as illustrated in Figure 15 for an ensemble of typical B decays. As a consequence, the efficiency for π^0 reconstruction, and ultimately B reconstruction, is a strong function

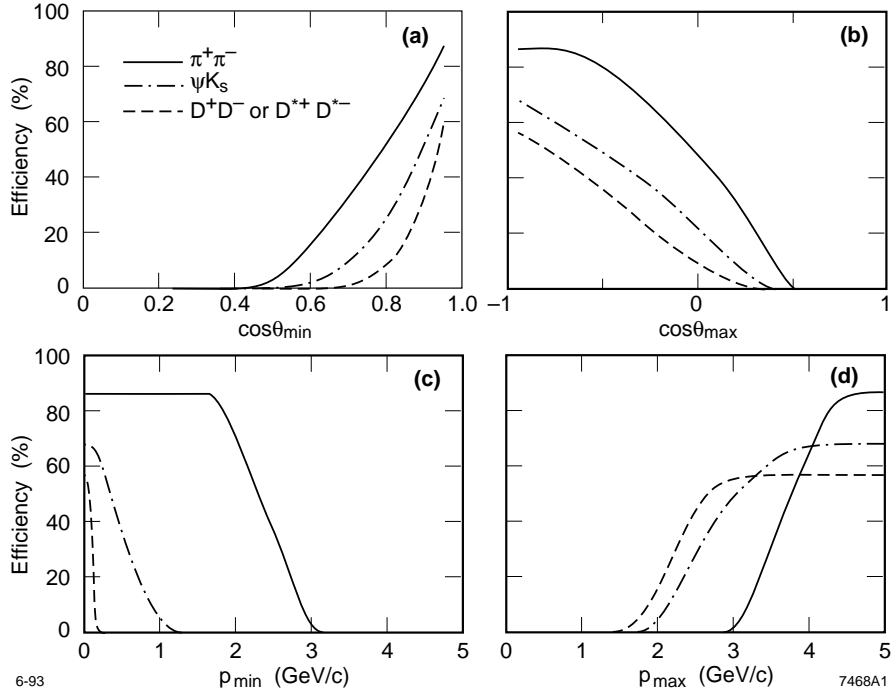


Fig. 14. Variation of geometric acceptance for boosted $\Upsilon(4S)$ system. Reconstruction efficiency for three representative B decay modes as a function of (a) minimum forward polar angle θ_{\min} , (b) maximum backward polar angle θ_{\max} , (c) minimum momentum, and (d) maximum momentum of the detector acceptance coverage. .

of the minimum detectable photon energy. With a 50 MeV threshold, on average 20% of the π^0 mesons from B decays are lost and the average B reconstruction efficiency is only 40%, as shown in Figure 16. At the other end of the energy spectrum there are specific channels, such as the two-body decay $B^0 \rightarrow \pi^0\pi^0$, that produce photons all the way up to 4 GeV. Thus, efficient B reconstruction requires very good energy and angular resolution over the range 20 MeV to 4 GeV.

3.1.2 Vertex detector requirements

A crucial element of the time-development measurements is the need to determine the proper time separation between the time-dilated flight distances of the B_{rec} and B_{tag} decays. Since the momentum spectrum of tracks from B decays are quite soft, tracking systems end up separating the function of measuring impact parameters (d_0, z_0) and angles (θ, ϕ) from the determination of transverse momentum p_T . This is a result of the impact of material and the significant contribution of multiple scattering to particle tra-

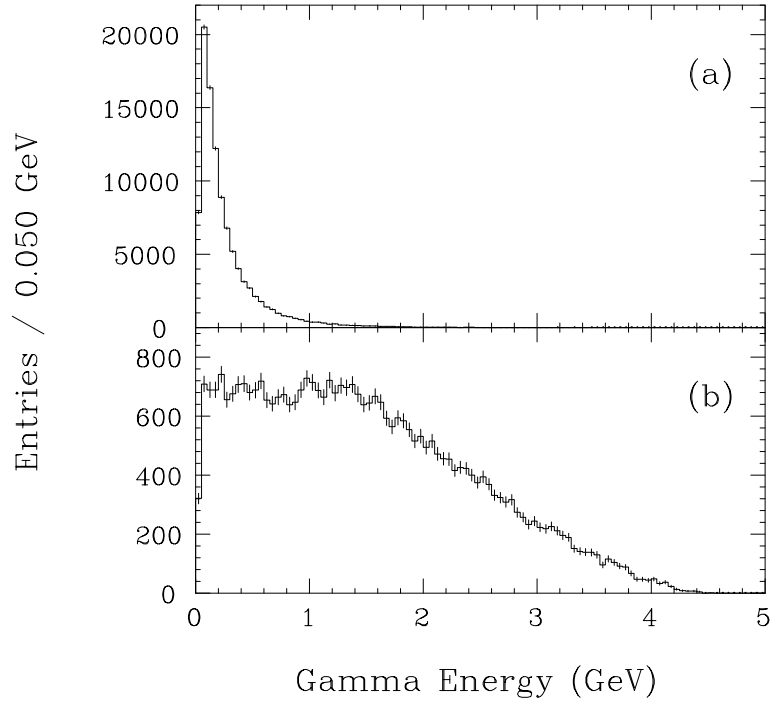


Fig. 15. Spectrum of π^0 momentum for generic B decays (upper) and the two-body channel $B^0 \rightarrow \pi^0 \pi^0$.

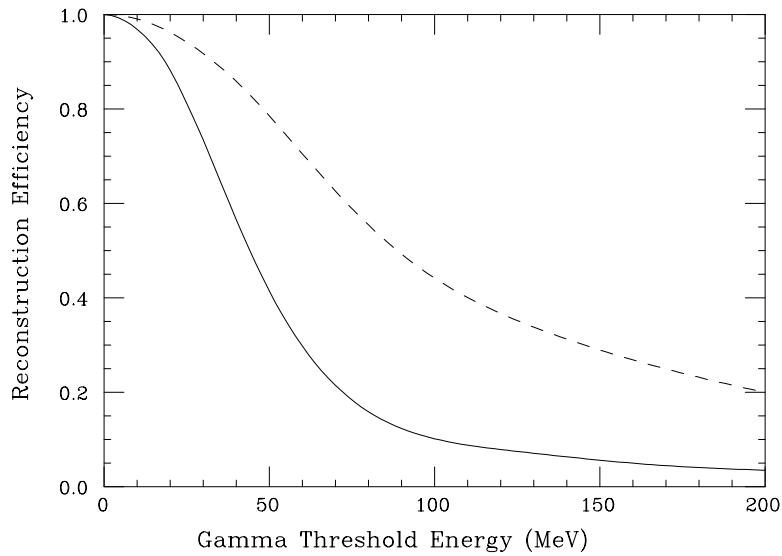


Fig. 16. Efficiency for π^0 (dashed curve) and B (solid curve) reconstruction as a function of the minimum detectable photon energy.

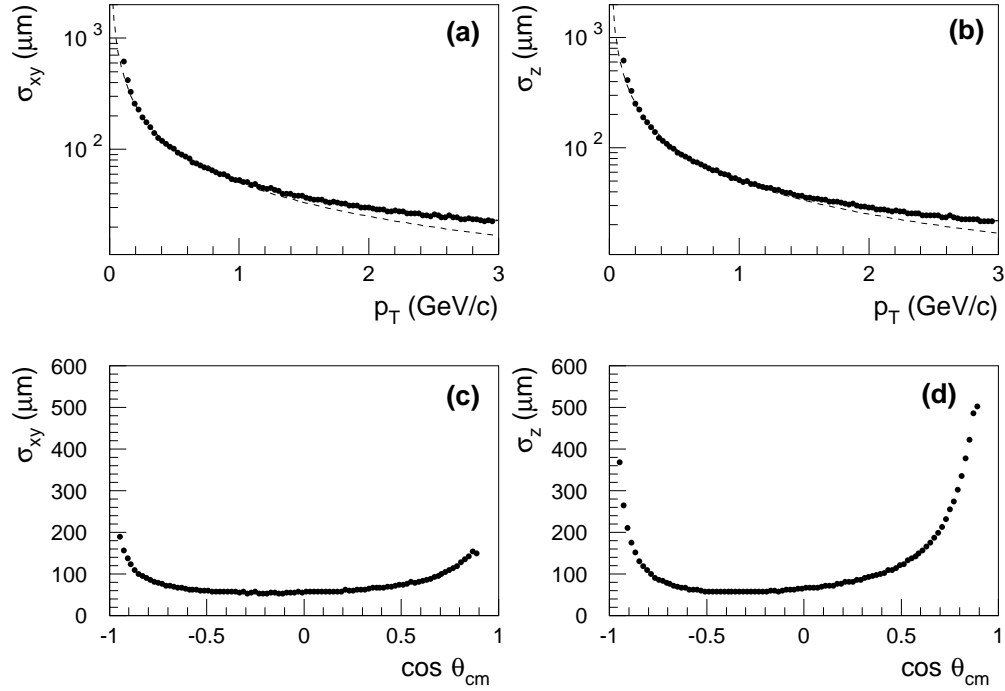


Fig. 17. Resolutions for impact parameters at the vertex: (a) σ_{xy} as a function p_T at $\cos \theta_{lab} = 0$; (b) σ_z as a function of p_T at $\cos \theta_{lab} = 0$; (c) σ_{xy} as a function of $\cos \theta_{lab}$ for $p_T = 1 \text{ GeV}/c$; and (d) σ_z as a function of $\cos \theta_{lab}$ for $p_T = 1 \text{ GeV}/c$. For (a) and (b), the dashed curve represents $50 \mu\text{m}/p_T$.

jectories. Thus, precision vertex detectors based on silicon microstrip detectors perform the function of measuring impact parameters and angles close to the IP, but at the cost of introducing considerable multiple scattering. Low mass drift chambers determine p_T from curvature over comparatively large radial track distances from the outermost vertex detector measurement to the outside of the tracking volume. In addition, the resolution for the B vertex separation along the HER beam direction introduces a new element into the measurement requirements, by placing an emphasis on the longitudinal position measurements and z_0 impact parameter resolution.

Impact parameter resolution is determined by resolution $\sigma_0 \sim 15 \mu\text{m}$ of the first measurement point on the track and multiple scattering contributions to the IP extrapolation, which in turn will be given by

$$\sigma_{ms} = \frac{0.014r\sqrt{x}}{\beta pc \sin^{5/2}\theta} \text{ cm} \quad (18)$$

where r is the extrapolation radius, x is the amount of intervening material (% radiation

length), and momentum is in GeV/c . For example, a $1 \text{ GeV}/c$ track at $\theta = 90^\circ$ with a first measurement point at $r = 2.5 \text{ cm}$ ($\sigma_0 = 15 \mu\text{m}$) and then extrapolated to the IP through a double-walled beryllium beam pipe with water cooling (about 1.13% of a radiation length) will have impact parameters (d_0, z_0) determined with $50 \mu\text{m}$ resolution. Thus, for a fully reconstructed B meson candidate, one might expect to reconstruct the spatial position of its decay vertex to a precision of $50\text{--}100 \mu\text{m}$, recalling that many of its decay daughters will have momentum well under $1 \text{ GeV}/c$. A simulation of the angular and momentum dependence of the impact parameter resolution for this configuration is shown in Figure 17.

Armed with an understanding of the factors that impact the vertex separation resolutions, we should now examine whether the CP violation measurement remains possible for a real colliding detector. With $1\text{--}2 \text{ A}$ of circulating current and significant nearby sources of synchrotron radiation, it is not possible to design an IP beam and shielding scheme with a radius smaller than $2\text{--}3 \text{ cm}$. Figure 18 shows the impact of degrading vertex performance by varying this basic design parameter for the B Factory detectors. As can be seen in this simulation of a CP asymmetry measurement, the fractional

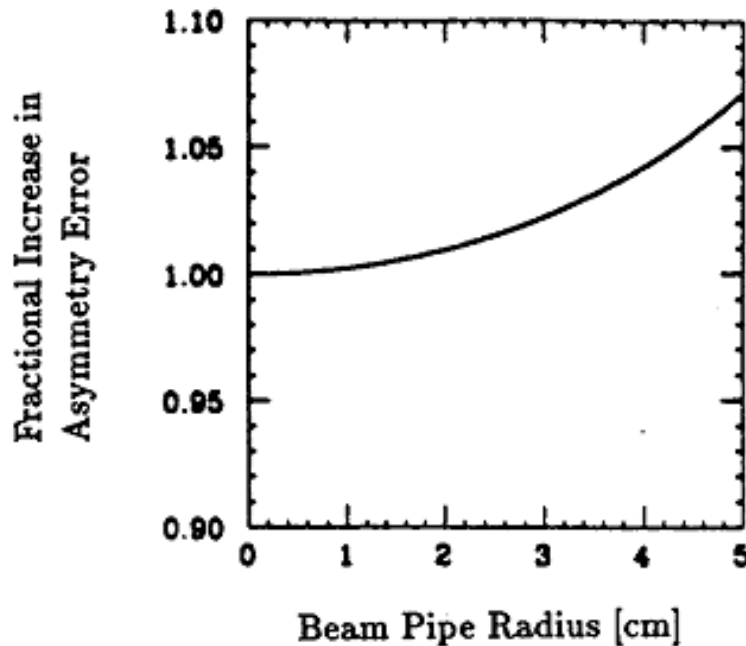


Fig. 18. Fractional increase in the error on the CP asymmetry amplitude as a function of the beam pipe radius and therefore the resolution on Δt .

increase in the error is not a strong function of r , despite the linear dependence on r for $\sigma_{x,y}$ and σ_z . However, the CP asymmetry measurement is feasible as long as the proper time resolution is smaller than the oscillation length of the sinusoidally varying CP amplitude, which is not an overly ambitious requirement on the scale of feasible Δz resolution.

3.1.3 Particle identification requirements

Identification of electrons, muons and kaons is an essential ingredient in both B reconstruction and flavor tagging. Particle species can be distinguished by measurements of the specific energy loss (dE/dx) in tracking systems, Cherenkov light in suitable radiators, electromagnetic shower energy and distribution in calorimeters, and particle penetration length in material. Selection criteria are based on these quantities, on likelihood ratios derived from them, or on neural network algorithms combining different detector likelihoods. Typically, looser selection criteria are applied for B reconstruction than for B -flavor tagging. Efficiencies and particle misidentification probabilities are determined from data control samples with similar characteristics.

Lepton identification over the momentum range of interest involves well understood detector techniques. High efficiencies and relatively low mis-identification rates can be achieved for electrons from about about 500 MeV/ c with dE/dx and calorimetry and for muons from about 1.1 GeV/ c with detector systems embedded in the iron flux return of magnets.

Figure 19 illustrates three basic processes where hadron identification is required. The upper plot shows the momentum distribution for all kaons from B decays, where PID up to 1–1.5 GeV/ c would be sufficient to exploit kaon charge for tagging purposes. About 40–50% of this range can be covered with dE/dx , while the upper end would require excellent time-of-flight or some other system. The middle plot shows the much harder pion momentum distribution for the charmless two-body decay $B^0 \rightarrow \pi^+\pi^-$, which is similar to the kaon distribution in $B^0 \rightarrow K^+\pi^-$ channel. A two-body B meson decay that is reconstructed with the wrong daughter mass assignment will only be marginally distinguishable from the correct assignment on the basis of the B candidate energy. Hadron identification in the range 2–4 GeV/ c is essential to achieve clean separation for these $b \rightarrow u$ modes. Other two-body decays with charm produce a somewhat softer kaon spectrum, as illustrated in the lower plot, but not by much.

We conclude that hadron particle identification over the full momentum range up to

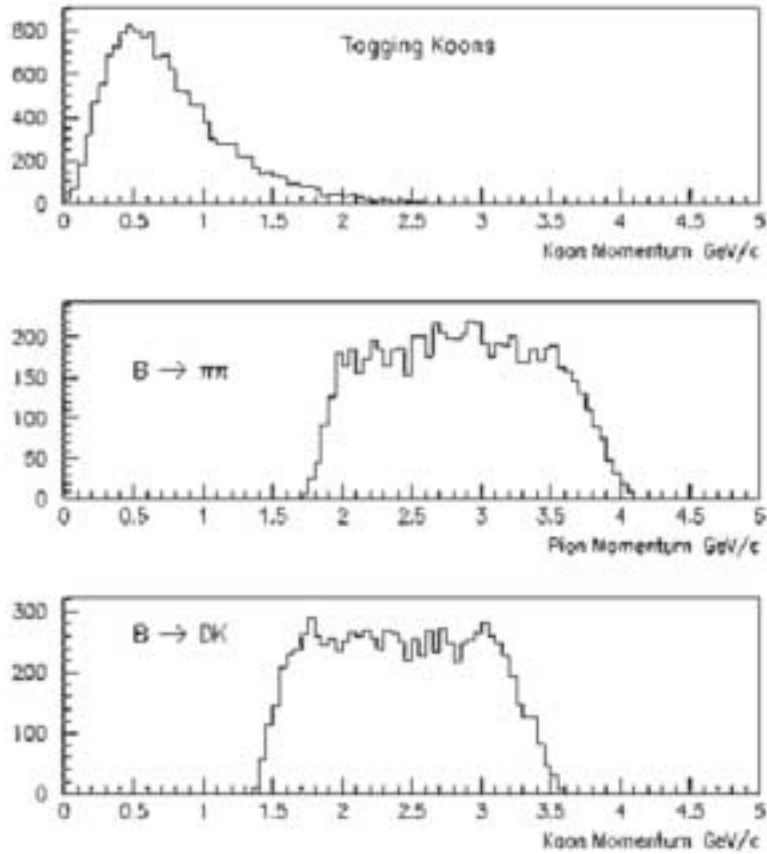


Fig. 19. Requirements for particle identification as derived from the momentum spectrum for hadrons in B decays: (upper) momentum distribution for all kaons from B decays; (middle) pion momentum distribution for the charmless two-body decay $B^0 \rightarrow \pi^+\pi^-$; and (bottom) kaon momentum distribution for two-body charm mode $B \rightarrow DK$.

4 GeV/ c is needed at the asymmetric energy B Factories. This is a technically challenging requirement, given the constraints of a colliding beam environment and the need to minimize material in the active volume. *BABAR* and Belle have addressed this particular challenge in distinctly different manners.

3.2 Implementation at *BABAR*

The *BABAR* detector³³ is one of two B Factory detectors that has been designed and built with these requirements in mind. Figure 20 shows a cross sectional view of the detector. Charged particles are detected and their momenta measured by a combination

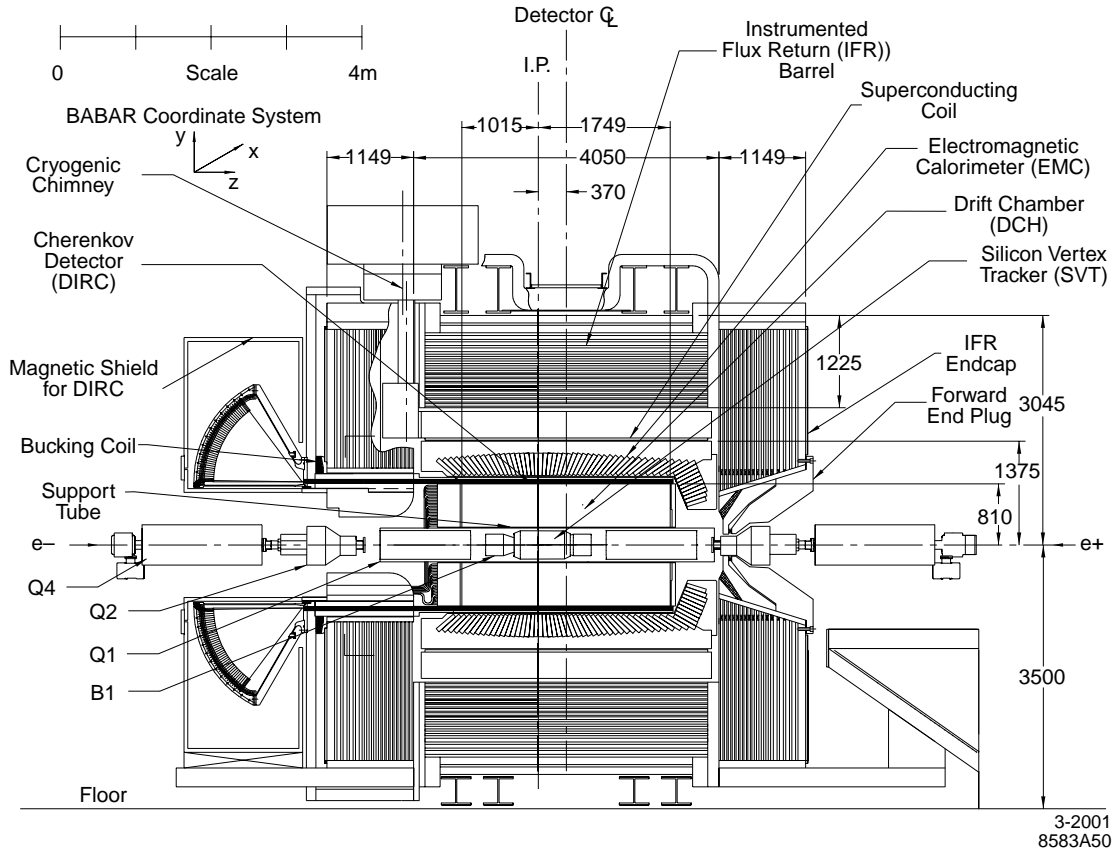


Fig. 20. Cross sectional view of the *BABAR* detector.

of a 40-layer, small-celled drift chamber (DCH) filled with a 80:20 helium:isobutane gas mixture, and a five-layer silicon vertex tracker (SVT), consisting of 340 AC-coupled double-sided silicon microstrip sensors in the radial volume between 3.2 and 11.4 cm. A cross sectional view of the SVT layout can be seen in Figure 21. The forward section of the outer two layers are arranged in a lampshade, in order to keep a near perpendicular angle of incidence on the silicon detectors. The single point resolution for each of the layers, shown in Figure 22, clearly meets the requirements discussed in Section 22. Note that with 5 layers, the SVT is capable of standalone tracking. This has particular advantages for detecting the soft charged pion in the decay $D^{*+} \rightarrow D^0 \pi^+$ transition, which often cannot be reconstructed in the drift chamber due to the 1.5-T magnetic field.

The 7104 cells of the DCH are organized into 10 superlayers in the radial volume between 23.6 and 80.9 cm within which the 2.7-m long sense wires all have the same orientation, thereby allowing segment-based tracking. Both the DCH and the SVT lie

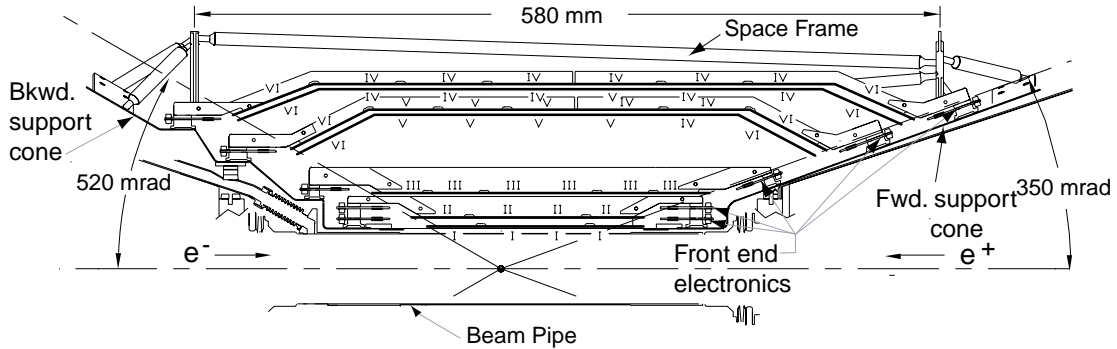


Fig. 21. Cross sectional view of the silicon vertex tracker at *BABAR*, showing 5 layer arrangement of AC-coupled double-sided silicon microstrip detectors.

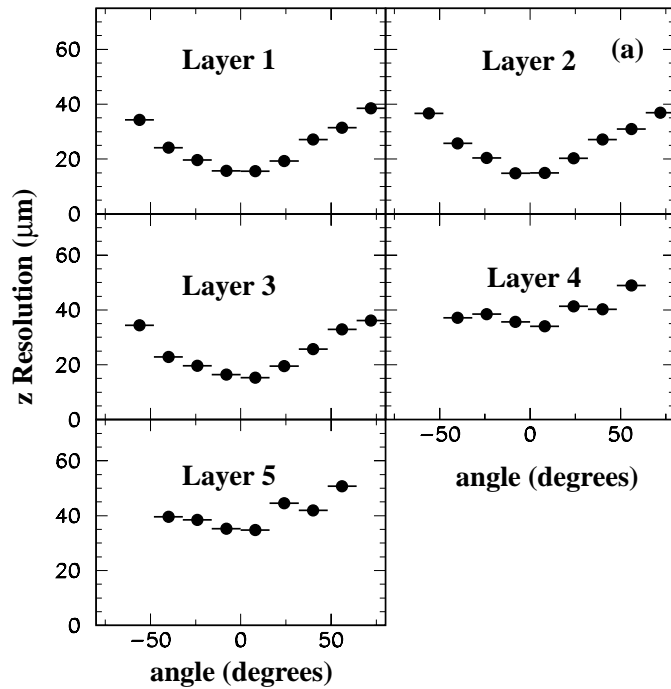


Fig. 22. Observed single point resolution in the z direction for the 5 different layers of the SVT as a function of the angle of incidence.

inside a 1.5-T solenoidal magnetic field. The tracking system covers the laboratory polar angle range from 17 to 153° (20 to 150° for the SVT) with respect to the beam direction. The impact parameter resolution is 55 μm at 1 GeV/ c and the momentum resolution is found to be $\sigma_{p_T}/p_T = (0.45 + 0.13p_T)\%$ where p_T is measured in GeV/ c .

Beyond the outer radius of the DCH is a detector of internally reflected Cherenkov radiation (DIRC), which is used primarily for charged-hadron identification. The device consists of 144 fused silica quartz bars in which relativistic charged particles above the Cherenkov threshold radiate photons while traversing the material. The light is transported by total internal reflection down the length of the bars to an array of 10752 photomultiplier tubes mounted on the rear of the detector, where the opening angle of the Cherenkov ring is measured. The DIRC and the hadron identification performance of *BABAR* will be discussed in further detail below.

A finely segmented electromagnetic calorimeter (EMC), consisting of 6580 CsI(Tl) crystals, is used to detect photons and neutral hadrons, and also to identify electrons. This device provides coverage over the polar angle range 16 to 153° and detects electromagnetic showers with a resolution of $\sigma_E/E = (1.85 \oplus 2.32/E^{1/4})\%$ where E is in GeV. The EMC is surrounded by a thin cylindrical superconducting coil and a segmented iron flux return, organized into a hexagonal barrel and two endcaps. The instrumented flux return (IFR) consists of multiple layers of resistive plate chambers (RPCs) interleaved with the flux-return iron and is used in the identification of muons and neutral hadrons.

Details of the design and performance of all *BABAR* detector systems, including backgrounds and IP design, trigger, data acquisition, and offline computing, are available³³ in the literature.

3.3 Implementation at Belle

The Belle detector³⁴ shares the same optimization for B decays into neutral and charged final states daughters in a boosted $\Upsilon(4S)$ system. Figure 23 shows a cross sectional view of the detector. Charged particles are detected and their momenta measured by a combination of a 50-layer, small-celled drift chamber (CDC) filled with a 50:50 helium:ethane gas mixture, and a three-layer silicon vertex tracker (SVD), consisting of 8, 10, and 14 ladders of Hamamatsu AC-coupled double-sided silicon microstrip sensors (105 in total) at 3.0, 4.55, and 6.05 cm radius. A cross sectional view of the SVT layout can be seen in Figure 24.

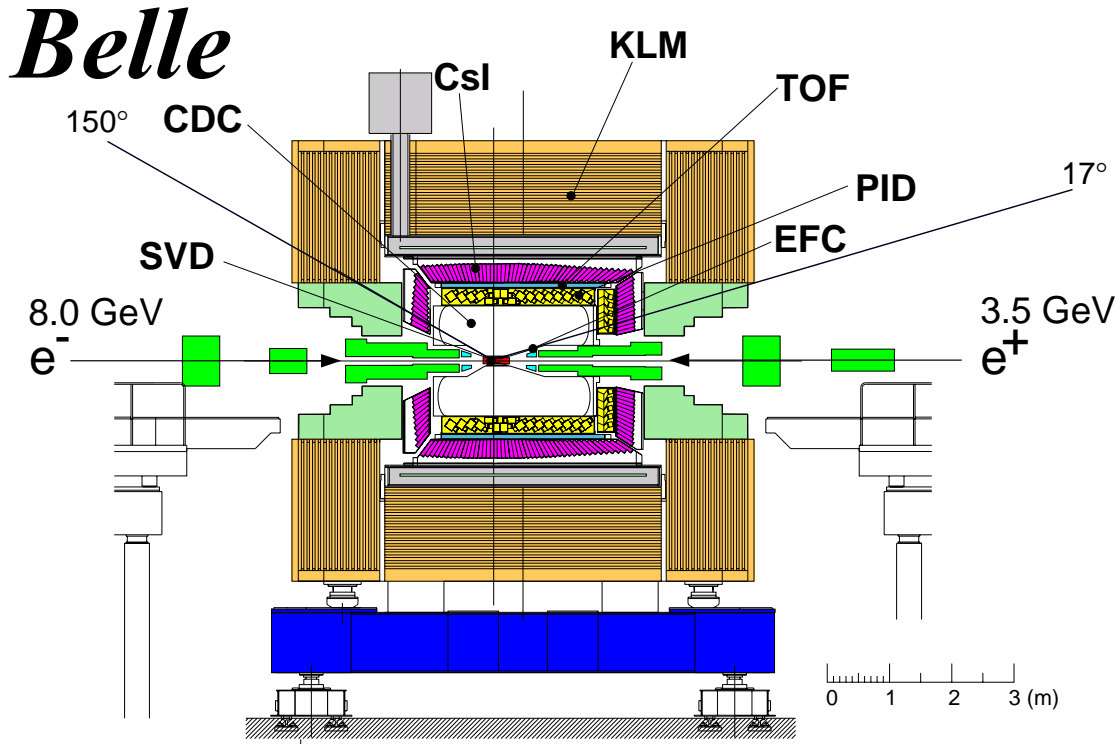


Fig. 23. Cross sectional view of the Belle detector.

The 8400 cells of the CDC are organized into axial (11) and stereo (10) superlayers in the radial volume between 8.3 and 86.3 cm, with a conical inner section to clear accelerator components and an outer 2.4-m long cylindrical section. A cross sectional view of the CDC layout can be seen in Figure 25. Both the CDC and the SVD lie inside a 1.5-T solenoidal magnetic field. The tracking system covers the laboratory polar angle range from 17 to 150° (27 to 139° for the SVD) with respect to the beam direction, or 92% of the full solid angle in the $\Upsilon(4S)$ center-of-mass system. The impact parameter resolution is 55 μm at 1 GeV/c and the momentum resolution is found to be $\sigma_{p_T}/p_T = (0.30/\beta \oplus 0.19p_T)\%$ where p_T is measured in GeV/c.

Outside the CDC are two dedicated hadron identification systems: an array of 128 time-of-flight counters (TOF) with 100 ps timing resolution and a set of 1188 silica aerogel threshold Cherenkov counters (ACC) with fine mesh phototubes for photon detection. These detectors and the hadron identification performance of Belle will be discussed in further detail below.

A CsI(Th) electromagnetic calorimeter (ECL) is located outside these systems and

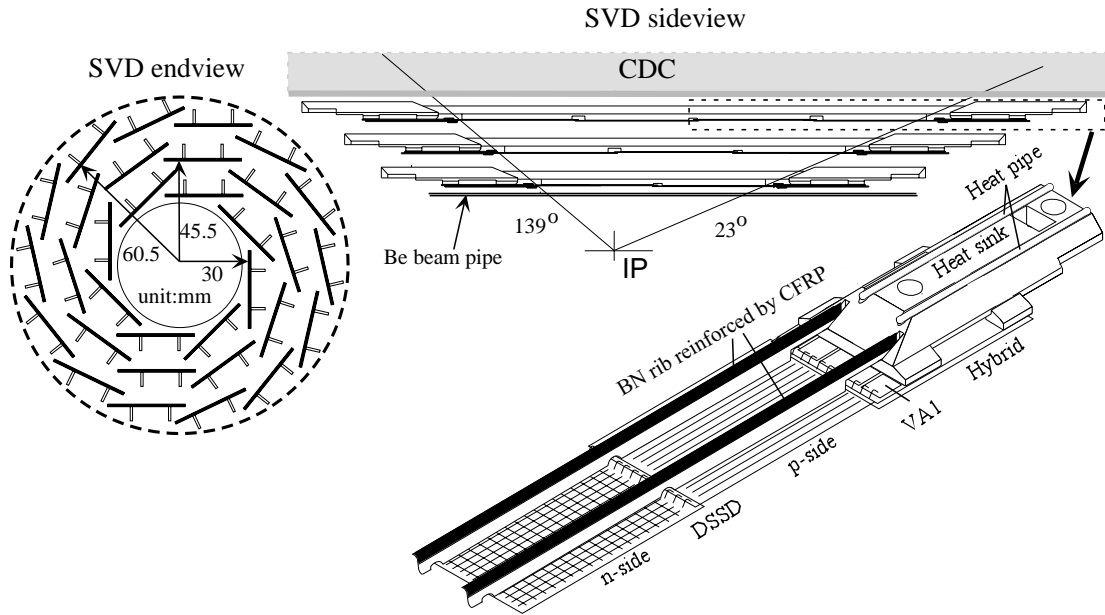


Fig. 24. Cross sectional view of the silicon vertex detector at Belle, showing 3 layer arrangement of AC-coupled double-sided silicon microstrip detectors.

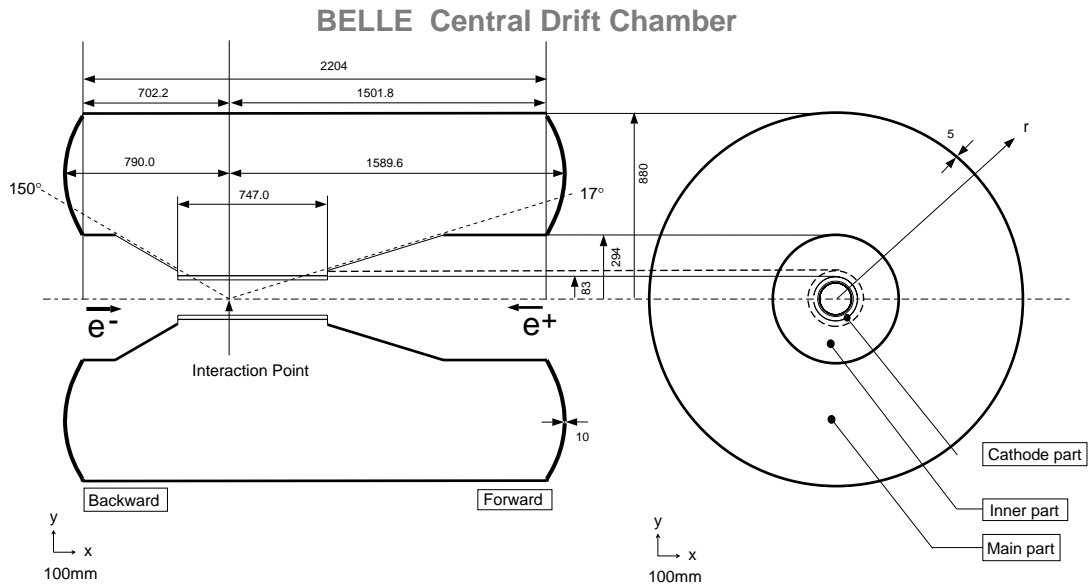


Fig. 25. Cross sectional and end views of the central drift chamber at Belle, showing conical insert to enable tracking down to 8.8 cm from the beamline.

inside the solenoid coil. This device provides coverage over the same solid angle range as the tracking system and detects electromagnetic showers with a resolution of $\sigma_E/E = (1.3 \oplus 0.07/E \oplus 0.8/E^{1/4})\%$ where E is in GeV. The iron flux return is segmented into 14 layers of 4.7 cm-thick iron to allow instrumentation with resistive-plate chambers (KLM). This serves both to allow muon identification and crude hadronic calorimetry for K_L^0 reconstruction.

Details of the design and performance of all Belle detector systems, including backgrounds and IP design, trigger, data acquisition, and offline computing, are available³⁴ in the literature.

3.4 Hadron identification

As already noted, the hadron identification requirements for the B Factory detectors represent a significant technical challenge. It is useful to examine the clever solutions that have been devised to provide kaon identification up to 4 GeV/ c .

3.4.1 The DIRC at BABAR

The DIRC provides $BABAR$ with a powerful detection system for hadron identification, based on the novel idea of using quartz bars both as a radiator of Cherenkov light and as a means of transporting that light outside the magnetic field volume of the detector by total internal reflection. The basic concept is illustrated in Figure 26. A particle traversing the quartz bar above the Cherenkov threshold will produce light at the characteristic angle

$$\cos \theta_c / n\beta \tag{19}$$

where n is the index of refraction of the material. Some of these photons will lie within the total internal reflection limit, with the fraction dependent on the angle of incidence of the particle. As the light reflects off the surfaces of the bar, the Cherenkov angle information will be preserved as the light reflects down the length of the bar until it can be imaged onto a toroidal array of phototubes. To avoid instrumenting both ends of the bar with photon detectors, a mirror is placed at the forward end, perpendicular to the bar axis, to reflect incident photons to the backward, instrumented end. Fused synthetic silica is used for the bar material, because of its resistance to ionizing radiation, its long attenuation length, large index of refraction, and low chromatic dispersion within the detection wavelengths of the DIRC, and the ability to create an excellent optical finish on its surfaces.

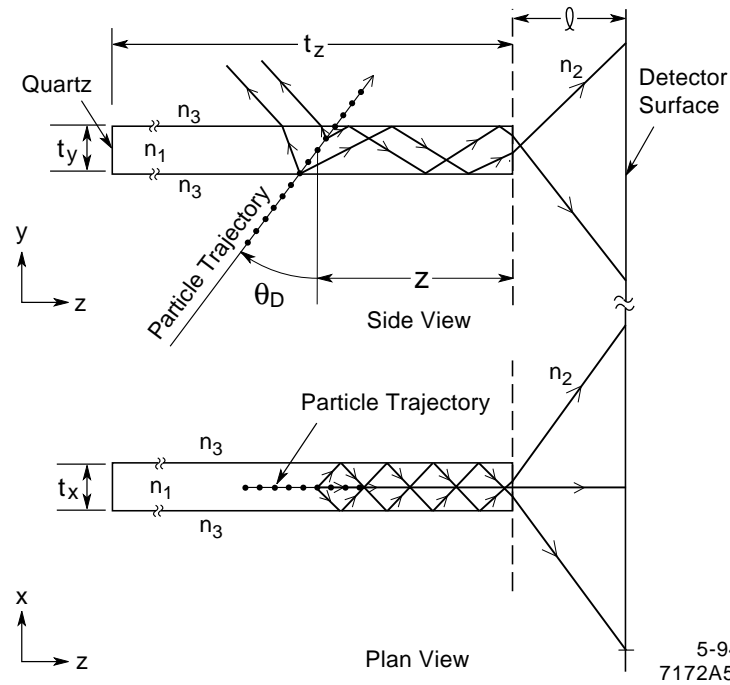


Fig. 26. Illustration of DIRC principle, showing creation of cherenkov light in quartz, transport down the length of the bar by internal reflection, and then emerging image with preserved angular information at the end of the bar.

As shown in Figure 27, once photons arrive at the instrumented end, they emerge into a water-filled region which allows the image to magnification of the image and provides good optical coupling. The photons are detected by an array of densely packed photomultiplier tubes (PMTs), each surrounded by reflecting light catcher cones to capture light that would miss the active area of the PMT. The PMTs are about 1.2 m from the end of the bars. The expected Cherenkov light pattern at the PMT surface is essentially a conic section, where the cone opening-angle is the Cherenkov production angle modified by refraction at the exit from the bar. A fused silica wedge at the exit of the bar reflects photons at large angles relative to the bar axis, thereby improving photon acceptance at the phototube array. A complete view of all the DIRC detector elements is shown in Figure 28.

Accounting for attenuation losses, reflection coefficients, geometric phototube packing fractions, trapping probabilities for internal reflection, and quantum efficiency of the photocathodes, an minimum of 20 photoelectrons are produced for a $\beta = 1$ track at normal incidence to the bar center. This number increases by about a factor of three for

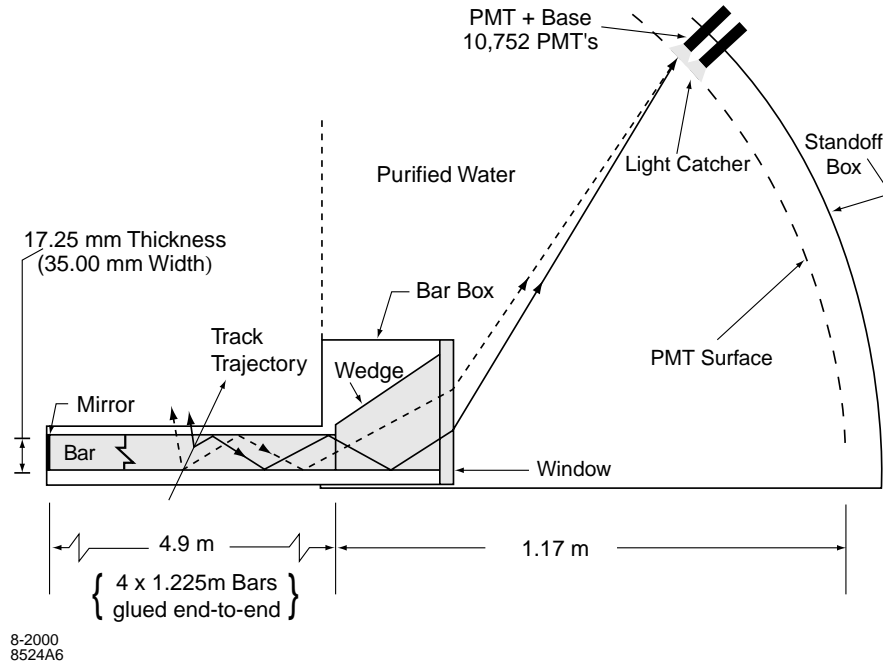


Fig. 27. Schematic diagram of quartz radiator and imaging system for the DIRC detector at *BABAR*.

the larger entrance angles in the forward and backward directions. The observed phototube hits can be transformed into measurements of Cherenkov angle with respect to known track directions, where ambiguities and backgrounds are substantially reduced by determining the transit time for the Cherenkov photons with a resolution of about 1.7 ns.

An example of the discriminating power of the DIRC is illustrated in Figure 29, where the measured Cherenkov angle is shown as a function of momentum. The left-hand panel is for kinematically identified π^+ from the decay $D^{*+} \rightarrow D^0(\rightarrow K^-\pi^+)\pi_s^+$, while the right-hand panel is for the K^- . Clearly it is possible to distinguish pions from kaons up to 4 GeV/c, as demonstrated by the π - K separation power shown in Figure 30.

In addition to the number of Cherenkov photons and the Cherenkov angle in the DIRC, kaons can be distinguished from pions and protons at *BABAR* on the basis of specific energy-loss measurements dE/dx in SVT and DCH. The difference between the measured truncated-mean dE/dx in the DCH and the expected mean for the pion, kaon and proton hypothesis, with typical resolution of 7.5%, is used to compute likelihoods \mathcal{L}_π , \mathcal{L}_K and \mathcal{L}_p assuming Gaussian distributions. Similarly, the difference between the measured 60% truncated-mean dE/dx in the SVT and the expected dE/dx is

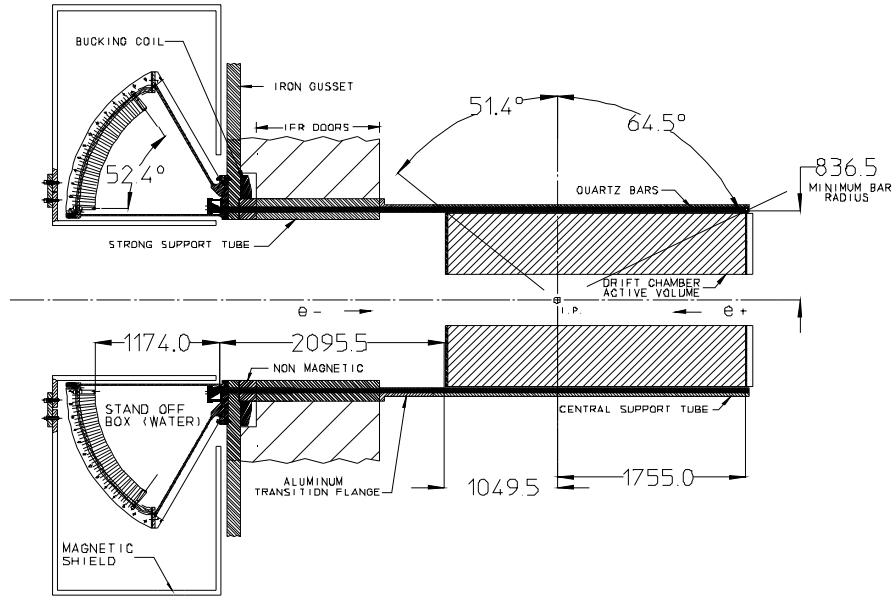


Fig. 28. Elevation view of the complete DIRC system, including central support tube with quartz bars bundled into bar boxes, strong support tube for mechanical support, and toroidal water-filled stand-off box with the phototube readout array.

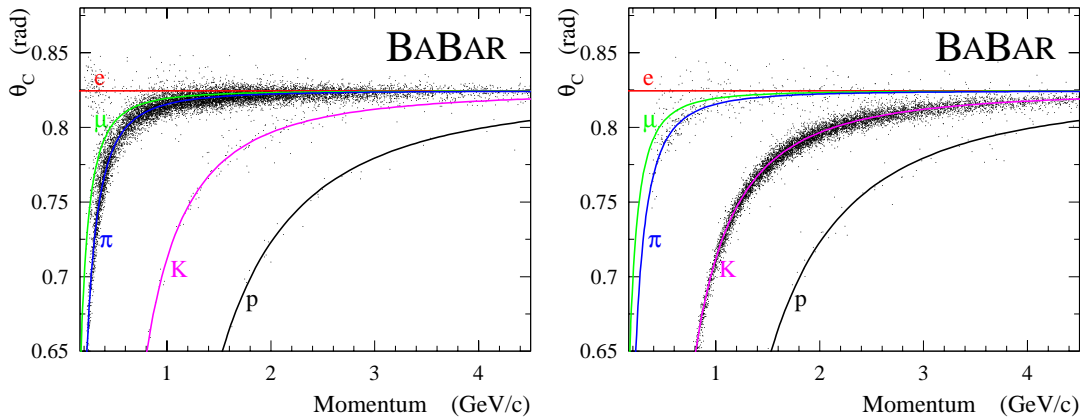


Fig. 29. Distribution of observed DIRC Cherenkov angle versus momentum for kinematically identified pions (left) kaons (right) in the decay $D^{*+} \rightarrow D^0 \pi^+$ followed by $D^0 \rightarrow K^- \pi^+$. The D^0 signal has a combinatorial background of about 10%.

described by an asymmetric Gaussian distribution. For minimum-ionizing particles the resolution on the SVT truncated mean is about 14%. In the DIRC, a likelihood is obtained for each particle hypothesis from the product of two components: the expected

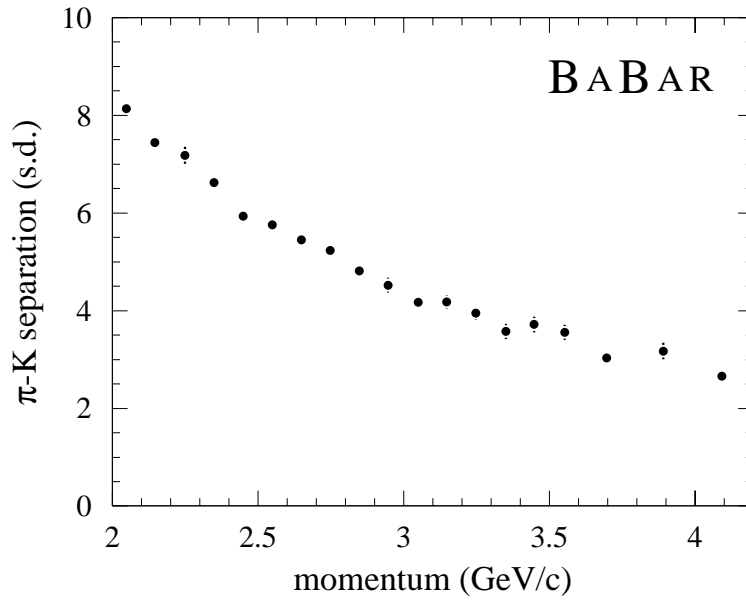


Fig. 30. π - K separation power in standard deviations from the kinematically tagged D^{*+} sample.

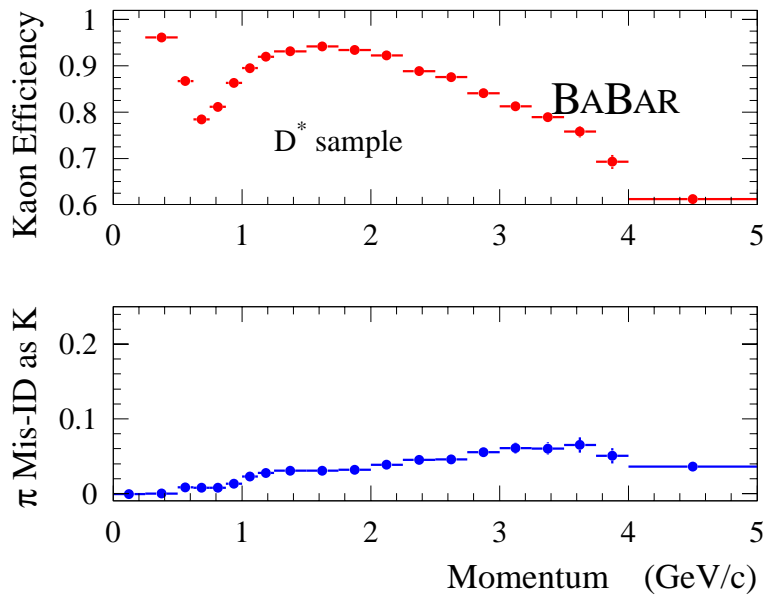


Fig. 31. Kaon identification performance obtained from combined particle identification systems at *BABAR* on the basis of a neural network algorithm.

number of Cherenkov photons, with a Poisson distribution, and the difference between the measured average Cherenkov angle to the expected angle for a given mass hypothesis, assuming a Gaussian distribution. The combined efficiency and misidentification rate available for tagging purposes with this method is shown in Figure 31.

3.4.2 Aerogel Cherenkov Counters and TOF System at Belle

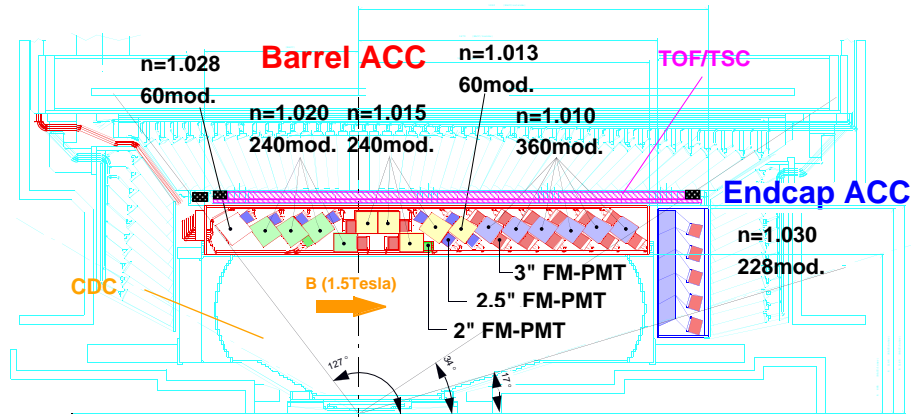


Fig. 32. Elevation view of Aerogel Cherenkov Counter and Time-of-Flight system at Belle.

Belle has opted for two detector systems devoted to hadron identification. The configuration of the two systems is shown in cross-section in Figure 32.

The first detector is an innovative Aerogel Cherenkov Counter (ACC) system, which is based on the collection of Cherenkov light produced in blocks of low-density silica aerogel and detected with fine-mesh (FM) photomultiplier tubes operating in the main 1.5-T solenoidal magnetic field. The barrel ACC consists of 960 modules, arranged in an array with 60-fold segmentation in azimuth and grouped by index of refraction in polar angle with $n = 1.028$ (60), $n = 1.020$ (240 modules), $n = 1.015$ (240 modules), $n = 1.013$ (60) and $n = 1.010$ from back to front. The forward endcap is covered by 228 modules with $n = 1.030$ arranged in 5 concentric layers. Aerogels of such low densities are not available commercially. Instead a new production method was developed in-house at KEK. In addition, a special surface treatment was also devised to avoid degradation of aerogel transparency through aging due to the hydrophilic nature

of the material. In seven months of operation, a total of 2 m^2 of silica aerogel was produced. Five tiles of aerogel are stacked in a single module of dimension $12 \times 12 \times 12 \text{ cm}^3$, which is viewed by either two (barrel modules) or one (endcap modules) FM-phototube.

Extensive simulations have been performed to model the light transport in the aerogel and the collection by the FM-phototubes. Treating absorption in aerogel as the only free parameter, the light yields are reproduced to 5%. Test beam results for a $n = 1.015$ ACC module show 20.3 photoelectrons without magnetic field in Figure 33 and three sigma pion-proton separation in a 1.5-T field. The observed average number of photoelectrons in the barrel and endcap modules of the ACC can be seen in Figure 34 to vary from a minimum of 10 in some barrel modules to a typical 25 in the endcap.

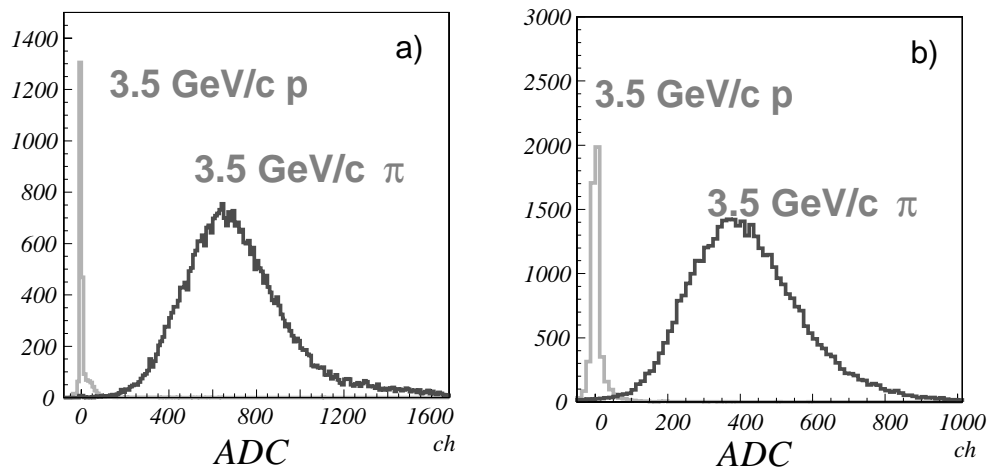


Fig. 33. Pulse-height spectra for 3.5 GeV/c pions (above threshold) and protons (below threshold) obtained with a single ACC module with $n = 1.015$ (a) without magnetic field and (b) with a 1.5-T field.

The second detector is a high-precision time-of-flight (TOF) system. A 100 ps resolution at a flight distance of 1.2 m from the IP allows good hadron identification below about 1.2 GeV/c. In total there are 64 barrel modules in azimuth, each consisting a thin trigger scintillation counter (TSC) in front and two trapezoidal time-of-flight counters (TOF) behind. The TOF counters are from long-attenuation length BC408 of dimension ($T \times W \times L$) $4 \times 6 \times 255 \text{ cm}$ and are readout with FM-phototubes at both ends.

The hadron identification information from the ACC and TOF systems is combined with specific energy-loss measurements dE/dx in the CDC. The difference between

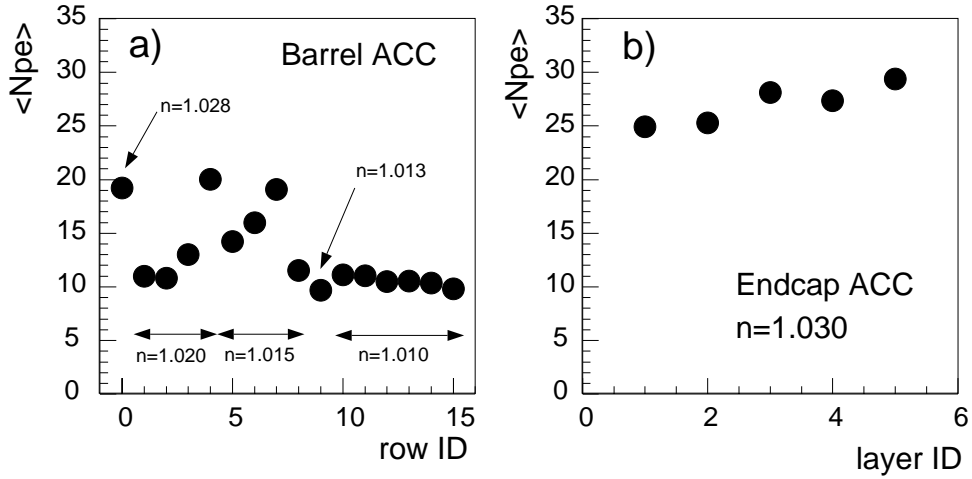


Fig. 34. Average number of photoelectrons per ACC module for (a) each row in the barrel and (b) each layer in the endcap.

the measured truncated-mean dE/dx in the DCH and the expected mean for the pion, kaon and proton hypothesis, with typical resolution of 6%. The performance of this combined system can be measured in data with the kinematically identified pions and kaons in the decay $D^{*+} \rightarrow D^0 \pi^+$ followed by $D^0 \rightarrow K^- \pi^+$. A scatter plot of the combined likelihood ratio $L(K)/(L(K) + L(\pi))$ is shown in Figure 35 as a function of momentum. The combined kaon efficiency and pion misidentification rate obtained from the D^{*+} sample is shown in Figure 36, where a requirement that $L(K) > 0.6$ has been applied. Clearly this system meets the requirements for tagging and discrimination between two-body B decays.

4 Reconstruction of B mesons

Neutral B mesons in flavor eigenstates are reconstructed in the hadronic final states $B^0 \rightarrow D^{(*)-} \pi^+$, $D^{(*)-} \rho^+$, $D^{(*)-} a_1^+$, and $J/\psi K^{*0} (K^+ \pi^-)$, and the semileptonic decay mode $B^0 \rightarrow D^{*-} \ell^+ \nu$. The CP sample is reconstructed in the channels $B^0 \rightarrow J/\psi K_S^0$, $\psi(2S) K_S^0$, $\chi_{c1} K_S^0$, $\eta_c K_S^0$, $J/\psi K^{*0} (K^{*0} \rightarrow K_S^0 \pi^0)$ and $J/\psi K_L^0$. In some cases, control samples of charged B decays are studied, where the hadronic final states $B^+ \rightarrow \bar{D}^{(*)0} \pi^+$, $J/\psi K^{(*)+}$, $\psi(2S) K^+$ and $\chi_{c1} K^+$ are used. All final-state particles, with the exception of the neutrino in the semileptonic decay, are reconstructed. A number of \bar{D}^0

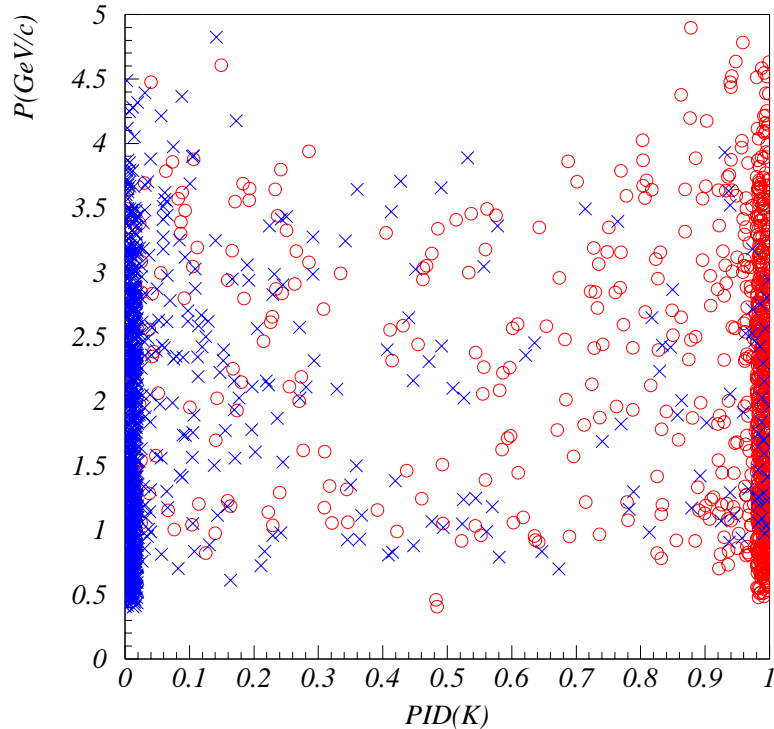


Fig. 35. Likelihood ratio $L(K)/(L(K) + L(\pi))$, computed from combined dE/dx , TOF, and ACC information, versus momentum for kinematically identified pions (marked by “x”) and kaons (marked by open circle) in the decay $D^{*+} \rightarrow D^0\pi^+$ followed by $D^0 \rightarrow K^-\pi^+$.

and D^- decay modes are used to achieve reasonable reconstruction efficiency despite the typically small branching fractions for any given B or D decay channel. In the following, kinematic quantities and selection criteria are given in the laboratory frame, unless otherwise specified.

4.1 Event selection

Multihadron events are selected by demanding a minimum number (typically 3) of reconstructed charged tracks in the polar angle range with active tracking coverage, which originate from the beamspot region. A primary vertex is formed on an event-by-event basis from a vertex fit to all charged tracks in the fiducial volume. Events are accepted if they have a primary vertex within nominal distance of the average position of the interaction point. Typically some additional requirement on the total energy

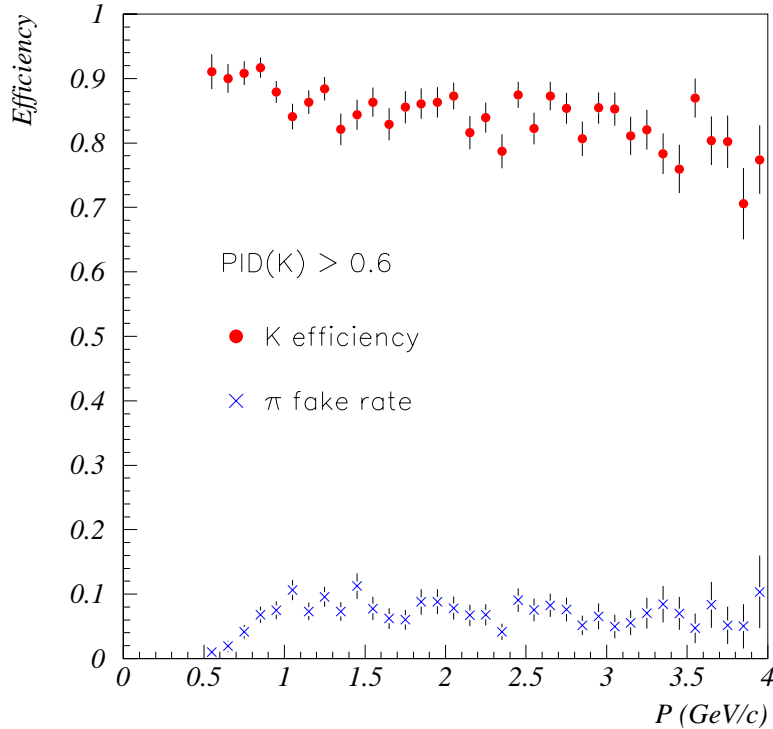


Fig. 36. Kaon efficiency and pion misidentification rate in the barrel region as obtained from $D^{*+} \rightarrow D^0(\rightarrow K^-\pi^+)\pi^+$ events. The combined likelihood ratio for the kaon hypothesis is required to be greater than 60%.

for charged tracks and neutrals is also made. To reduce continuum background, a requirement is made on the normalized second Fox-Wolfram moment³⁵ R_2 of the event, calculated with both charged tracks and neutrals. The ℓ^{th} Fox-Wolfram moment is the momentum-weighted sum of Legendre polynomial of the ℓ^{th} order computed from the cosine of the angle between all pairs of tracks. The ratio R_2 provides good separation between jet-like continuum events and more spherical $B\bar{B}$ events. Typically requiring $R_2 < 0.5$ is quite efficient for $B\bar{B}$ events while rejecting continuum, as shown in Figure 37.

4.2 Reconstruction of decay daughters

The reconstruction of B mesons typically involves the summation of a set of related decay modes, with multiple decay chains for the charm daughters or other short-lived decay products. Vertex and kinematic fitting is used to improve four-momenta and

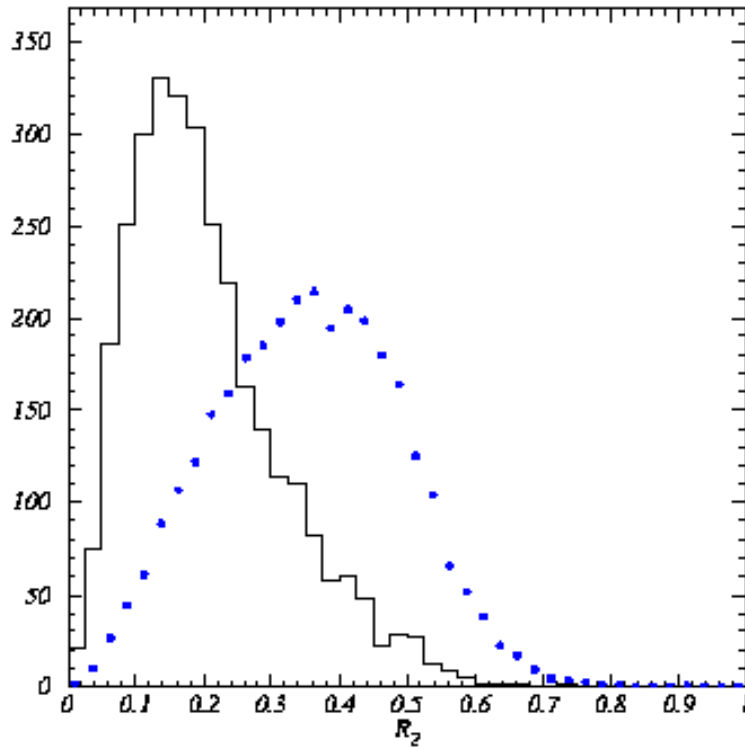


Fig. 37. Distribution of the ratio of the second-to-first Fox-Wolfram moments R_2 for $\Upsilon(4S) \rightarrow B\bar{B}$ events (histogram) and continuum $e^+e^- \rightarrow q\bar{q}$ (dots).

position measurements, as well as to measure the time difference between decaying B hadrons in the $\Upsilon(4S) \rightarrow B\bar{B}$ decay. For example, in the case of $B^0 \rightarrow J/\psi K_s^0$, the position measurement of the B^0 can be improved with the constraint that the line-of-flight of the K_s^0 intersects the J/ψ vertex. The energy resolution of the B^0 can also be improved by applying a mass constraint to the J/ψ and K_s^0 daughters. Likewise, mass constraints are applied to other intermediate charm states or to neutral pions formed from two photons.

4.2.1 K_L^0 selection

Candidates for K_L^0 mesons are identified in the calorimeter (EMC at *BABAR* or ECL at Belle) and flux-return detectors (IFR at *BABAR* or KLM at Belle) as reconstructed clusters that cannot be associated with any charged track in the event. We will examine the requirements at *BABAR*, although the approach is similar at Belle.

In the EMC, candidates must satisfy a basic requirement of cluster energy between

200 MeV and 2 GeV to be consistent with a K_L^0 shower. Since the dominant source of background is photons from neutral pions, K_L^0 candidates consistent with a being a photon are paired with other neutrals with $E_\gamma > 30$ MeV. Any candidate with $100 < m(\gamma\gamma) < 150$ MeV/ c^2 is rejected. Likewise, clusters with more than 1 GeV energy that contain two bumps are rejected if the bump energies and shower shapes are consistent with two photons from a π^0 decay. Monte Carlo simulation shows that clusters due to true K_L^0 mesons are easily distinguished from π^0 candidates by these criteria. The remaining background consists primarily of photons and overlapping showers. Isolated clusters produced by charged hadrons are removed by the basic clustering algorithm, which requires a minimum separation of about 20 cm between clusters.

IFR candidates are defined as clusters with hits in two or more RPC layers that are not matched to any reconstructed charged track. To reduce beam-related backgrounds and to avoid regions where the charged tracking efficiency is low, the polar angle θ of the IFR cluster must lie in the range $-0.75 < \cos \theta < 0.93$, and clusters that begin in the outer 25% of the forward IFR endcap are removed. Due to the irregular structure of hadronic showers, some hits from charged tracks are missed by the tracking association. These clusters can be removed by rejecting K_L^0 candidates that lie within ± 350 mrad in polar angle and in the range $-750(-300)$ to $+300(+750)$ mrad in azimuth of the EMC intersection of any positively (negatively) charged track in the event. The remaining background is predominantly from charged particles and detector noise.

4.2.2 Charmed meson and charmonium reconstruction

The decay channels $K^+\pi^-$, $K^+\pi^-\pi^0$, $K^+\pi^+\pi^-\pi^-$ and $K_S^0\pi^+\pi^-$ are commonly used to reconstruct \bar{D}^0 candidates, while D^- candidates are selected in the $K^+\pi^-\pi^-$ and $K_S^0\pi^-$ modes. These modes represent a combined branching fraction of about 28% for the \bar{D}^0 and 12% for the D^- . For $\bar{D}^0 \rightarrow K^+\pi^-\pi^0$, the dominant resonant mode is $\bar{D}^0 \rightarrow K^+\rho^-$, followed by $\rho^- \rightarrow \pi^-\pi^0$. This allows the angle $\theta_{D^0\pi}^*$ between the π^- and \bar{D}^0 in the ρ^- rest frame to be used as a discriminant against background.

Candidates for D^{*-} mesons are formed in the decay $D^{*-} \rightarrow \bar{D}^0\pi^-$ by combining a \bar{D}^0 with an additional pion. This soft pion is constrained to originate from the beamspot when the D^{*-} vertex is computed. After applying a mass-constrained fit to the \bar{D}^0 daughter, D^{*-} candidates are required to have $m(\bar{D}^0\pi^-)$ within about 1 MeV/ c^2 . This narrow width is a powerful technique for rejected combinatorial background.

\bar{D}^{*0} candidates are formed by combining a \bar{D}^0 with a soft π^0 . In this case, \bar{D}^{*0}

candidates are required to have $m(\bar{D}^0\pi^0)$ within about $\pm 4 \text{ MeV}/c^2$ of the nominal value, after applying a mass-constrained fit to the \bar{D}^0 daughter.

Candidates for J/ψ and $\psi(2S)$ mesons are reconstructed in their e^+e^- and $\mu^+\mu^-$ decay modes, while $\psi(2S)$ mesons are also reconstructed in the $J/\psi\pi^+\pi^-$ channel. In order to improve acceptance, it is common that only one of the two lepton daughters must be positively identified; the other need only be consistent. For $J/\psi \rightarrow e^+e^-$ and $\psi(2S) \rightarrow e^+e^-$ decays, where the electron may have radiated Bremsstrahlung photons, the missing energy can be recovered by identifying neutral calorimeter clusters within suitable polar and azimuthal angular ranges. The inclusive J/ψ signal obtained at *BABAR* is shown in Figure 38a,b.

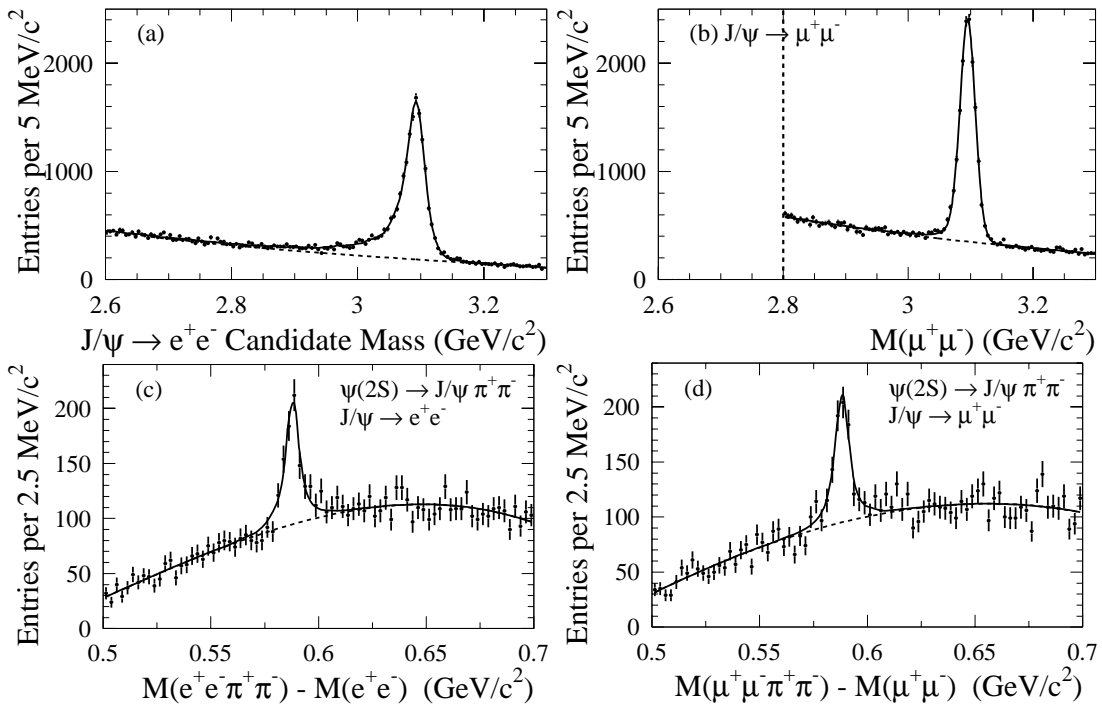


Fig. 38. Inclusive charmonium production as reconstructed in the $J/\psi \rightarrow e^+e^-$, $J/\psi \rightarrow \mu^+\mu^-$, and $\psi(2S) \rightarrow J/\psi\pi^+\pi^-$ channels [*BABAR*].

For the $\psi(2S) \rightarrow J/\psi\pi^+\pi^-$ mode, J/ψ candidates are constrained to the nominal mass and then combined with pairs of oppositely-charged tracks considered as pions. Candidates with a mass difference $m(J/\psi\pi^+\pi^-) - m(J/\psi)$ consistent with the known value are retained. The inclusive $\psi(2S)$ signal obtained at *BABAR* is shown in Figure 38c,d.

Photon candidates used for the reconstruction of $\chi_{c1} \rightarrow J/\psi\gamma$ should not form, in

combination with any other photon in the event having an appropriate minimum energy, a π^0 candidate.

4.3 B meson selection in fully-reconstructed modes

Candidates for B decays in all modes except $B^0 \rightarrow J/\psi K_L^0$ are identified with a pair of nearly uncorrelated kinematic variables: the difference ΔE between the energy of the B candidate and the beam energy in the $\Upsilon(4S)$ center-of-mass frame, defined as

$$\Delta E = E_B^* - E_{\text{beam}}^* \quad (20)$$

and the beam-energy substituted mass, m_{ES} , defined as

$$m_{\text{ES}} = \sqrt{(E_{\text{beam}}^*)^2 - (p_B^*)^2}, \quad (21)$$

where E_B^* and \mathbf{p}_B^* are the energy and momentum of the B candidate, and E_{beam}^* is the beam energy, all evaluated in the cms frame. In terms of these variables, the signal events will be found at $\Delta E \sim 0$ and $m_{\text{ES}} \sim m_B$ with resolutions given by

$$\begin{aligned} \sigma_{\Delta E}^2 &= \sigma_{\text{beam}}^2 + \sigma_E^2 \sim \sigma_E^2 \\ \sigma_{m_{\text{ES}}}^2 &= \sigma_{\text{beam}}^2 + \left(\frac{p}{m_B}\right)^2 \sigma_p^2 \sim \sigma_{\text{beam}}^2 \end{aligned} \quad (22)$$

Since $\sigma_E \gg \sigma_{\text{beam}} \gg \sigma_p$, this reduces to

$$\begin{aligned} \sigma_{\Delta E}^2 &\sim \sigma_E^2 \\ \sigma_{m_{\text{ES}}}^2 &\sim \sigma_{\text{beam}}^2 \end{aligned} \quad (23)$$

where the errors on ΔE and m_{ES} are largely uncorrelated. Thus, it is common to define a signal region in the $(m_{\text{ES}}, \Delta E)$ plane as $m_{\text{ES}} = m_B \pm 3\sigma_{m_{\text{ES}}}$ and $|\Delta E| < 3\sigma_{\Delta E}$. The value for $\sigma_{m_{\text{ES}}}$ is typically about $2.6 \text{ MeV}/c^2$, with slight variation between channels. On the other hand, $\sigma(\Delta E)$ varies between 7 to 40 MeV for typical modes. When multiple B candidates (with $m_{\text{ES}} > 5.20 \text{ GeV}/c^2$) are found in the same event, the candidate with the smallest value of $|\Delta E|$ is selected.

Two types of background in the sample of selected B^0 candidates are distinguished. The first background, called combinatorial, arises from random combinations of charged tracks and neutral showers from both B mesons in $B\bar{B}$ events or from continuum events. This background is smoothly distributed in m_{ES} and does not peak near the B mass. The second, so-called ‘‘peaking’’ background, consists of events in which, for

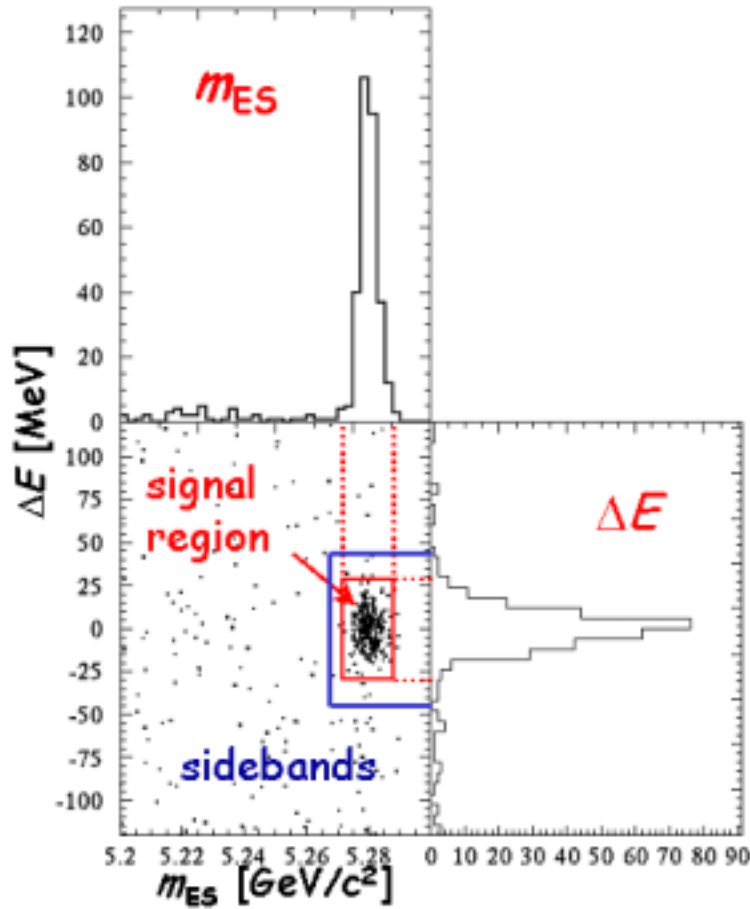


Fig. 39. Illustration of kinematic variables that are used to identify B candidates. Signal events appear inside the region centered at $|\Delta E| = 0$ and $m_{ES} = m_B$, shown by the inner box in the scatter plot and projected for corresponding slices in $|\Delta E|$ and m_{ES} onto the one-dimensional histograms. The region outside the outer box in the scatter plot can be used to extrapolate combinatorial background into the signal region.

example, a slow pion from the reconstructed B meson is replaced by a slow pion from the tagging B , causing an enhancement near the nominal B mass. The loss or addition of a soft pion track does not significantly alter the vertex for the B_{rec} candidate, since such tracks undergo significant multiple scattering and have large impact parameter errors. The peaking background from charged B decays is considered as a specific background source in the construction of the full likelihood function for B^0 - \bar{B}^0 mixing, since these events have a particular time structure and set of effective dilutions. In this case, the peaking background from other neutral B decays has time-dependent proper-

ties and dilutions that are essentially identical to the signal and is treated as such. For the likelihood describing the CP sample, the peaking background is simply assumed to have zero effective CP .

Suppression of continuum background, in addition to a general requirement on R_2 , is typically provided by restricting the thrust angle θ_{th} , defined as the angle between the thrust axis of the particles that form the reconstructed B_{rec} candidate and the thrust axis of the remaining tracks and unmatched clusters in the event, computed in the $\Upsilon(4S)$ frame. The two thrust axes are almost uncorrelated in $B\bar{B}$ events, because the B^0 mesons are nearly at rest in the $\Upsilon(4S)$ rest frame. In continuum events, which are more jet-like, the two thrust axes tend to have small opening angles. Thus, a requirement on the maximum value of $|\cos\theta_{th}|$ is effective in continuum rejection, as can be seen in Figure 40.

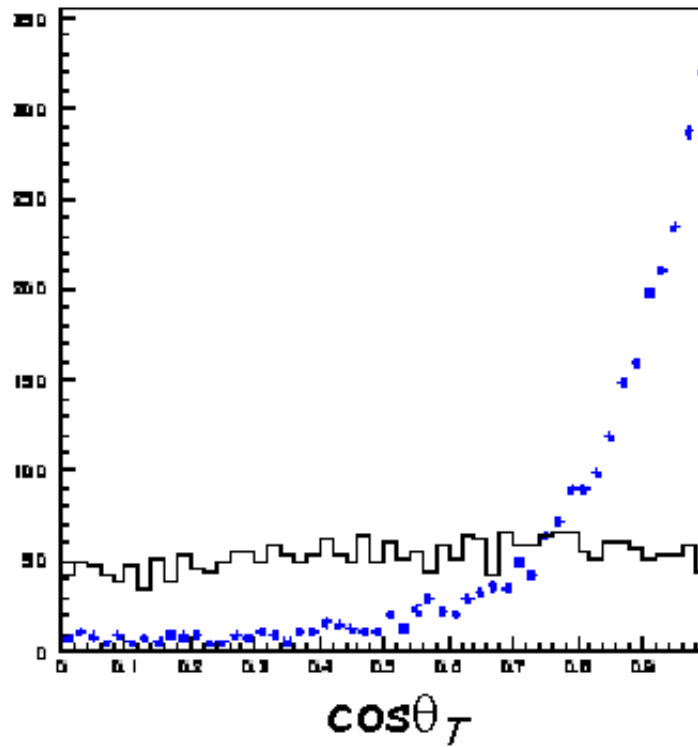


Fig. 40. Distribution of the cosine of the opening angle θ_T between the thrust axis of the B candidate and the thrust axis of the remaining charged tracks and neutral clusters in the event for $\Upsilon(4S) \rightarrow B\bar{B}$ events (histogram) and continuum $e^+e^- \rightarrow q\bar{q}$ events (dots).

Signal yields and sample purities are extracted from fits to the m_{ES} distributions of B candidates with a Gaussian distribution for the signal and an ARGUS background shape³⁶ for the combinatorial background with a functional form given by

$$A(m_{\text{ES}}; m_0, \xi) = A_B m_{\text{ES}} \sqrt{1 - x_{\text{ES}}^2} e^{\xi} (1 - x_{\text{ES}}^2), \quad (24)$$

for $x_{\text{ES}} = m_{\text{ES}}/m_0 < 1$, where m_0 represents the kinematic upper limit and is held fixed at the center-of-mass beam energy $E_b^* = 5.291 \text{ GeV}$, and ξ and A_B are free parameters.

4.3.1 B^0 decays to flavor-eigenstates

Candidates in the B_{flav} sample of neutral flavor-eigenstate B mesons are formed by combining a D^{*-} or D^- with a π^+ , ρ^+ ($\rho^+ \rightarrow \pi^+\pi^0$), a_1^+ ($a_1^+ \rightarrow \pi^+\pi^-\pi^+$), or by combining a J/ψ candidate with a K^{*0} ($K^{*0} \rightarrow K^+\pi^-$). Together these modes represent a combined B^0 branching fraction of about 4.1%. Kaon identification is sometimes used to reject background, usually with a requirement for consistency rather than active identification. For most B^0 modes, it is possible to achieve signal purities of at least 90%, with the exception of such higher multiplicity channels such as $B^0 \rightarrow D^- a_1^+$. Additional background rejection is achieved with restrictions on $\cos \theta_{\text{th}}$, where needed.

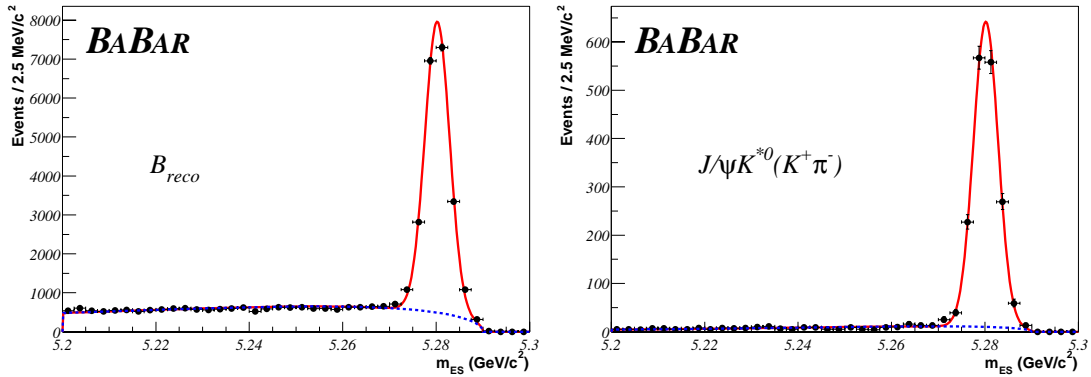


Fig. 41. Distribution of m_{ES} for all selected flavor-eigenstate B^0 candidates in hadronic decays to (a) open charm and (b) charmonium final states. Overlaid in both cases is the result of a fit with a Gaussian distribution for the signal and an ARGUS function for the background.

Based on the 81.3 fb^{-1} *BABAR* data sample, the net B^0 signal sample consists of 23618 candidates with $m_{\text{ES}} > 5.27 \text{ GeV}/c^2$ in open charm decays with a purity of about

84%, and 1757 in the decay $B^0 \rightarrow J/\psi K^{*0}$ ($K^{*0} \rightarrow K^+\pi^-$), with a purity of about 96%, both after tagging and vertexing requirements. Figure 41 shows the combined m_{ES} distribution for all the hadronic B^0 modes. Superimposed is the result of a fit with a Gaussian distribution for the signal and an ARGUS background form.³⁶

The signal obtained by this method includes a small fraction of peaking background from other charged and neutral B decay modes. However, only the charged B component needs to be determined, since it alone has a time structure that differs from the signal events. Therefore, the fraction of peaking background can be estimated with a sample of $\Upsilon(4S) \rightarrow B^+B^-$ Monte Carlo events.

4.3.2 B^+ control samples

An additional B^+ control sample of charged B candidates can be formed by combining a \bar{D}^{*0} , \bar{D}^0 , J/ψ , or $\psi(2S)$ candidate with a π^+ or K^+ , together representing a combined B^+ branching fraction of about 1.35%. Based on the 81.3 fb^{-1} BABAR data sample, the net B^+ signal sample in open charm modes, after applying any decay-vertex requirements, consists of 6245 candidates with $m_{ES} > 5.27 \text{ GeV}/c^2$ in charmonium modes, with a purity of about 94%, and 15915 candidates in open charm modes, with a purity of about 87%. Figure 42 shows the combined m_{ES} distribution for all the hadronic B^+ modes. Superimposed on the data is the result of a fit with a Gaussian distribution for the signal and an ARGUS background form.³⁶

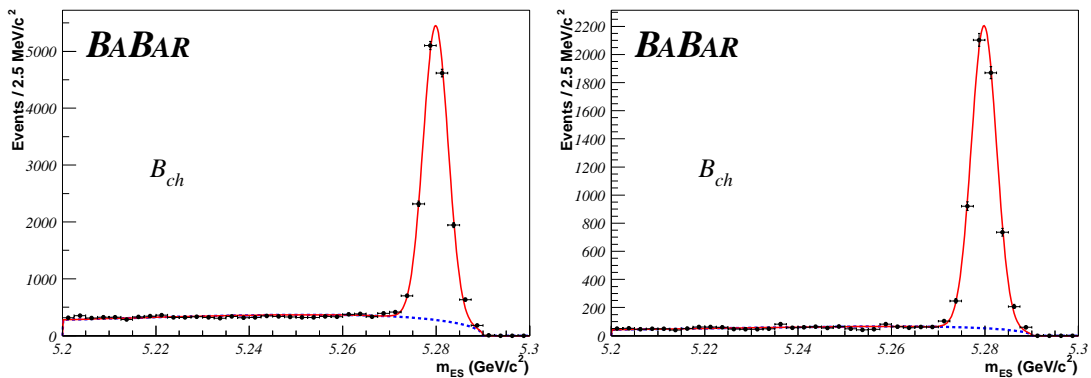


Fig. 42. Distribution of m_{ES} for all selected flavor-eigenstate B^+ candidates in hadronic decays to (a) open charm and (b) charmonium final states. Overlaid in both cases is the result of a fit with a Gaussian distribution for the signal and an ARGUS function for the background.

4.3.3 B^0 decays to CP modes involving K_S^0

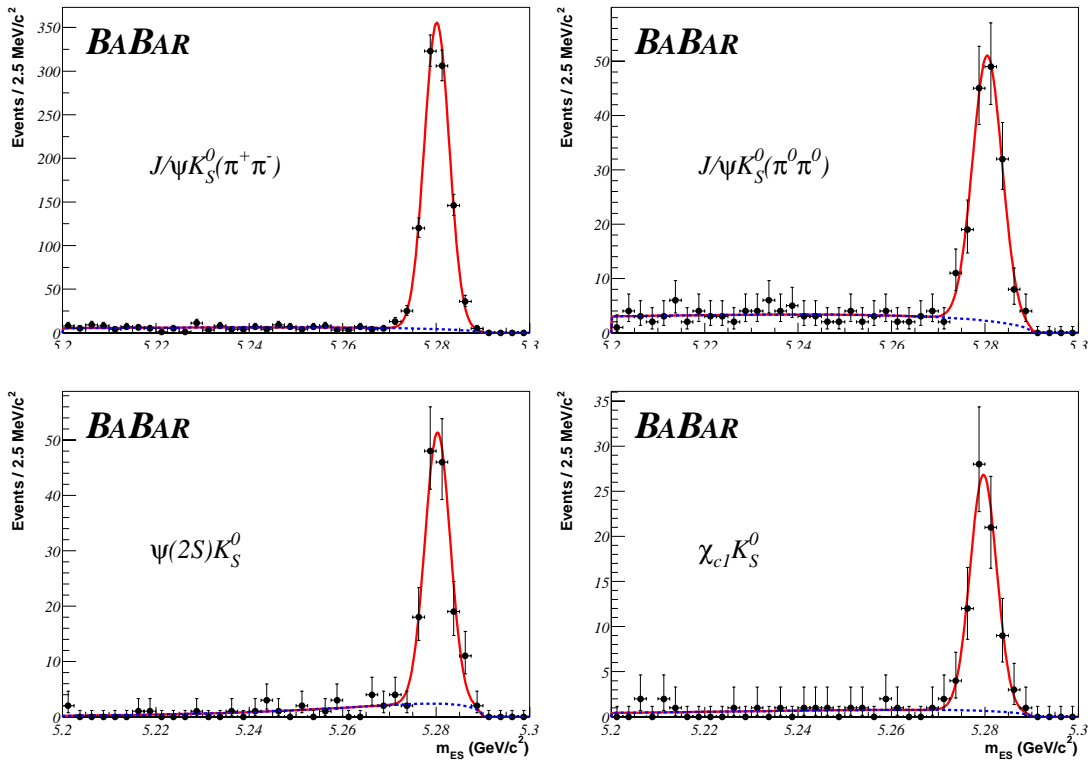


Fig. 43. Candidates for $B^0 \rightarrow J/\psi K_S^0$ where K_S^0 decays to a) $\pi^+\pi^-$ or b) $\pi^0\pi^0$; Candidates for c) $B^0 \rightarrow \psi(2S)K_S^0$ and d) $B^0 \rightarrow \chi_{c1}K_S^0$ ($K_S^0 \rightarrow \pi^+\pi^-$). Overlaid in each case is the result of a fit with a Gaussian distribution for the signal and an ARGUS function for the background.

A sample B_{CP} of neutral B candidates in charmonium modes with a K_S^0 by combining mass-constrained J/ψ , $\psi(2S)$, χ_{c1} or η_c candidates with mass-constrained K_S^0 candidates. The helicity angle θ_h of the J/ψ daughters with respect to the J/ψ flight direction in the B candidate rest frame should have a $\sin^2 \theta_h$ distribution. This can be exploited by restricting $|\cos \theta_h|$ as an efficient way of rejecting backgrounds.

Distributions of m_{ES} are shown in Figure 43 for the CP samples. Candidate yields and purities, determined from a fit to the m_{ES} distributions after selection on ΔE , are summarized in Table 6 for the 81.3 fb^{-1} BABAR data sample. A comparable sample is available from the 78 fb^{-1} Belle data sample as shown in Table 7.

Table 6. Candidate yields for the different samples used in *BABAR* time-dependent *CP* asymmetry measurements with the 81.3 fb^{-1} data sample, after tagging and vertexing requirements. Note that the *BABAR* tagging strategy has an efficiency of about 65.6%, but comparable $Q = \epsilon(1 - 2w)^2$ to Belle. The purity for *B* decays to hadronic final states are obtained from a fit to the m_{ES} distribution described in Section 4.3, after selection on ΔE . Purities are quoted for $m_{\text{ES}} > 5.27 \text{ MeV}/c^2$. The results for $J/\psi K_L^0$ are obtained from a fit to the ΔE distribution described in Section 4.4. The purity for $J/\psi K_L^0$ is quoted for events with $\Delta E < 10 \text{ MeV}$.

Sample	Final state	Candidates	Purity (%)
B_{CP}	$J/\psi K_S^0 (K_S^0 \rightarrow \pi^+ \pi^-)$	974	97
	$J/\psi K_S^0 (K_S^0 \rightarrow \pi^0 \pi^0)$	170	89
	$\psi(2S) K_S^0$	150	97
	$\chi_{c1} K_S^0$	80	95
	$\eta_c K_S^0$	132	73
	$J/\psi K^{*0} (K^{*0} \rightarrow K_S^0 \pi^0)$	147	81
	$J/\psi K_L^0$	988	55
	Total	2641	78
B_{flav}	Open charm	23618	84
	Charmonium	1757	96
	Total	25375	85
B^+	Open charm	15915	87
	Charmonium	6245	94
	Total	22160	89

4.4 B^0 decays to the *CP* mode $J/\psi K_L^0$

Candidates for the B_{CP} sample in the mode $B^0 \rightarrow J/\psi K_L^0$ are obtained by combining mass-constrained J/ψ and K_L^0 candidates. Since the K_L^0 energy is not well measured by the calorimeter (EMC at *BABAR* or ECL at Belle) or in the flux-return detectors (IFR at *BABAR* or KLM at Belle), the laboratory momentum of the K_L^0 is determined by its flight direction as measured from the calorimeter or flux-return cluster and one of two equivalent constraints derived from knowledge of the initial *B* state. For *BABAR*, the B^0 mass

Table 7. Candidate yields for the different samples used in Belle time-dependent CP asymmetry measurements with the 78 fb^{-1} data sample, after tagging and vertexing requirements. Note that the Belle tagging strategy has an efficiency of about 100%, but comparable $Q = \epsilon(1 - 2w)^2$ to $BABAR$. The purity for B decays to hadronic final states are obtained from a fit to the m_{ES} distribution described in Section 4.3, after selection on ΔE . Purities are quoted for $m_{\text{ES}} > 5.27 \text{ MeV}/c^2$. The results for $J/\psi K_L^0$ are obtained from a fit to the p_B^* distribution described in Section 4.4.

Sample	Final state	Candidates	Purity (%)
B_{CP}	$J/\psi K_S^0 (K_S^0 \rightarrow \pi^+\pi^-)$	1116	97
	$J/\psi K_S^0 (K_S^0 \rightarrow \pi^0\pi^0)$	162	82
	$\psi(2S)K_S^0$	172	93
	$\chi_{c1}K_S^0$	67	95
	$\eta_c K_S^0$	122	71
	$J/\psi K^{*0} (K^{*0} \rightarrow K_S^0\pi^0)$	89	92
	$J/\psi K_L^0$	1230	63
	Total		2958

constraint is applied to the $J/\psi K_L^0$ system. This leaves the difference ΔE between the energy of the $J/\psi K_L^0$ system and the beam energy in the $\Upsilon(4S)$ frame available to discriminate between signal and backgrounds. For Belle, the condition $\Delta E = 0$ is applied instead and the B candidate cms momentum p_B^* is used to determine the signal content of the sample. The production angle θ_B of a B meson with respect to the z axis in the $\Upsilon(4S)$ frame follows a $\sin^2 \theta_B$ distribution and so can be used to remove background. The J/ψ helicity angle is required to satisfy $|\cos \theta_h| < 0.9$ and the sum of $|\cos \theta_B|$ and $|\cos \theta_h|$ must be less than 1.3. Events with a reconstructed charged or neutral B decay to channels such as $J/\psi K_S^0 (K_S^0 \rightarrow \pi^+\pi^- \text{ or } \pi^0\pi^0)$, $J/\psi K^{*0} (K^{*0} \rightarrow K^+\pi^- \text{ or } K_S^0\pi^0)$, $J/\psi K^+$, or $J/\psi K^{*+} (K^{*+} \rightarrow K_S^0\pi^+ \text{ or } K^+\pi^0)$ are explicitly removed, since these can easily contribute fake signal events. Finally, the K_L^0 direction predicted for a correct reconstruction of $B^0 \rightarrow J/\psi K_L^0$ should coincide with the measured direction, either by restrictions on the opening angle between the two vectors or on the missing transverse momentum perpendicular to the measured flight direction.

The ΔE distribution of selected $B^0 \rightarrow J/\psi K_L^0$ combinations in the 81.3 fb^{-1}

BABAR data sample is shown in Figure 44. Signal events are peaked within ± 10 MeV of $\Delta E = 0$ while background events extend towards positive values of ΔE . The small signal width and the asymmetric distribution of the background in comparison with the K_S^0 modes are both consequences of the mass constraint used to determine the K_L^0 momentum. The corresponding distribution of cms B candidate momentum p_B^* in the 78 fb^{-1} Belle data sample is shown in Figure 45.

The purity of the $B^0 \rightarrow J/\psi K_L^0$ sample is the lowest of the CP modes ($\sim 60\%$). In particular, there are irreducible backgrounds, predominantly from $B \rightarrow J/\psi K_L^0 X$ modes, which cannot be distinguished from signal due to imposition of the m_B mass or $\Delta E = 0$ constraint in determining the momentum of the K_L^0 candidate. The largest single background contribution is from $B \rightarrow J/\psi K^*$, where the K^* decays to $K_L^0 \pi$. This mode and backgrounds from other $B \rightarrow J/\psi X$ decays are studied with Monte Carlo simulation. Background from events with a misreconstructed $J/\psi \rightarrow \ell\ell$ candidate is studied in data with the $m(\ell\ell)$ sidebands. A binned likelihood fit to the ΔE distribution is performed to determine the composition of the $B^0 \rightarrow J/\psi K_L^0$ sample. The result of the fit is shown in Figure 44.

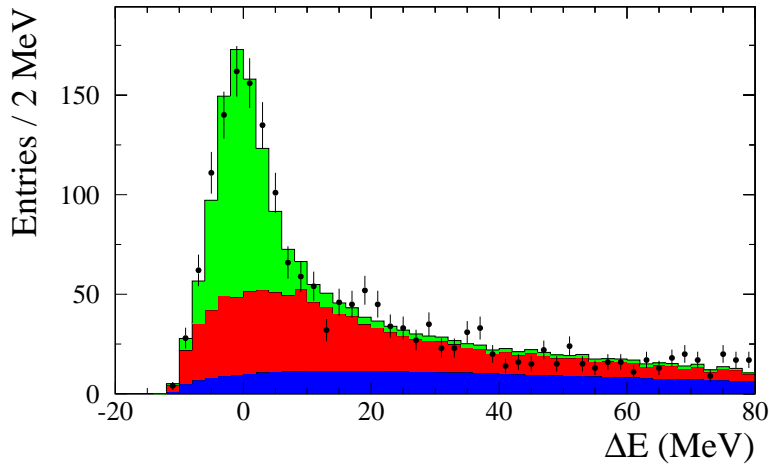


Fig. 44. Distribution of ΔE for selected $B^0 \rightarrow J/\psi K_L^0$ combinations in the 81.3 fb^{-1} BABAR sample. The points with error bars are the data. The open histogram is the result of a binned likelihood fit with signal (open), inclusive J/ψ background (cross hatched), and non- J/ψ combinatorial background (dark shading). Candidates for the B_{CP} sample are selected in the region $|\Delta E| < 10$ MeV.

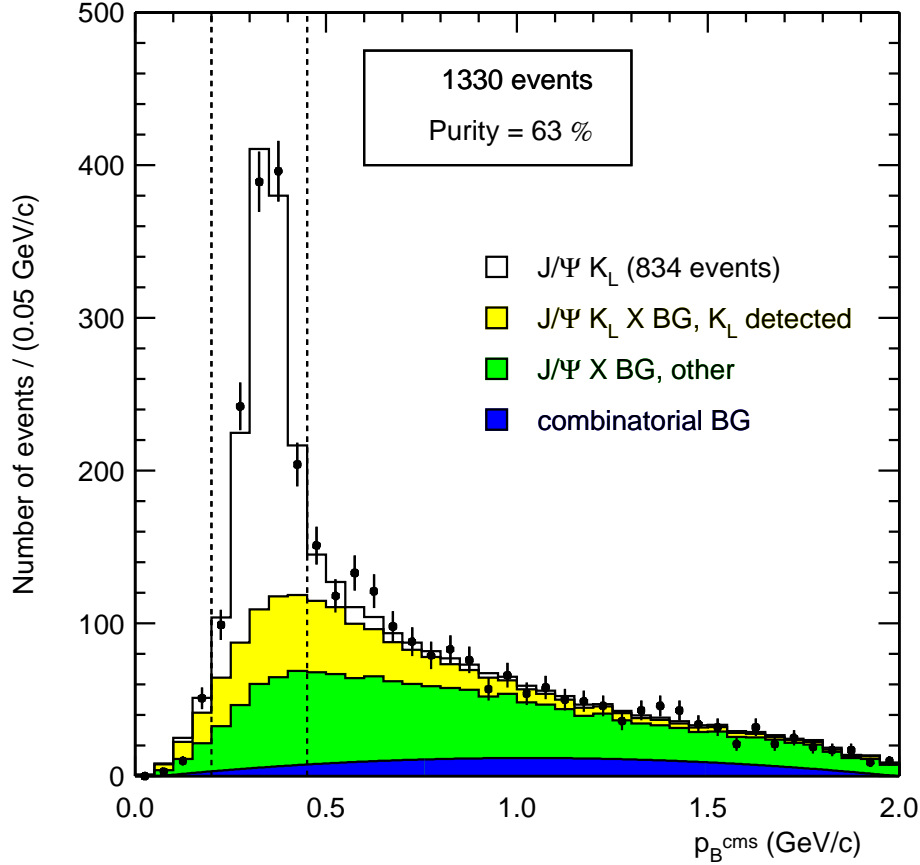


Fig. 45. Distribution of B candidate cms momentum p_B^* for selected $J/\psi K_L^0$ combinations in the 78 fb^{-1} Belle sample. The points with error bars are the data. The open histogram is the result of a fit with signal (open), $J/\psi K_L^0 X$ background with a detected K_L^0 , inclusive J/ψ background (cross hatched), and non- J/ψ combinatorial background (dark shading). Candidates for the B_{CP} sample are selected in the region $0.20 < p_B^* < 0.45 \text{ MeV}/c$.

4.4.1 B^0 decays to the CP mode $J/\psi K^{*0}$

The B_{CP} sample can be further enlarged by the addition of B^0 candidates in the mode $J/\psi K^{*0}$ ($K^{*0} \rightarrow K_s^0 \pi^0$). For this purpose, mass-constrained J/ψ candidates are combined with $K^{*0} \rightarrow K_s^0 \pi^0$ candidates to form a B^0 candidate. This channel is susceptible

to cross-feed backgrounds from other $B \rightarrow J/\psi X$ modes involving a π^0 (which includes reflection from the CP mode itself), which can be suppressed with requirements on the cosine of the helicity angle of the K^{*0} in the B^0 meson rest frame.

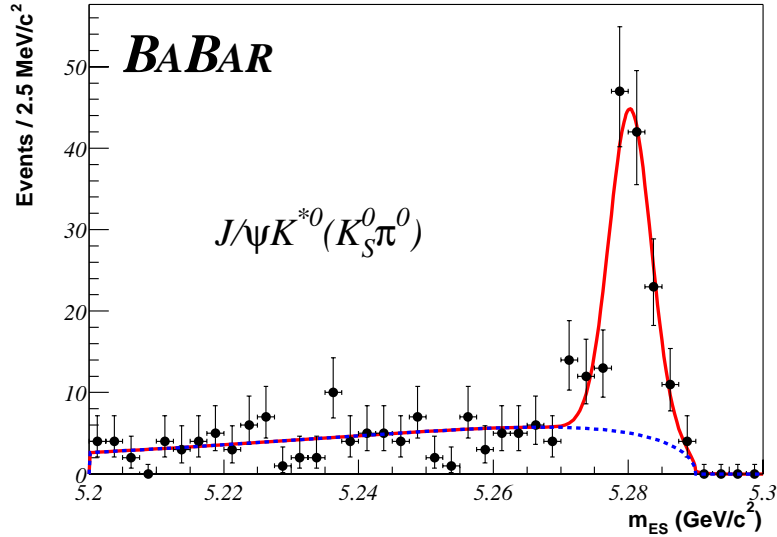


Fig. 46. Distribution in the 81.3 fb^{-1} *BABAR* data sample of m_{ES} for selected $J/\psi K^{*0}$ combinations, where $K^{*0} \rightarrow K_S^0 \pi^0$ after tagging and vertexing requirements.

The m_{ES} distribution for $J/\psi K^{*0}$ ($K^{*0} \rightarrow K_S^0 \pi^0$) combinations in data is shown in Figure 46. Given the relatively tight criteria applied in the lepton identification of the daughters of the J/ψ candidates, the background is dominated by true J/ψ mesons from B decays. As a result, backgrounds are not estimated with a fit to the observed m_{ES} distribution, but rather by extrapolation of Monte Carlo background distributions, normalized to the number of produced B mesons in the data. Signal yields and purities in data are listed in Table 6. The dominant source of cross-feed background, with zero effective CP , is $B^+ \rightarrow J/\psi K^{*+}$ ($K^{*+} \rightarrow K_S^0 \pi^+$), where the daughter π^+ is exchanged for a background π^0 .

In addition to somewhat larger backgrounds, the $J/\psi K^{*0}$ mode has the additional complication of not being a pure CP eigenstate. The orbital angular momentum carried by the $J/\psi K^{*0}$ system can be used to determine the contribution of $\eta_{CP} = +1$ ($L = 0, 2$) and $\eta_{CP} = -1$ ($L = 1$). When the angular information in the decay is ignored, the measured CP asymmetry in $J/\psi K^{*0}$ is reduced by a dilution factor $D_{\perp} = 1 - 2R_{\perp}$, where R_{\perp} is the fraction of the $L = 1$ component. This has been measured at *BABAR*

to be $R_{\perp} = 0.160 \pm 0.032 \pm 0.014$ ²¹ which, after acceptance corrections, leads to an effective $\eta_{CP} = +0.65 \pm 0.07$ for the $J/\psi K^{*0}$ mode. A similar determination at Belle finds a consistent value of $R_{\perp} = 0.191 \pm 0.023 \pm 0.026$.²²

5 Time difference measurement

The difference between B decay times, $\Delta t = t_{\text{rec}} - t_{\text{tag}}$, is determined from the measured separation Δz between the vertex of the reconstructed B meson (B_{rec}) and the vertex of the daughters of the flavor-tagging B meson (B_{tag}) along the z axis. The Δz resolution is dominated by the z position resolution for the B_{tag} vertex.

5.1 Δz reconstruction

We will follow the algorithms used at *BABAR* with the understanding that the approach at Belle is similar. Reconstruction of the B_{rec} vertex is based on a straightforward use of all charged daughter tracks to a best fit spatial point of origin. Daughter tracks from K_S^0 and D candidates are first fit to a separate vertex and the resulting parent momentum and position are used in the fit to the B_{rec} vertex. The RMS resolution in z for the B_{rec} vertex in Monte Carlo simulation is about $65 \mu\text{m}$ for more than 99% of the B candidates, and $40 \mu\text{m}$ for about 80% of the candidates.

The vertex for the B_{tag} decay is constructed from all tracks in the event except the daughters of B_{rec} . Since one of the two B mesons in the event is fully reconstructed, an additional constraint is available from the inferred B_{tag} production point and three-momentum, with its associated error matrix. This is determined from the knowledge of the three momentum of the fully reconstructed B_{rec} candidate, its decay vertex and error matrix, and from the knowledge of the average position of the interaction point and the $\Upsilon(4S)$ average boost (see Figure 47). These B_{tag} parameters are used as input to a geometrical fit to a single vertex, including all other tracks in the event except those used to reconstruct B_{rec} . In order to reduce bias and tails due to long-lived particles, K_S^0 and Λ^0 candidates are used as input to the fit in place of their daughters. In addition, tracks consistent with photon conversions ($\gamma \rightarrow e^+e^-$) are excluded. To reduce contributions from charm decay products, which bias the determination of the vertex position, the track with the largest vertex χ^2 contribution greater than 6 is removed and the fit is redone until no track fails the χ^2 requirement. In Monte Carlo simulation, the RMS of the core and tail Gaussian components of the residual Δz distribution (measured Δz minus

true Δz) is $190 \mu\text{m}$. The residual distribution can be fit to the sum of three Gaussian distributions, from which the RMS of the narrowest Gaussian, containing 70% of the area, is about $100 \mu\text{m}$. Only 1% of the area is in the widest Gaussian.

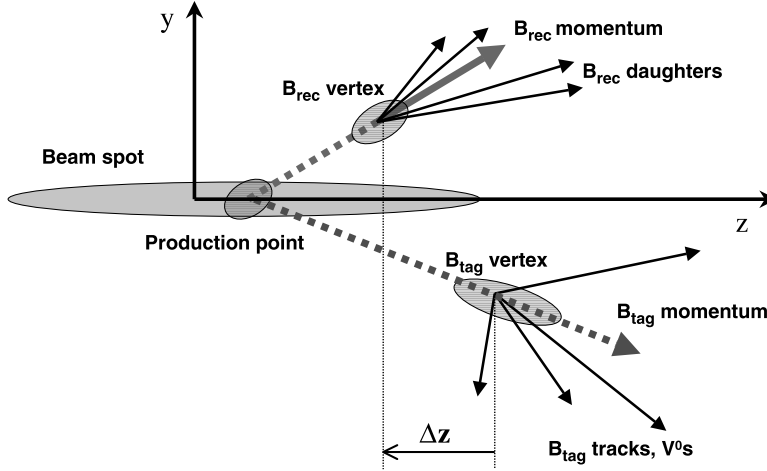


Fig. 47. Schematic view of the geometry in the yz plane for a $\Upsilon(4S) \rightarrow B\bar{B}$ decay. For fully reconstructed decay modes, the line of flight of the B_{tag} can be estimated from the (reverse) momentum vector and the vertex position of B_{rec} , and from the beam spot position in the xy plane and the $\Upsilon(4S)$ average boost. Note that the scale in the y direction is substantially magnified compared to that in the z direction.

5.2 Δt measurement

The experimental resolution on the decay length difference Δz dominates the accuracy with which Δt can be determined. The next most significant limitation is the B meson momentum of about $340 \text{ MeV}/c$ in the $\Upsilon(4S)$ rest frame. However, a partial correction for this effect can be implemented, as described below. The impact on the Δt measurement of the spread in the two beam energies, which results in a distribution of $\Upsilon(4S)$ momenta with a Gaussian width of about $6 \text{ MeV}/c$, is negligible. Finally, a correction is applied for the 20 mrad angle between the $\Upsilon(4S)$ boost direction (the z axis in the following discussion) and the axis of symmetry of the detector, along which the separation between vertices is measured.

Neglecting the B momentum in the $\Upsilon(4S)$ frame, one can write

$$\Delta z = \beta\gamma c\Delta t, \quad (25)$$

where $\beta\gamma$ is the $\Upsilon(4S)$ boost factor. The average value for the boost factor is $\beta\gamma = 0.55$.

In the case of a fully reconstructed B_{rec} , the momentum direction of the reconstructed candidate is measured with good precision and can be used to correct for the B momentum in the $\Upsilon(4S)$ frame. However, the correction depends on the sum of the decay times, $t_{\text{rec}} + t_{\text{tag}}$, which can only be determined with very poor resolution. An estimate is possible based on the relation $t_{\text{rec}} + t_{\text{tag}} = \tau_B + |\Delta t|$, which can then be used to correct for the measured B_{rec} momentum direction and extract Δt from the following expression:

$$\Delta z = \beta\gamma\gamma_{\text{rec}}^* c\Delta t + \gamma\beta_{\text{rec}}^* \gamma_{\text{rec}}^* \cos\theta_{\text{rec}}^* c(\tau_B + |\Delta t|), \quad (26)$$

where θ_{rec}^* , β_{rec}^* , and γ_{rec}^* are the polar angle with respect to the beam direction, the velocity, and the boost factor of the B_{rec} in the $\Upsilon(4S)$ frame. The difference between Δt calculated with Eq. 25 and Eq. 26 is very small because $\gamma_{\text{rec}}^* = 1.002$ and $\beta_{\text{rec}}^* = 0.064$. The event-by-event difference in Δt calculated with the two methods has an RMS of 0.20 ps. Equation 26 improves the Δt resolution by about 5%. In addition, it removes a correlation between the resolution on Δt and the true value of Δt . This correlation is due to the fact that the RMS of the second term in Eq. 26 depends on the expectation value of $(t_{\text{rec}} + t_{\text{tag}})^2$, which in turn depends on $|\Delta t|$.

5.3 Vertex quality requirements

A number of requirements are made in order to ensure a well-determined vertex separation. The fit for both the B_{rec} and B_{tag} vertex must converge. Also, the error on Δt determined from the vertex fit must be less than 2.4 ps and $|\Delta t|$ must be less than 20 ps. The efficiency for passing these requirements in data and Monte Carlo simulation is about 97% for all B_{rec} modes. The simulation, also shows that the reconstruction efficiency does not depend on the true value of Δt .

5.4 Δt resolution function

An event-by-event estimate of the error on Δt can be obtained from the measurement errors on the extrapolated tracks that are included in the B_{rec} and B_{tag} vertices. Figure 48a shows the distribution of the error on Δz so obtained from a sample of B decays to open charm. While the peak of the error distribution is about 90 μm , there is a long tail extending beyond 200 μm . Monte Carlo simulation can be used to study how well

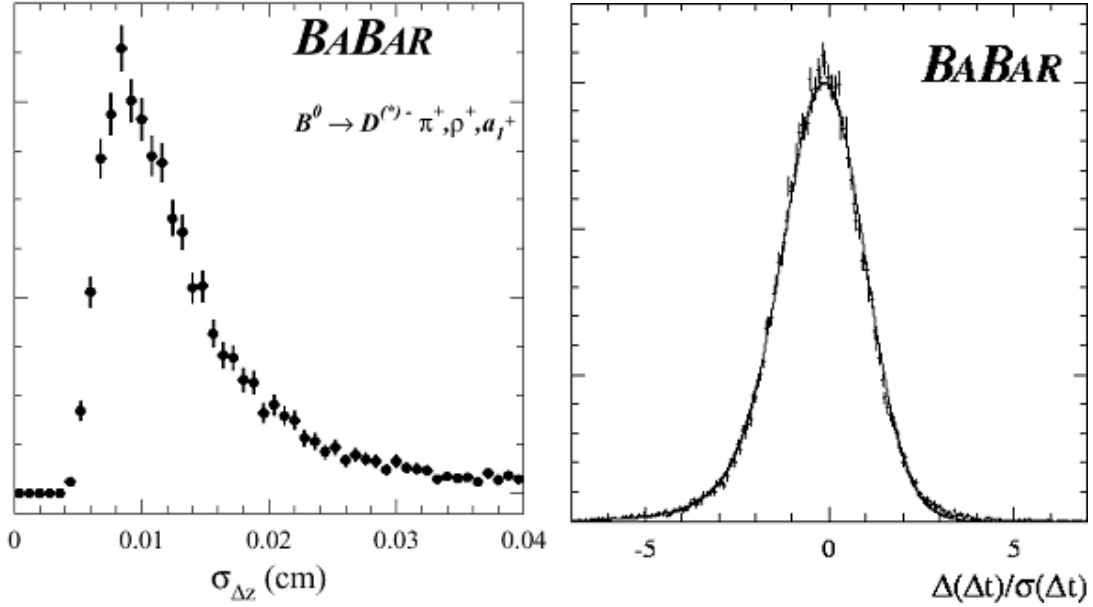


Fig. 48. Distribution of the event-by-event errors on the measurement of Δz as observed in the B_{flav} sample (left); distribution from Monte Carlo simulation of the difference between measured and true Δt divided by the measurement error $\sigma(\Delta t)$ (right).

the event-by-event calculated error reproduces the actual uncertainties on Δt . As can be seen in Figure 48b, the distribution of $\delta t = \Delta t_{\text{meas}} - \Delta t_{\text{true}}$ divided by the calculated error $\sigma(\Delta t)$ is very nearly Gaussian. The deviations from unit width and the slight bias towards negative Δt that are evident in the distribution are accommodated by scaling the calculated errors with a Δt resolution function.

The Δt resolution function is represented in terms of δ_t by one of two possible empirical parameterizations. One is known as a ‘‘Gaussian-Exponential’’ distribution

$$\begin{aligned} \mathcal{R}_{GE}(\delta_t, \sigma_{\Delta t} | \hat{a} = \{f, S, \kappa\}) &= f \frac{1}{\sqrt{2\pi} S \sigma_{\Delta t}} \exp\left(-\frac{\delta_t^2}{2S^2 \sigma_{\Delta t}^2}\right) \\ &+ (1-f) \int_{-\infty}^0 \frac{1}{\kappa \sigma_{\Delta t}} \exp\left(\frac{\delta'_t}{\kappa \sigma_{\Delta t}}\right) \frac{1}{\sqrt{2\pi} S \sigma_{\Delta t}} \exp\left(-\frac{(\delta_t - \delta'_t)^2}{2S^2 \sigma_{\Delta t}^2}\right) d(\delta'_t). \end{aligned} \quad (27)$$

The other, known as a ‘‘Triple-Gaussian’’ is obtained from the sum of three Gaussian distributions (called the core, tail and outlier components) with different means and

widths:

$$\mathcal{R}_{3G}(\delta_t; \hat{a}) = \sum_{k=1}^2 \frac{f_k}{S_k \sigma_{\Delta t} \sqrt{2\pi}} \exp\left(-\frac{(\delta_t - b_k \sigma_{\Delta t})^2}{2(S_k \sigma_{\Delta t})^2}\right) + \frac{f_3}{\sigma_3 \sqrt{2\pi}} \exp\left(-\frac{\delta_t^2}{2\sigma_3^2}\right). \quad (28)$$

In both resolution models, the measurement error $\sigma_{\Delta t}$ derived from the vertex fit for each event is used, allowing for a separate scale factor (S for GE, or S_1 and S_2 for 3G) to accommodate any overall underestimate ($S_k > 1$) or overestimate ($S_k < 1$) of the errors for all events.

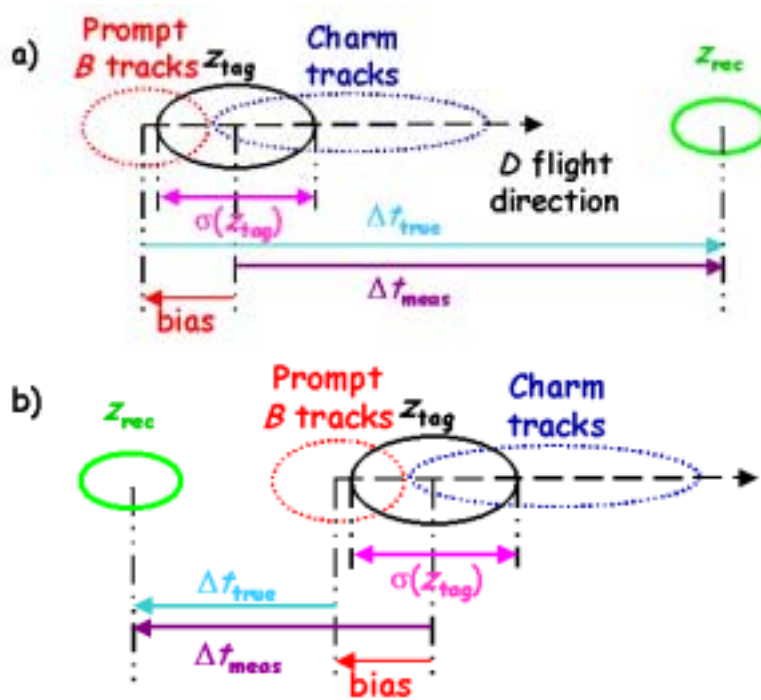


Fig. 49. Illustration of vertex difference bias introduced by inclusion of charm tracks in the B vertex: (a) for $\Delta t > 0$ and (b) for $\Delta t < 0$.

Both forms attempt to accommodate the impact of the finite charm flight distances and the inclusion of residual charm decay products on the B_{tag} vertex determination. In GE case, an explicit component with an effective lifetime $\kappa \sigma_{\Delta t}$ is incorporated in the resolution function. In the 3G model, the core and tail Gaussian distributions are allowed to have a nonzero mean. Figure 49 shows the basic vertex topology. Recalling that charm flight distances are typically a few hundred microns, it is clear that it is

not possible to cleanly differentiate tracks from the secondary charm decay from those produced directly from the B parent, particularly given that many tracks are well below $1 \text{ GeV}/c$ momentum and have relatively poor impact parameter resolution. The consequence of including daughter tracks from the charm decay in the vertex fit is to add a small bias to the B_{tag} vertex determination. When the B_{tag} decay occurs first, $\Delta t > 0$ and the bias is negative, pulling the B_{tag} vertex towards the B_{rec} vertex and reducing Δt . When the B_{tag} decay occurs second, $\Delta t < 0$ and $|\Delta t|$ is increased by the charm component, so again the bias is negative. Including a provision for this effect in the resolution function minimizes the eventual bias in measured parameters, particularly lifetimes and mixing rates.

In the 3G resolution function, these mean offsets are incorporated as scale factors b_k times the event-by-event measurement error $\sigma_{\Delta t}$ to account for an observed correlation shown in Figure 50b between the mean of the δ_t distribution and the measurement error $\sigma_{\Delta t}$ in Monte Carlo simulation. Figure 51 illustrates the underlying origin of this correlation. In B decays, the vertex error ellipse for the D decay products is oriented with its major axis along the D flight direction, leading to a correlation between the D flight direction and the calculated uncertainty on the vertex position in z for the B_{tag} candidate. In addition, the flight length of the D in the z direction is correlated with its flight direction. Therefore, the bias in the measured B_{tag} position due to inclusion of D decay products is correlated with the D flight direction. Taking into account these two correlations, it is clear that D mesons with a flight direction perpendicular to the z axis in the laboratory frame will have the best z resolution and will introduce the least bias in a measurement of the z position of the B_{tag} vertex, while D mesons that travel forward in the laboratory will have poorer z resolution and will introduce a larger bias in the measurement of the B_{tag} vertex.

Monte Carlo simulations confirm the expectation that the resolution function is less biased for events with a primary lepton tag than those with a kaon tag. Therefore, the mean of the core Gaussian is allowed to be different for each tagging category. One common mean is used for the tail component. The third Gaussian has a fixed width of 8 ps and no offset; it accounts for the fewer than 1% of events with incorrectly reconstructed vertices.

Since the B_{tag} vertex precision dominates the Δt resolution, no significant differences between the Δt resolution function for the flavor-eigenstate sample and the CP -eigenstate sample are expected. Hence, identical resolution functions are used for all modes. This assumption is supported by Monte Carlo simulation and addressed

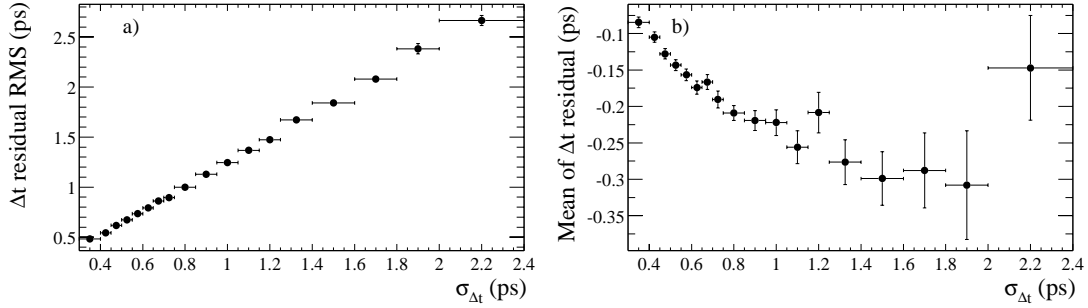


Fig. 50. Correlation between the event-by-event error on Δt ($\sigma_{\Delta t}$) and a) the observed RMS and b) offset of the mean for $\delta_t = \Delta t - \Delta t_{\text{true}}$ from Monte Carlo simulation.

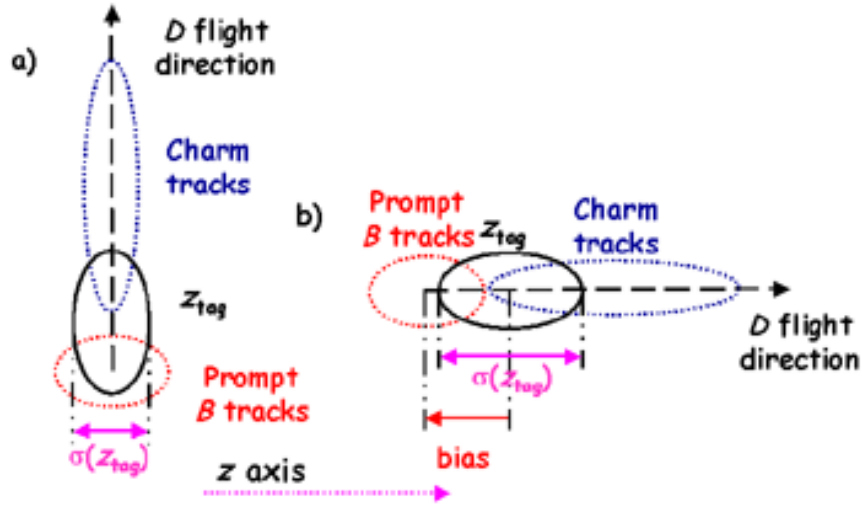


Fig. 51. Illustration of the expected correlation between the error on Δt and the size of the bias on Δt , depending on whether the charm decay is (a) perpendicular or (b) parallel to the boost direction (z axis).

in the evaluation of systematic errors. Figure 52 shows the distribution of the uncertainties on $\sigma_{\Delta t}$ from the fit to Δz for the flavor-eigenstate sample, and the combined $\eta_{CP} = -1$ ($J/\psi K_S^0$, $\psi(2S)K_S^0$, $\chi_{c1}K_S^0$) and $J/\psi K^{*0}$ samples. Also shown is a comparison between data and Monte Carlo prediction for the two samples, since Monte Carlo simulation is used to evaluate the systematic error contribution. The flavor-eigenstate and CP -eigenstate distributions need not be the same under our assumption of a common resolution function, since the topologies and multiplicities of the B_{rec} decays are different. The agreement between the data and Monte Carlo simulation is satisfactory,

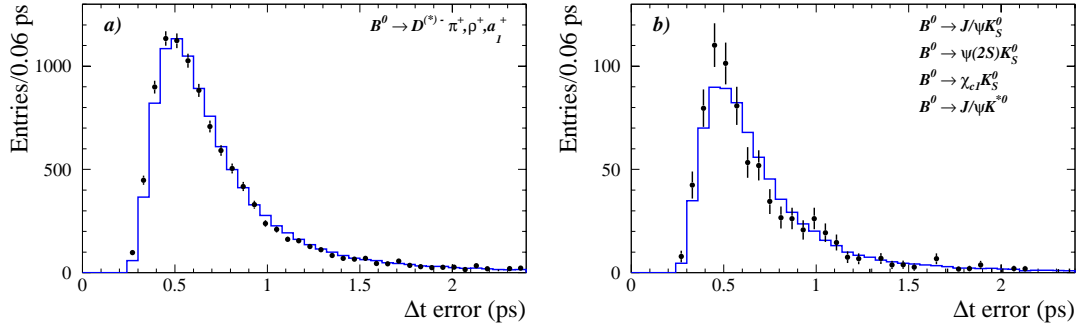


Fig. 52. Distribution of event-by-event uncertainties on Δt ($\sigma_{\Delta t}$) for a) the sample of neutral B decays to flavor eigenstates other than $J/\psi K^{*0}(K^+ \pi^-)$ and b) the combined $\eta_{CP} = -1$ ($J/\psi K_S^0$, $\psi(2S)K_S^0$, $\chi_{c1}K_S^0$) and $J/\psi K^{*0}$ samples. The histogram corresponds to Monte Carlo simulation and the points with error bars to data. All distributions have been background-subtracted with events from the m_{ES} sideband. The Monte Carlo distribution has been normalized to the same area as the data distribution.

particularly given the statistical uncertainties for the CP sample.

5.5 Validation of vertex assumptions

Two of the fundamental assumptions in this analysis are that the Δt resolution function for the sample of flavor-eigenstate modes is the same as that for CP events, and that the event-by-event vertex errors provide a good measure of the relative uncertainty on the Δz measurement from event to event. In Figure 53, various properties of the flavor-eigenstate sample are compared with the combined $\eta_{CP} = -1$ and $J/\psi K^{*0}$ samples. These include the χ^2 probability for the vertex fits, the number of tracks used in the B_{tag} vertex, and the momentum in the $\Upsilon(4S)$ rest frame and polar angle in the laboratory frame of tracks used in the B_{tag} vertex. Good agreement in all variables is observed between the two data samples.

A similar comparison of the momentum and polar-angle distribution of tracks in data and Monte Carlo simulation also shows good agreement. However, there are modest discrepancies for the χ^2 probability for the vertex fits and the number of tracks used in the B_{tag} vertex. The agreement improves when residual misalignments between the SVT silicon modules in the Monte Carlo simulation are included.

As expected, there are no significant differences observed in comparisons between

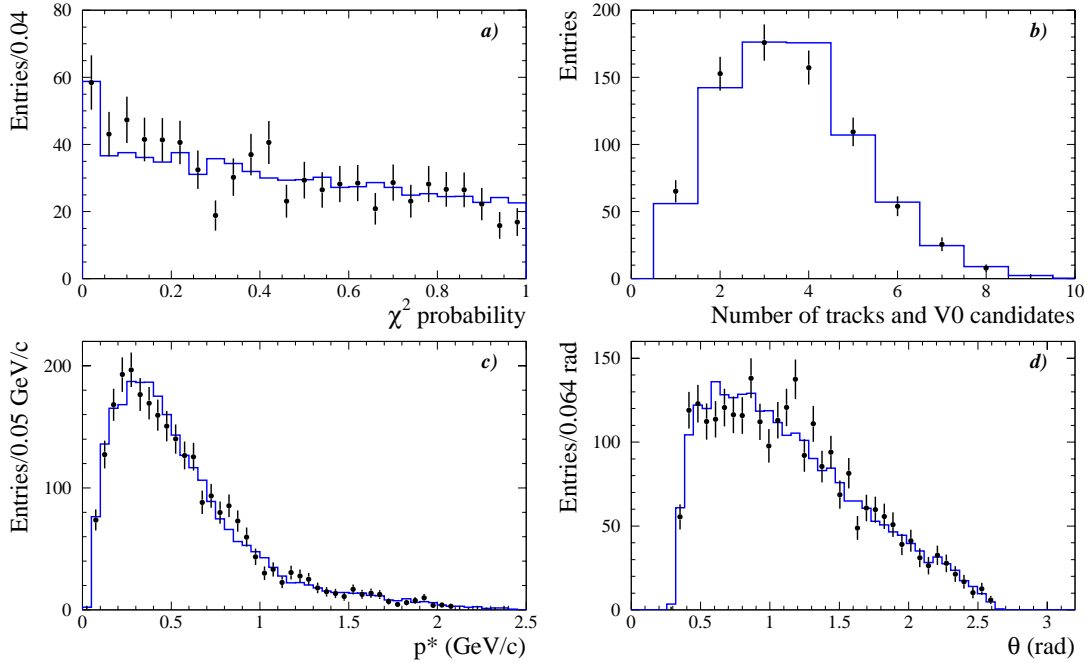


Fig. 53. Distributions of a) χ^2 probability of the B_{tag} vertex fit, b) number of charged tracks and V^0 candidates used in the B_{tag} vertex, c) momentum in the center-of-mass frame, and d) polar angle in the laboratory frame for tracks in the B_{tag} vertex, for the flavor-eigenstate (histograms) and the combined $\eta_{CP} = -1$ and $J/\psi K^{*0}$ (points with errors bars) data samples. All distributions have been background-subtracted with events from the m_{ES} sideband. The flavor-eigenstate distributions have been normalized to the same area as the distributions from the combined $\eta_{CP} = -1$ and $J/\psi K^{*0}$ samples.

the CP modes used in the $\sin 2\beta$ analysis. However, comparisons between the CP and flavor-eigenstate samples, in data as well as in the Monte Carlo simulation, show that the CP events have a slightly better Δz resolution. For example, in Monte Carlo simulation the most probable value for $\sigma_{\Delta t}$ is about 0.017 ps (3%) worse for the B_{flav} sample, as can be seen by comparing the distributions in Figures 52a and b. This is due to the fact that the B_{CP} vertex is better determined because tracks in the lower-multiplicity CP final states generally have higher momentum. This effect is incorporated in the likelihood fit by using the calculated event-by-event errors, as described in Section 5.4. Indeed, for Monte Carlo simulation, the pull distributions for $\sigma_{\Delta t}$ (defined as the difference between the fitted and generated value divided by the calculated error) are nearly Gaussian with unit width for both the B_{CP} and B_{flav} samples. Any residual effect due to

differences in the observed scale factors in data is included as a systematic uncertainty and found to be negligible.

6 Lifetimes

6.1 Results for B lifetimes from *BABAR*

At *BABAR*,²³ the value for $\tau(B^0)$, $\tau(B^+)$, the Δt resolution parameters \hat{a}_i , and the parameters for the background description are determined by simultaneously fitting the Δt distributions of B^0 and B^+ events in the flavor-eigenstate sample with $m_{\text{ES}} > 5.2 \text{ GeV}/c^2$. The selection of the B_{flav} candidates is made with the techniques described in Section 4 in a data sample equivalent to 20.7 fb^{-1} . The lifetime measurement also requires that there be a determination of Δt based on the algorithms described in Section 5. Events are required to have at least 2 tracks remaining in the B_{tag} vertex, an error on Δz smaller than $400 \mu\text{m}$, and $|\Delta z| < 3000 \mu\text{m}$ and $|\Delta t| < 18 \text{ ps}$. These additional requirements are intended to reduce systematic errors on the precision lifetime measurements. The precision achieved on Δz , $190 \mu\text{m rms}$, is dominated by the resolution on the B_{tag} vertex. A remaining bias of $-35 \mu\text{m}$ due to charm decays on the B_{tag} side is observed. For the lifetime result, more restrictive requirements $|\Delta t| < 18 \text{ ps}$ and $\sigma_{\Delta t} < 1.4 \text{ ps}$ are applied to the proper time-difference measurement. The results of a fit with a Gaussian signal distribution and an ARGUS background function³⁶ are superimposed on the m_{ES} distribution of the final sample in Figure 54. The final sample consists of $6018 \pm 70 B^0$ and $6298 \pm 63 B^+$ signal events in a $\pm 2\sigma$ ($\sigma = 2.7 \text{ MeV}/c^2$ and $2.6 \text{ MeV}/c^2$, respectively) window around the B mass above a small background ($\simeq 10\%$).

An unbinned maximum likelihood fit is used to extract lifetime results from all events with $m_{\text{ES}} > 5.2 \text{ GeV}/c^2$. This technique extracts maximum statistical precision from the data and ideally incorporates all physically important correlations between parameters in the model itself. In order to construct the likelihood function, probability density functions (PDFs) for signal and background are required that also incorporate models for Δt resolution. The probability p_i^{sig} for event i to be signal with Δt distribution \mathcal{G} , defined in Eq. 2 with the Gaussian-Exponential resolution function $\mathcal{R}(\delta_t; \hat{a}) = \mathcal{R}_{GE}$, is estimated from the m_{ES} fit (Figure 54) and the m_{ES} value of the B_{rec} candidate. Each event i then contributes to the likelihood with weighted contribu-

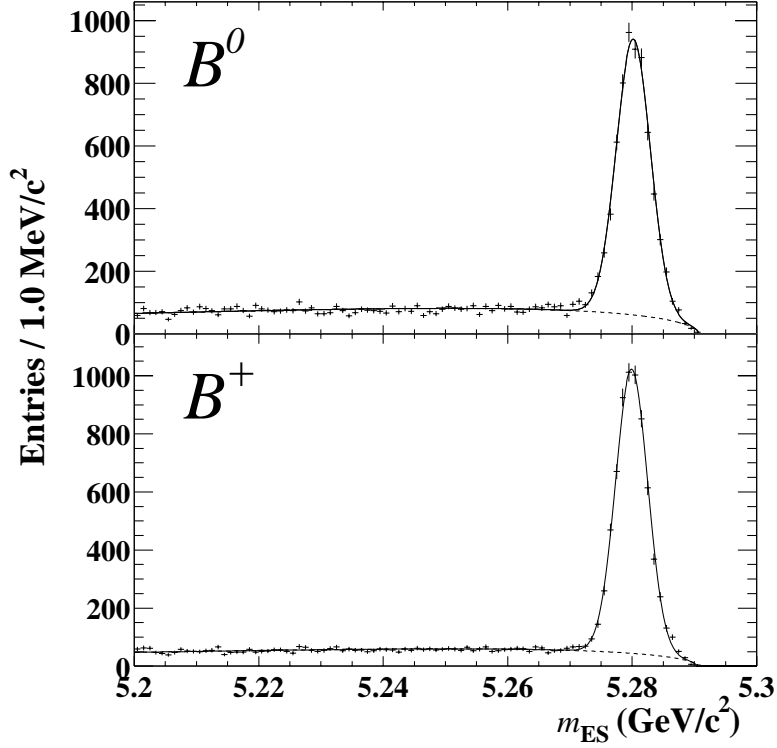


Fig. 54. Distribution of m_{ES} for selected B^0 and B^+ candidates included in the lifetime measurement. The dashed line represents the fitted combinatorial background, while the solid line includes both the background and a Gaussian signal component [BABAR].

tions of signal, background, and outlier PDF components:

$$\begin{aligned} \mathcal{F}(\Delta t_i, \sigma_i, p_i^{sig}; \tau, \hat{a}, \hat{b}, f_{out}^{sig}, f_{out}^{bkg}) = & \quad (29) \\ p_i^{sig} \cdot [(1 - f_{out}^{sig}) \cdot \mathcal{G}(\Delta t_i; \tau, \hat{a}) + f_{out}^{sig} \cdot \mathcal{O}(\Delta t_i)] + & \\ (1 - p_i^{sig}) \cdot [(1 - f_{out}^{bkg}) \cdot \mathcal{B}(\Delta t_i; \hat{b}) + f_{out}^{bkg} \cdot \mathcal{O}(\Delta t_i)]. & \end{aligned}$$

The background Δt distribution, \mathcal{B} , for each B species is modelled by the sum of a prompt component and a lifetime component convoluted with a resolution function of the form given in Eq. 27, but with a separate set of parameters \hat{b} . The fraction of non-prompt background, its effective lifetime and the background resolution parameters are determined separately for charged and neutral B mesons. Signal and background outlier events have an assumed Δt behavior \mathcal{O} given by a Gaussian distribution with zero mean and a fixed 10 ps width. The fractions of outliers in signal and background are determined separately in the lifetime fit.

Since the same resolution function is used for neutral and charged B mesons, the fitting procedure maximizes the log-likelihood function $\ln \mathcal{L}$ formed from the sum of two terms, one for each B meson species, with common parameters \hat{a} for \mathcal{R} :

$$\begin{aligned} \ln \mathcal{L} = & \sum_{i^+} \ln[\mathcal{F}(\Delta t_{i^+}, \sigma_{i^+}, p_{i^+}^{sig}; \tau_{B^+}, \hat{a}, \hat{b}_+, f_{out}^{sig,+}, f_{out}^{bkg,+})] \\ & + \sum_{i^0} \ln[\mathcal{F}(\Delta t_{i^0}, \sigma_{i^0}, p_{i^0}^{sig}; \tau_{B^0}, \hat{a}, \hat{b}_0, f_{out}^{sig,0}, f_{out}^{bkg,0})]. \end{aligned} \quad (30)$$

The likelihood fit involves 19 free parameters. The parameter τ_{B^+} is replaced with $\tau_{B^+} = r \cdot \tau_{B^0}$ to estimate the statistical error on the lifetime ratio r . The lifetime values were kept hidden until the event selection, Δt reconstruction method, and fitting procedures were finalized and the systematic errors were determined.

The fit results, after small corrections due to the assumption of common B^+ and B^0 signal resolution function, are summarized in Table 9. The resolution parameters \hat{a} ($h = 0.69 \pm 0.07$, $s = 1.21 \pm 0.07$ and $\kappa = 1.04 \pm 0.24$) are consistent with those found in a Monte Carlo simulation that includes detector alignment effects. The fitted outlier fractions in the B^+ and B^0 signals are both $0.2_{-0.2}^{+0.3}\%$. Figure 55 shows the results of the fit superimposed on the observed Δt distributions for B^0 and B^+ events within 2.5 standard deviations of the B mass in m_{ES} .

Table 8. Summary of the systematic uncertainties on the B lifetime measurements.

Effect	$\delta(\tau_{B^0})$ (ps)	$\delta(\tau_{B^+})$ (ps)	$\delta(\tau_{B^+}/\tau_{B^0})$
MC statistics	0.009	0.007	0.006
\mathcal{R} parameterization	0.008	0.004	0.003
same \mathcal{R} for B^0 and B^+	0.004	0.005	0.006
Beam spot, $p_{B_{rec}}$	0.002	0.002	Cancels
Δt outliers	0.011	0.011	0.005
SVT alignment	0.008	0.008	Cancels
z scale	0.008	0.008	Cancels
Δz to Δt conversion	0.006	0.006	Cancels
Signal probability	0.003	0.003	0.003
Background modelling	0.005	0.011	0.005
Total in quadrature	0.022	0.023	0.012

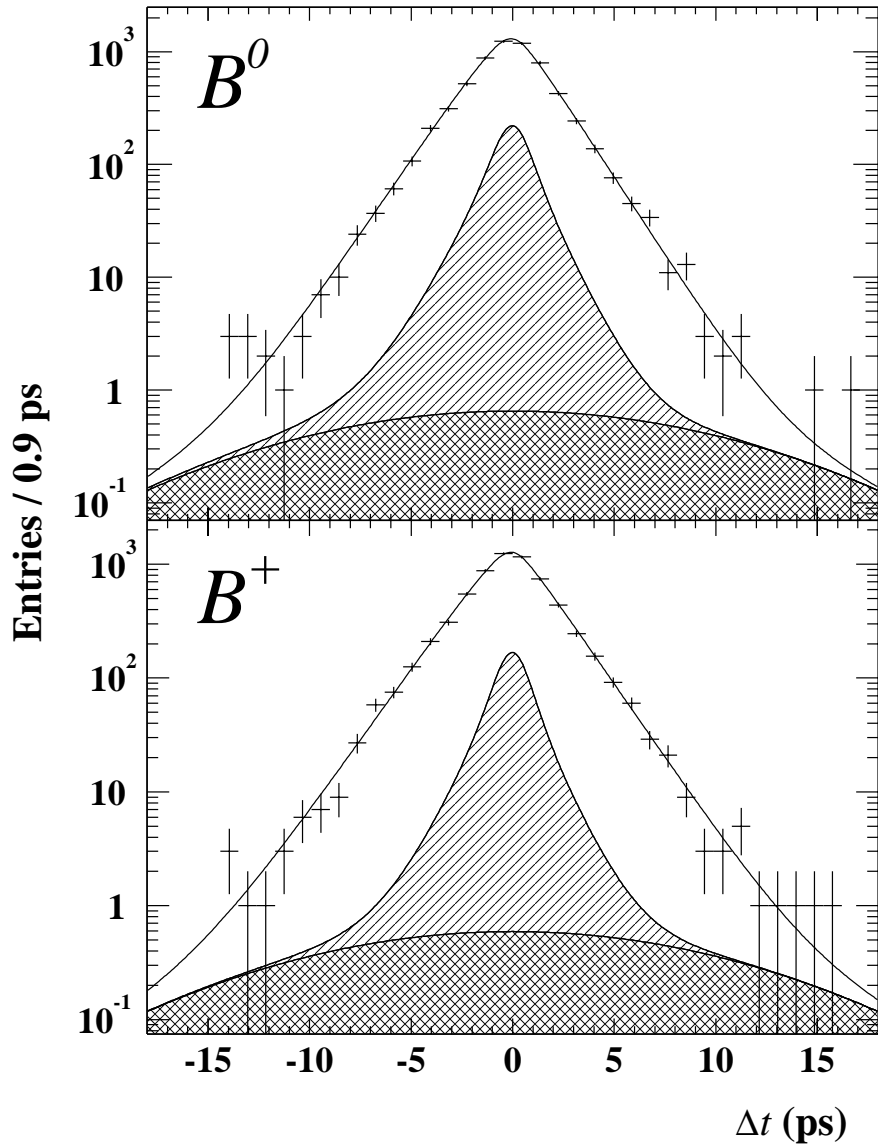


Fig. 55. Distribution of proper time difference Δt between the reconstructed B_{rec} and tag-side B_{tag} decays for neutral (top) and charged (bottom) B candidates that lie within 2σ of the B mass in m_{ES} . The results of the likelihood fit are superimposed. The single-hatched areas are the background components and the cross-hatched areas represent the outlier contributions [BABAR].

Table 8 summarizes the systematic uncertainties on the lifetime results. The full analysis chain, including event reconstruction and selection, has been tested with Monte Carlo simulation with no significant bias observed. The statistical precision of this test is assigned as a systematic error. The resolution parameters \hat{a} , determined from the data as part of the fit, contribute ± 0.017 ps in quadrature to the statistical error of the individual lifetime results. Thus, a large part of the Δt resolution uncertainty is included in the statistical error. Residual systematic uncertainties are attributed to limited flexibility of the resolution model, which are estimated by comparing results with different parameterizations. A small systematic error results from uncertainties on the beam spot position and vertical size, and the B_{rec} momentum vector, which are used to constrain the B_{tag} vertex. An ensemble of Monte Carlo experiments is used to explore the sensitivity to the outlier component. Additional systematic uncertainties are due to the residual misalignments in the SVT. The z length scale is only verified to the 0.5% level from secondary interactions in a beam pipe section of known length and this leads to a small systematic error. Approximations already noted in Section 5.2 in the calculation of Δt from Δz and the uncertainty on the boost leads to small systematic errors. The errors on the m_{ES} fit parameters are used to determine the uncertainty on p^{sig} and the corresponding systematic error. The main background uncertainty is due to changes in the background composition as a function of m_{ES} . An additional contribution arises from a 1-2% B^0 contamination of the B^+ signal sample and vice versa. Monte Carlo simulation is used to correct for these background effects and the sum in quadrature of the corrections is assigned as a systematic uncertainty.

6.2 Results for B lifetimes from Belle

A similar analysis has been conducted by Belle,²⁴ where the value for $\tau(B^0)$, $\tau(B^+)$, the signal Δt resolution parameters \hat{a}_i , and outlier parameters description are determined by simultaneously fitting the Δt distributions of B^0 and B^+ events in the flavor-eigenstate sample in a signal region defined by $m_{\text{ES}} = m_B$ and $|\Delta E| = 0$ to within 3σ . A description of the resolution and time-distribution of the background in this sample is obtained by separate fits to events in the m_{ES} sidebands. Events in the lifetime sample are assigned signal and background probabilities based on a two-dimensional fit to the full $m_{\text{ES}}-\Delta E$ distribution, with an ARGUS function to model the background in m_{ES} and a first-order polynomial in ΔE . The selection of the B_{flav} candidates is made with the techniques described in Section 4 in a data sample equivalent to 29.1 fb^{-1} . The

lifetime measurement also requires that there be a determination of Δt based on the algorithms similar to those described in Section 5. The final sample consists of 7863 B^0 and 12047 B^+ candidates in the signal region.

Table 9. Summary of B Factory lifetime measurements.

	<i>BABAR</i> ²³ [20.6 fb ⁻¹]	Belle ²⁴ [29.1 fb ⁻¹]	PDG2000 ¹⁸
τ_{B^0} [ps]	$1.546 \pm 0.032 \pm 0.022$	$1.554 \pm 0.030 \pm 0.019$	1.548 ± 0.032
τ_{B^+} [ps]	$1.673 \pm 0.032 \pm 0.023$	$1.695 \pm 0.026 \pm 0.015$	1.653 ± 0.028
τ_{B^+}/τ_{B^0}	$1.082 \pm 0.026 \pm 0.012$	$1.091 \pm 0.023 \pm 0.014$	1.062 ± 0.029

The fit results, after small corrections due to the assumption of common B^+ and B^0 signal resolution function, are summarized in Table 9. Figure 56 shows the results of the fit superimposed on the observed Δt distributions for B^0 and B^+ events within 3 standard deviations of the B mass in m_{ES} . At 2% relative error, clearly these are precision results, comparable in fact to the world average in the PDG2000 compilation.¹⁸ They demonstrate excellent control of the Δt resolution function at both *BABAR* and Belle, as an essential component of the CP asymmetry and mixing measurements. Note that the measurements are still statistics dominated, so that further improvement can be expected based on the currently recorded data sets, which are about 4–5 times larger than used in the reported analyses.

7 Flavor tagging

After removal of the daughters of the reconstructed B , the remaining tracks can be analyzed to determine not only the vertex position z_{tag} of the B_{tag} decay, but also its flavor, allowing the ensemble to be assigned a tag flavor, either B^0 or \bar{B}^0 .

In its simplest initial form, four different types of flavor tag, or tagging categories, have been defined. The first two tagging categories rely upon the presence of a prompt lepton, or one or more charged kaons in the event. The next two categories exploit a variety of inputs with a neural-network algorithm. These tagging categories are hierarchical and mutually exclusive.

To quantify the discriminating power of each tagging category, it is useful to introduce a figure of merit the effective tagging efficiency $Q_i = \epsilon_i (1 - 2w_i)^2$, where ϵ_i is the fraction of events associated to the tagging category i and w_i is the mistag fraction, the

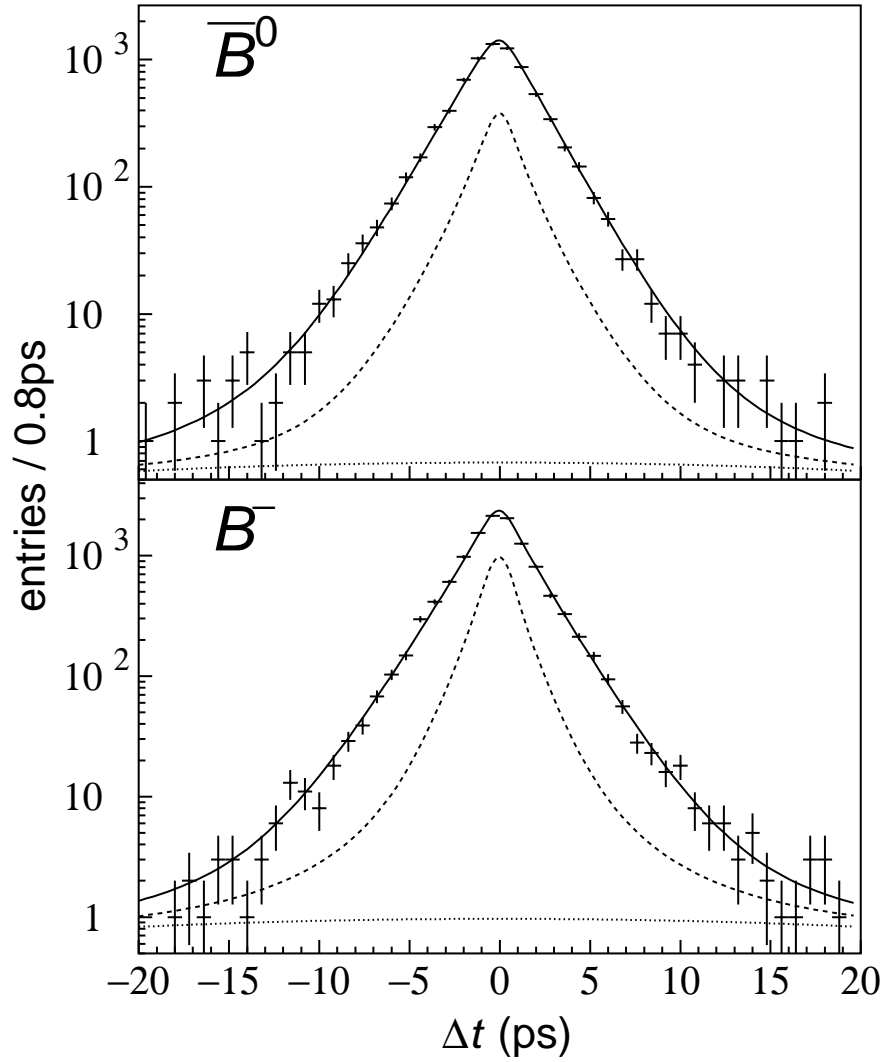


Fig. 56. Distribution of proper time difference Δt between the reconstructed B_{rec} and tag-side B_{tag} decays for neutral (top) and charged (bottom) B candidates that lie within 3σ of the B mass in m_{ES} . The results of the likelihood fit are superimposed. The dashed curves are the background components and the dotted areas represent the outlier contributions [Belle].

probability of incorrectly assigning the tag to an event in this category. The statistical errors in the measurements of $\sin 2\beta$ and Δm_d are inversely proportional to $\sqrt{\sum_i Q_i}$.

The mistag fractions, and thus the tagging performance, are measured with the B_{flav} data sample. The results are shown in Section 9.

7.1 Lepton and kaon tags

The Lepton and Kaon tagging categories use the correlation between the flavor of the decaying b quark and the charge of a primary lepton from a semileptonic decay or the charge of a kaon from the chain $b \rightarrow c \rightarrow s$.

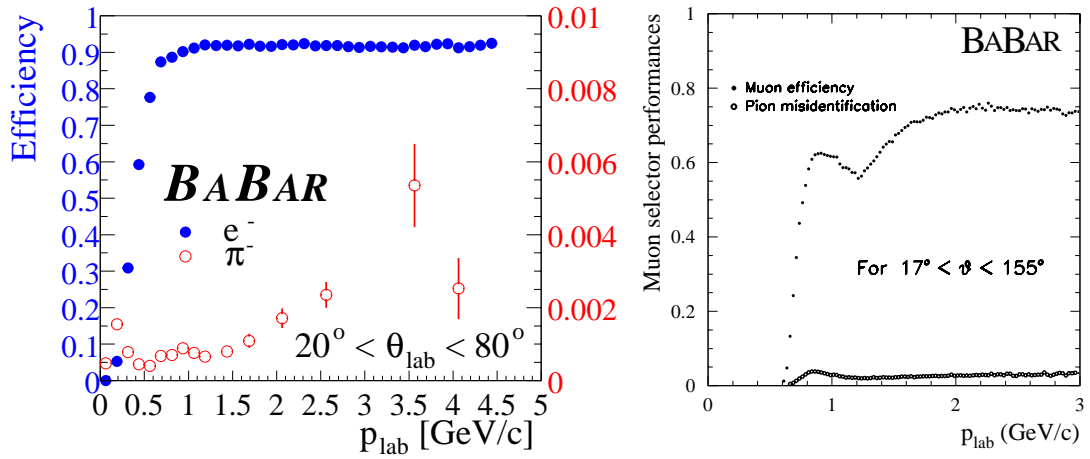


Fig. 57. Electron (left) and muon (right) identification efficiency and pion misidentification probability [BABAR].

For the Lepton category uses both electrons and muons. Although not discussed in detail here, the lepton identification efficiencies and hadron misidentification rates at BABAR and Belle are shown in Figures 57 and 58. A minimum requirement of 1.0 (1.1) GeV/ c on the electron (muon) center-of-mass momentum is applied to reduce the contamination from softer, opposite-sign leptons coming from cascade semileptonic decays of charm mesons. The center-of-mass momentum distributions for electrons and muons are shown in Figure 59 for the B_{flav} sample, after background subtraction based on the m_{ES} sideband events. Overlaid on the data is a Monte Carlo simulation of the spectrum.

The kaon content of the event is evaluated by taking the sum of the charges of all kaons identified with a neural network algorithm (\mathcal{K} subnet described below in Sec-

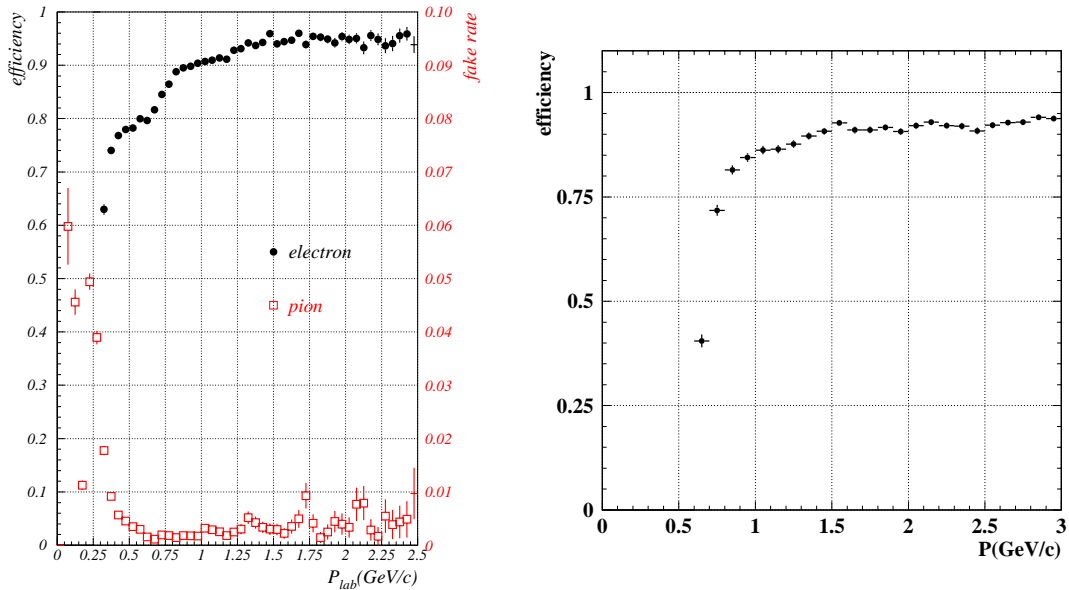


Fig. 58. Electron (left) and muon (right) identification efficiency and pion misidentification probability [Belle].

tion 7.2). The kaon identification algorithm has been set to maximize the effective tagging efficiency Q . There are 0.8 charged kaons per B decay, and roughly 15% of these have the wrong sign (e.g. K^- from B^0 , rather than the expected K^+). Wrong-sign kaons occur primarily in B decays to a charmed–anti-charmed pair of mesons. The momentum distributions are quite similar for right- and wrong-sign kaons, so that no kinematic quantity usefully distinguishes between them. The center-of-mass momentum spectrum for charged kaons and the distribution of charged kaon multiplicity are shown in Figure 60 for the B_{flav} sample.

An event with an identified high-momentum lepton is assigned to the `Lepton` category unless the sum of the charges of any kaons present has the opposite sign. Failing this, events are assigned to the `Kaon` category if the sum of the kaon charges is non-zero. The charge of the lepton or sum of kaon charges is used to assign the flavor of the B_{tag} . All remaining events, approximately 55% of the total including those with inconsistent lepton and kaon charge (0.5% of all events in simulation) and those with two oppositely-charged kaons (4.6% of all events in simulation), are passed to the neural-network-based categories.

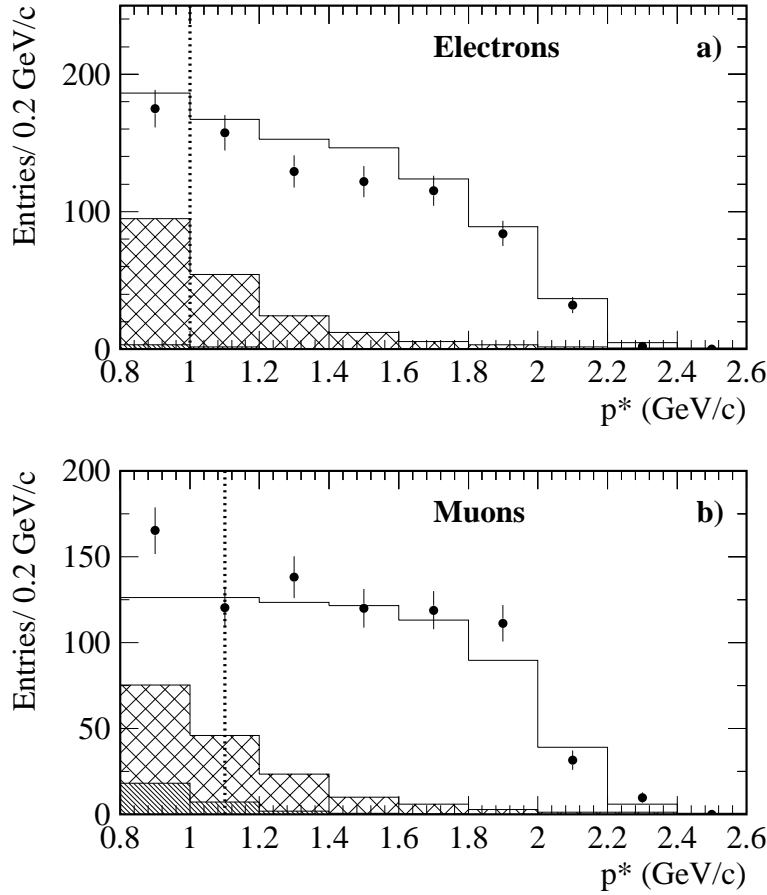


Fig. 59. Center-of-mass momentum distribution for a) electrons and b) muons. Data from the B_{flav} sample, after background subtraction based on the m_{ES} sideband, are shown as points. The open histogram shows primary leptons, the cross-hatched histogram cascade leptons, and the diagonally-hatched histogram fake leptons, all from simulation. The simulation is normalized, with a residual overall systematic error of 5%, to the total number of B^0 decays in data after background subtraction, not to the number of observed leptons. The vertical lines at 1.0 GeV/c for electrons and 1.1 GeV/c for muons indicate the requirement on center-of-mass momentum for the Lepton category.

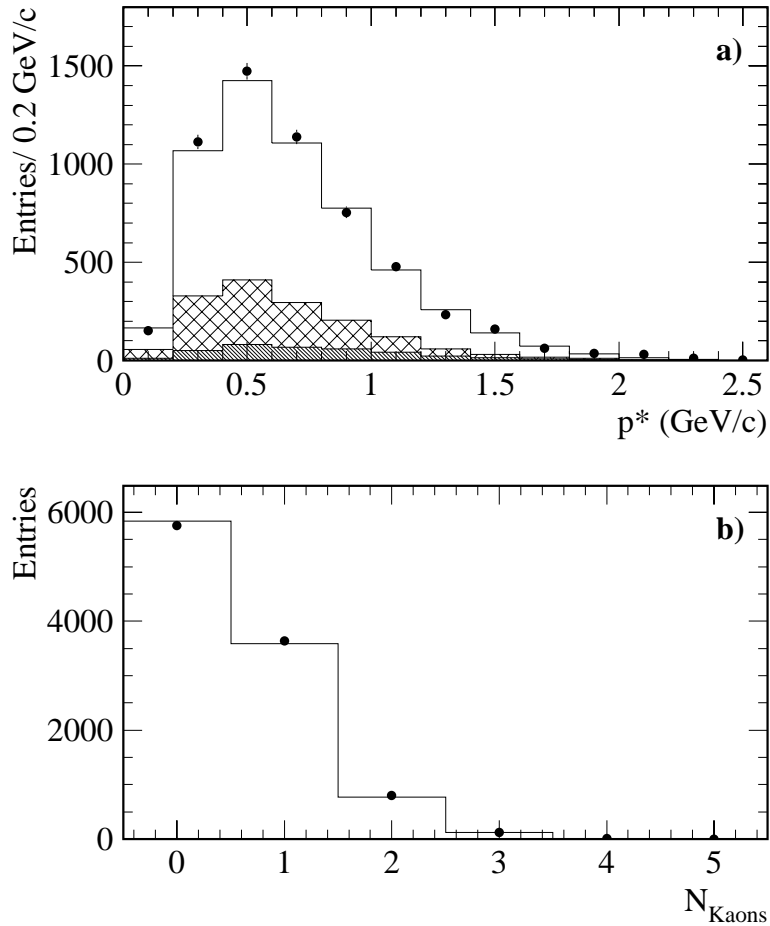


Fig. 60. a) Center-of-mass momentum distribution for kaons and b) kaon multiplicity per event. Data from the B_{flav} sample, after background subtraction based on the m_{ES} sideband, are shown as points. The histograms are from simulation. In a), the diagonally-hatched histogram is from fake kaons, the cross-hatched histogram is from kaons that have the wrong-sign charge, and the open histogram is from kaons with the right-sign charge, all from simulation. The simulation is normalized to the total number of B^0 flavor candidates after background subtraction, not to the number of observed kaons.

7.2 Neural-network tags

Besides identified high-momentum leptons and charged kaons, there are other characteristic features of B decays that can be used to determine the flavor of the B_{tag} , although not as easily or cleanly distinguishing. These include soft pions from D^* decays, high-momentum primary leptons that are not selected by the electron or muon identification algorithms, lower-momentum primary leptons, and charged kaons that are not selected by the kaon identification algorithm. These sources are harder to identify and require more kinematic quantities to discriminate against backgrounds. As a result multivariate methods are more appropriate; one implementation employs a sequence of neural networks to flavor-tag those events not assigned to the `Lepton` or `Kaon` categories.

Three different track-based neural networks, called “subnets”, are trained, each with a specific goal. The `L`, `K`, and `SoftPi` subnets are sensitive to the presence of primary leptons, charged kaons and soft pions from D^* decays, respectively. Each subnet is applied to all tracks from the B_{tag} .

The `L` subnet uses the binary output of the electron and muon identification algorithms on the input track, the center-of-mass momentum of the input track, and a pair of kinematic variables, E_W^{90} and $\cos \theta_{l\nu}$, that separate primary leptons from cascade leptons and other tracks.

The isolation variable, E_W^{90} , is given by the sum of the energies of all tracks within 90° of the W direction. The W momentum is inferred from the sum of the input track momentum and the neutrino momentum, where the latter is taken to be the missing momentum in the center-of-mass frame using all charged tracks in the B_{tag} . This variable is effective because in a semileptonic decay the hadrons recoiling against the virtual W would generally go off in the opposite direction.

The other kinematic variable used, $\cos \theta_{l\nu}$, is the cosine of the angle between the input track and the neutrino direction. The distributions in the B_{flav} sample and simulation of E_W^{90} and $\cos \theta_{l\nu}$ are shown in Figure 61a and b, for all events not in the `Lepton` or `Kaon` category.

The `K` subnet uses the input track momentum in the laboratory frame, together with the three relative likelihoods $\mathcal{L}_K/(\mathcal{L}_\pi + \mathcal{L}_K)$ for the SVT, the DCH and the DIRC. The SVT and DCH likelihoods are derived from dE/dx measurements, and the DIRC likelihood is calculated from a global fit to the number of photons detected, their positions and arrival times relative to the corresponding track.

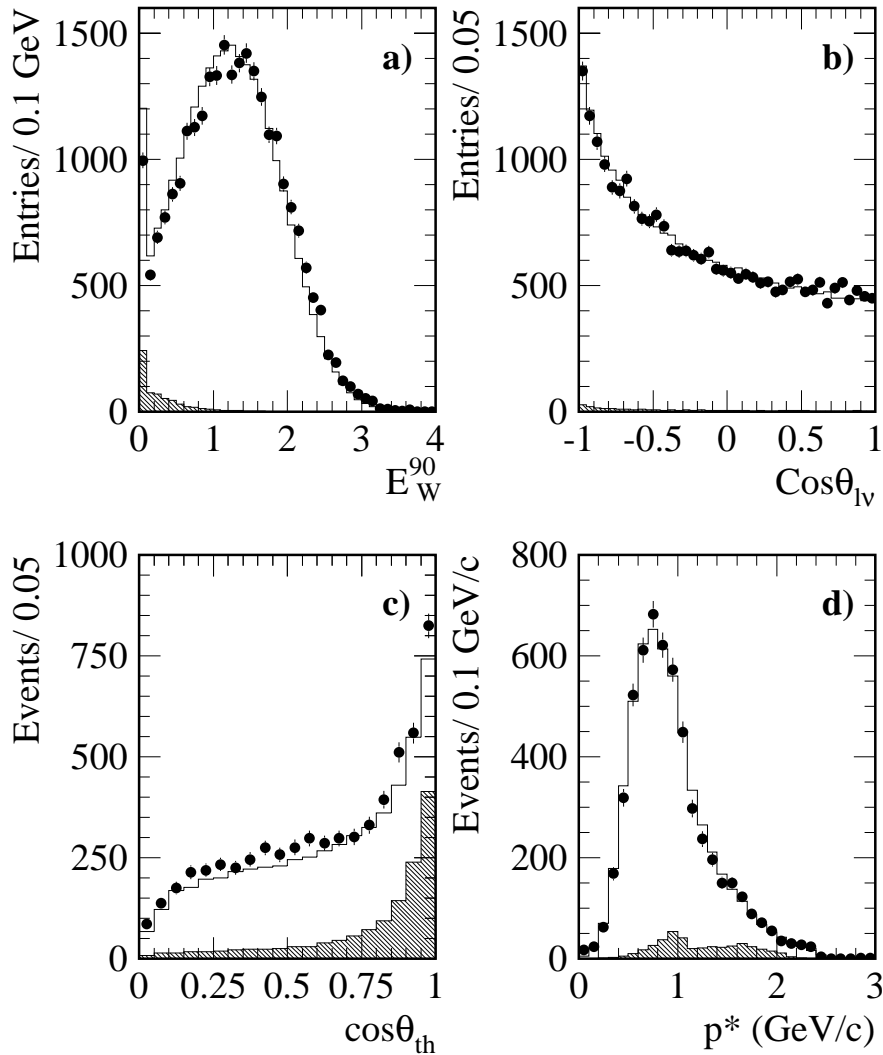


Fig. 61. Inputs to the subnets: a) E_W^{90} , b) $\text{cos}\theta_{lv}$, c) $\text{cos}\theta_{th}$ for low center-of-mass momentum tracks ($p^* < 0.18 \text{ GeV}/c$), and d) the center-of-mass momentum for all tracks. The points are data from the B_{flav} sample after background subtraction based on the m_{ES} sideband, and the histogram is simulation. For $\text{cos}\theta_{th}$ the diagonally-hatched histogram shows the contribution from soft- π coming from D^* decays, and for the other distributions shows the component from primary leptons. The simulation is normalized to the total number of B^0 flavor candidates after the background subtraction.

The `SoftPi` subnet uses the center-of-mass momentum of the input track, the cosine of the angle of the input track with the thrust axis $\cos \theta_{\text{th}}$, and the center-of-mass momentum of the minimum momentum track. The thrust axis is determined from all charged tracks and neutral clusters in the B_{tag} . The direction of any D^* in the decay of the B_{tag} is approximated by the direction of the thrust axis. Thus soft pions from D^* decays, which are aligned with the D^* direction in the center-of-mass frame, tend to be correlated with the thrust axis. The distribution of $\cos \theta_{\text{th}}$ is shown for low center-of-mass momentum tracks in Figure 61c, comparing the B_{flav} sample with simulation for all events not in the `Lepton` or `Kaon` category.

The outputs of the three subnets are among the inputs to a final neural network, which is trained to distinguish between B^0 and \bar{B}^0 . The variables used as inputs to the final network include the maximal values of the `L` and `SoftPi` subnet outputs, each multiplied by the charge of the corresponding input track, and the highest and the second-highest values of the `K` subnet output again multiplied by the charge of the corresponding input tracks. The two other inputs to the final neural network are the center-of-mass momentum of the maximum momentum track multiplied by its charge, and the number of tracks with significant impact parameters. The latter is an indicator of the presence of K_S^0 mesons. The distribution of the center-of-mass momentum for all tracks is shown in Figure 61d.

The output from the final neural network, x_{NT} , is mapped onto the interval $[-1, 1]$ shown in Figure 62a. The assigned flavor tag is B^0 if x_{NT} is negative, and \bar{B}^0 otherwise. Events with $|x_{NT}| > 0.5$ are assigned to the NT1 tagging category and events with $0.2 < |x_{NT}| < 0.5$ to the NT2 tagging category. Events with $|x_{NT}| < 0.2$, approximately 30% of the total, have very little tagging power and are rejected.

Most of the separation between B^0 and \bar{B}^0 in the NT1 and NT2 tagging categories derives from primary leptons that are not identified as electrons or muons and from soft pions from D^* decays. Simulation studies indicate that roughly 37% of the effective tagging efficiency Q is due to events with unidentified primary leptons, 28% is due to events with a soft pion, a further 11% from events with a lower momentum primary lepton, and the remainder from a mixture of the various inputs. A breakdown of the physics processes that contribute to the neural network tag is shown in Figure 62b.

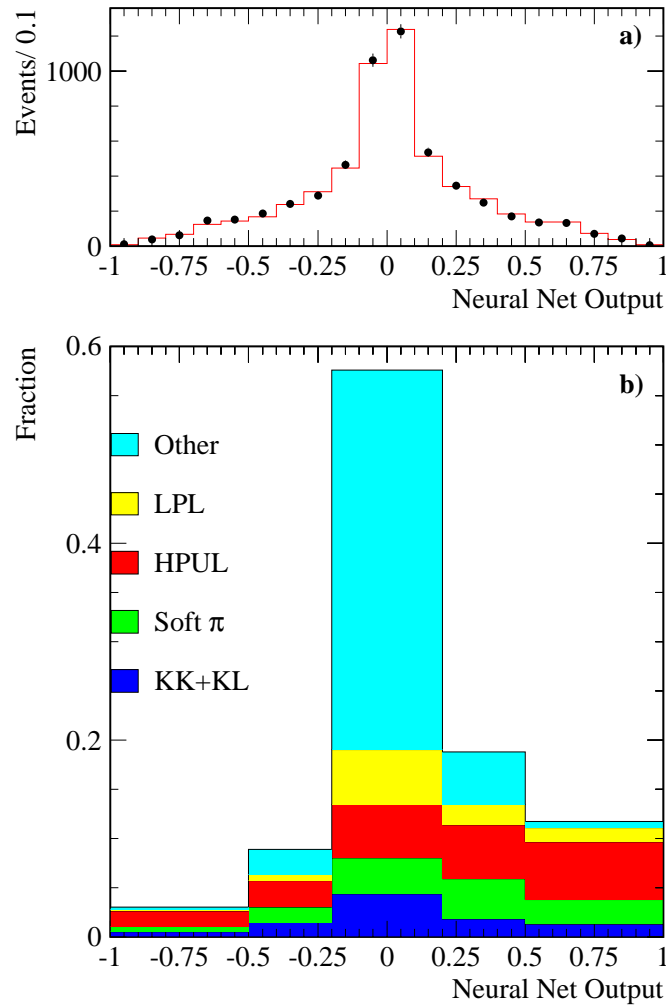


Fig. 62. a) Output of the final neural network for B_{flav} events that are not assigned to the Lepton or Kaon category, where the points are from the B_{flav} data after a background subtraction and the histogram is simulation; b) Neural network output from simulation of single B^0 decays with no time evolution, again for events not in the Lepton or Kaon category. The breakdown from bottom to top is events with two kaons or a kaon and lepton (KK+KL), events with a soft pion (soft π), events with a high momentum unidentified lepton (HPUL), events with a lower momentum lepton (LPL), and all remaining events. The outermost bins correspond to the category NT1 and the next to NT2. Entries for $x_{NT} > 0.0$ represent correct tags, while those for $x_{NT} < 0$ are mistags in each of the categories. The center bin contains events for which no tag is assigned.

8 Likelihood fit method

The value of $\sin 2\beta$ is extracted from the tagged B_{CP} sample with an unbinned maximum-likelihood technique based on $\ln \mathcal{L}_{CP}$ and the probability density functions \mathcal{F}_{\pm} of Eq. 12. However, the dilutions \mathcal{D}_i and Δz resolution parameters \hat{a}_i are also needed for the measurement. Assuming that mistag rates and vertex resolutions do not depend on the particular channel used to reconstruct the B meson, these parameters are best determined with the much larger mixing sample, since they also appear in \mathcal{L}_{mix} . In order to properly incorporate the correlations between these parameters and $\sin 2\beta$, the fit is performed by simultaneously maximizing the sum

$$\ln \mathcal{L}_{CP} + \ln \mathcal{L}_{\text{mix}} \quad (31)$$

for the combined tagged B_{flav} and B_{CP} samples. The values of B^0 lifetime and Δm_d are kept fixed in extracting $\sin 2\beta$.

The value of Δm_d is obtained with an unbinned maximum-likelihood fit to the tagged B_{flav} sample alone, where the log-likelihood $\ln \mathcal{L}_{\text{mix}}$ is maximized while keeping the B^0 lifetime fixed.

8.1 Mistag asymmetries

The probabilities of mistagging a B^0 or \bar{B}^0 meson are expected to be very nearly, but not exactly, equal. For example, the response of the detector to positive pions and kaons differs from its response to negative pions and kaons due to differences in total and charge-exchange cross sections. To account for any possible mistag differences, separate mistag probabilities w for B^0 and \bar{w} for \bar{B}^0 were introduced, with the conventions

$$\begin{aligned} \langle w \rangle &= \frac{1}{2}(w + \bar{w}); & \Delta w &= (w - \bar{w}) \\ \mathcal{D} &= 1 - 2w; & \bar{\mathcal{D}} &= 1 - 2\bar{w} \\ \langle \mathcal{D} \rangle &= \frac{1}{2}(\mathcal{D} + \bar{\mathcal{D}}); & \Delta \mathcal{D} &= (\mathcal{D} - \bar{\mathcal{D}}) \end{aligned} \quad (32)$$

The time distributions for the mixing and CP samples will thus depend on whether the tag was identified as a B^0 or a \bar{B}^0 , resulting in modifications to the expressions for mixing time development (Eq. 6)

$$\begin{aligned} h_{\pm, \text{tag}=B^0} &\propto \left[\left(1 + \frac{1}{2}\Delta \mathcal{D}\right) \pm \langle \mathcal{D} \rangle \cos \Delta m_d \Delta t \right] \\ h_{\pm, \text{tag}=\bar{B}^0} &\propto \left[\left(1 - \frac{1}{2}\Delta \mathcal{D}\right) \pm \langle \mathcal{D} \rangle \cos \Delta m_d \Delta t \right], \end{aligned} \quad (33)$$

where the \pm in the index refers to mixed ($-$) and unmixed ($+$) events as before, and for CP violation time development (Eq. 9)

$$f_{\pm} \propto [(1 \pm \frac{1}{2}\Delta\mathcal{D}) \mp \langle\mathcal{D}\rangle\eta_{CP} \sin 2\beta \sin \Delta m_d \Delta t], \quad (34)$$

where the \pm in the index refers to events where B_{tag} is a B^0 ($+$) and \bar{B}^0 ($-$) and $|\lambda| = 1$ has been assumed.

8.2 Background modelling

In the presence of backgrounds, the probability distribution functions \mathcal{H}_{\pm} of Eq. 7 and \mathcal{F}_{\pm} of Eq. 12 must be extended to include a term for each significant background source. The backgrounds for the flavor eigenstates and $\eta_{CP} = -1$ modes are quite small and are mostly combinatoric in nature. However, for the $B^0 \rightarrow J/\psi K_L^0$ and $B^0 \rightarrow J/\psi K^{*0}$ channels the backgrounds are substantial and originate mainly from other $B \rightarrow J/\psi X$ modes that have, to a very good approximation, the same flavor tagging and Δt resolution properties as the signal. The background properties of the flavor eigenstates, $\eta_{CP} = -1$ modes, and the non- J/ψ background in the $B^0 \rightarrow J/\psi K_L^0$ channel are determined empirically from sideband events in the data.

8.2.1 Background formulation for flavor eigenstates and $\eta_{CP} = -1$ modes

The background parameterizations are allowed to differ for each tagging category. Each event belongs to a particular tagging category i . In addition, the event is classified as either mixed ($-$) or unmixed ($+$) for a flavor-eigenstate or by whether B_{tag} was a B^0 ($+$) or a \bar{B}^0 ($-$) for a CP -eigenstate. The fraction of background events for each source and tagging category is a function of m_{ES} . The peaking and combinatorial background PDFs, $\mathcal{B}_{\pm,i,\text{peak}}$ and $\mathcal{B}_{\pm,i,j}$, provide an empirical description of the Δt distribution of the background events in the sample, including a resolution function parameterized by \hat{a}_i and \hat{b}_i , respectively.

The probability that a B^0 candidate is a signal or a background event is determined from a separate fit to the observed m_{ES} distributions of B_{flav} or B_{CP} candidates with $\eta_{CP} = -1$. The m_{ES} shape is described with a single Gaussian distribution $\mathcal{S}(m_{\text{ES}})$ for the signal and an ARGUS parameterization $\mathcal{A}(m_{\text{ES}})$ for the background (Eq. 24). The fraction δ_{peak} of the signal Gaussian distribution that is due to peaking backgrounds is determined from Monte Carlo simulation.

Backgrounds arise from many different sources. Rather than attempting to determine the various physics contributions an empirical description in the likelihood fit is used, allowing for background components with various time dependencies. For the B_{flav} sample, the background time distributions considered, each with its own effective dilution factor \mathcal{D}_i and either a common resolution function $\mathcal{R}(\delta_t; \hat{b}_i)$ or the signal resolution function $\mathcal{R}(\delta_t = \Delta t - \Delta t_{\text{true}}; \hat{a}_i)$. They are classified as prompt, non-prompt, and mixing background components, as well as a peaking contribution. For the $\eta_{CP} = -1$ sample, the possible background contributions corresponding to prompt and CP background components, as well as a peaking contribution.

The likelihood fit includes as free parameters the relative fractions of prompt versus non-prompt background, as well as apparent lifetimes, mixing frequencies and dilutions, and common effective resolution parameters \hat{b}_i that best describe the events with high weights for being background in the B_{flav} and B_{CP} samples. Roughly, uds continuum, short-lived charm continuum, and short-lived $B\bar{B}$ backgrounds fall into the prompt category, while some fraction of long-lived charm and $B\bar{B}$ are treated as non-prompt. The standard vertex algorithms are of course applied to all candidates in the B_{flav} and B_{CP} samples. Thus, the B_{rec} vertex fit must converge and the usual procedure is applied to obtain a self-consistent vertex for the remaining tracks on the tag side of the event, irrespective of whether the candidate event is eventually classified as signal or background. To maintain a parallel treatment with the signal PDF, an effective resolution function $\mathcal{R}(\delta_t; \hat{b}_i)$ is used to scale the result of the calculated uncertainty on Δz for background events. The actual choice of background parameters is described in Section 8.3 below, along with additional assumptions.

8.2.2 Background formulation for $B^0 \rightarrow J/\psi K_L^0$

The higher background level in the $B^0 \rightarrow J/\psi K_L^0$ channel requires a more extensive treatment of its properties. As discussed in Section 4.4, the data are used to determine the relative fraction of signal, background from $B \rightarrow J/\psi X$ events, and events with a misreconstructed $J/\psi \rightarrow \ell\ell$ candidate. Along with a Monte Carlo simulation of the channels that contribute to the $B \rightarrow J/\psi X$ background, this information is used to formulate the PDF model. The probability density functions \mathcal{F}_{\pm} of Eq. 12 are modified to include contributions identified $B \rightarrow J/\psi X$ channels and the non- J/ψ background component. Each event is classified according to its flavor tagging category (i), flavor tag value (\pm), and the K_L^0 reconstruction category (k), which is either EMC or IFR.

The shape of the signal and background ΔE functions are determined either from data (non- J/ψ contribution) or from Monte Carlo samples (signal and $J/\psi X$ background).

Some of the decay modes in the inclusive J/ψ background, such as $J/\psi K^{*0}$ and $J/\psi K_s^0$, have an expected CP asymmetry. The mistag fractions for all CP modes in the inclusive J/ψ background are determined with the Monte Carlo simulation and found to be consistent with the values for the signal. The signal mistag fractions are assumed to apply to the CP modes in the inclusive J/ψ background.

The Δt resolution for the $B \rightarrow J/\psi X$ background is shown with Monte Carlo simulation to be very similar to the signal resolution, while the resolution of the non- J/ψ background is measured with the J/ψ sideband sample. The non- J/ψ Δt resolution parameters are varied by their statistical uncertainties to estimate the systematic uncertainty.

8.3 Free parameters for the $\sin 2\beta$ and Δm_d fits

The unbinned likelihood fits employed by *BABAR* for $\sin 2\beta$ and Δm_d have free parameters that can be summarized as follows:

- **Value of $\sin 2\beta$ or Δm_d**
- **Signal resolution function:** Parameters \hat{a}_i to describe the resolution function for the signal, in terms of a scale factor S_1 for the event-by-event Δz resolution errors of the core Gaussian components, individual core bias scale factors $b_{1,i}$ for the four tagging categories and a common tail bias b_2 , and the tail f_2 and outlier f_3 fractions; the scale factor of the tail component is fixed to 3.0 and the width of the outlier component is fixed to 8 ps with zero bias. In some cases this set is doubled to account for different periods of tracking and vertexing reconstruction quality.
- **Signal dilutions:** Eight parameters to describe the measured average dilutions $\langle \mathcal{D} \rangle_i$ and dilution differences $\Delta \mathcal{D}_i$ in each tagging category.
- **Background resolution function:** Six parameters are used to describe a common resolution function for all non-peaking backgrounds. The resolution function is taken as a single Gaussian distribution with a scale factor S_1 for the event-by-event Δz errors and a common bias scale factor b_1 , and an outlier fraction f_3 ; the width of the outlier component is taken to be a fixed 8 ps with zero bias. As with the signal resolution function, in some cases a separate set of resolution function

parameters is required for different reconstruction periods.

- **B_{flav} background composition parameters:** A total of 13 parameters describe the B_{flav} background composition. Several assumptions are made to simplify the parameterization, such as removing the mixing background contribution, and assign a corresponding systematic uncertainty. The size of the peaking background is determined from Monte Carlo simulation to be $\delta_{\text{peak}}^{\text{flav}} = (1.5 \pm 0.5)\%$ of the signal contribution in each tagging category. This contribution is predominately from B^+ events, so $\Delta m_{i,\text{peak}} = 0$, $\Gamma_{i,\text{peak}}^{\text{flav}} = \Gamma_{B^+}$ and $D_{i,\text{peak}}^{\text{flav}}$ are taken from the B^+ data sample. The effective dilutions for the prompt ($D_{i,1}^{\text{flav}}$, 4 parameters) and non-prompt ($D_{i,2}^{\text{flav}}$, 4 parameters) contributions are allowed to vary. The relative amount of these two contributions is allowed to vary independently in each tagging category (4 parameters). For the non-prompt contribution, $\Gamma_{i,2}^{\text{flav}}$ is assumed to be the same for all tagging categories, giving one free parameter.
- **CP background composition parameters:** One parameter, the fraction of prompt relative to non-prompt background, assumed to be the same for each tagging category, is allowed to float to describe the CP background properties. The effective dilutions of the non-prompt and peaking contribution are set to zero ($D_{i,2}^{CP} = D_{i,\text{peak}}^{CP} = 0$), corresponding to no CP -asymmetry in the background. The size and parameters of the peaking background are determined from Monte Carlo simulation. The fraction of peaking background is $\delta_{\text{peak}}^{CP} = (1 \pm 1)\%$ of the signal contribution, independent of tagging category. This contribution is assumed to have lifetime parameters in common with the signal. Finally, the lifetime of the non-prompt background is assumed to be τ_{B^0} in all tagging categories.

A summary of the final set of parameters for the Δm_d and $\sin 2\beta$ fits is provided in Sections 9.1 and 10.1. Belle uses a strategy of employing separate auxiliary fits to obtain many of the equivalent resolution and background parameters, which leads to a smaller number of free parameters in the final Δm_d or $\sin 2\beta$ fits.

8.4 Blind analysis

A blind analysis technique was adopted for the extraction of $\sin 2\beta$ and Δm_d in order to eliminate possible experimenter's bias. Typically this involves a method that hides not only the central value for these parameters from the unbinned maximum-likelihood fit, but also the visual CP asymmetry in the Δt distribution. The error on both the asymmetry and Δm_d is not hidden.

The amplitude of the asymmetry $\mathcal{A}_{CP}(\Delta t)$ from the fit was hidden by a one-time choice of sign flip and arbitrary offset based on a user-specified key word. The sign flip hides whether a change in the analysis increases or decreases the resulting asymmetry. However, the magnitude of the change is not hidden. The visual CP asymmetry in the Δt distribution is hidden by multiplying Δt by the sign of the tag and adding an arbitrary offset.

With these techniques, systematic studies can be performed while keeping the numerical value of $\sin 2\beta$ or Δm_d hidden. For example, the hidden Δt distributions allow one to check whether there is consistency between B^0 and \bar{B}^0 tagged events or fit results in the different tagging categories can be compared to each other, since each fit is hidden in the same way. The analysis procedure for extracting $\sin 2\beta$ and Δm_d are then frozen prior to unblinding.

9 B^0 flavor oscillations and mistag rates

9.1 Result for Δm_d from *BABAR*

Table 10. Summary of parameters included in unbinned likelihood fit to the mixed and unmixed B_{flav} sample. For the signal and background resolution functions the number of parameters is doubled to allow a description of two different periods of vertex reconstruction performance.

Fit parameters	Number	Main sample
Δm_d	1	Signal
Mistag fractions for B^0 \bar{B}^0 tags	8	Signal
Signal resolution function	2×8	Signal
Description of background Δt	$5 + 8$	Sidebands
Background resolution function	2×3	Sidebands
B lifetime from PDG2000	0	Fixed
Total	44	

At *BABAR*,²⁵ the value for Δm_d , the dilution factors \mathcal{D}_i , the Δt resolution parameters \hat{a}_i , and the parameters for the background description are determined by simultane-

ously fitting the Δt distributions of mixed and unmixed events in the flavor-eigenstate B^0 sample with $m_{\text{ES}} > 5.2 \text{ GeV}/c^2$. The likelihood function has already been described in Section 8, including the addition of separate mistag rates for B^0 and \bar{B}^0 tags. The breakdown of fit parameters is summarized in Table 10. The selection of the B_{flav} candidates is made with the techniques described in Section 4 in a data sample equivalent to 29.7 fb^{-1} . The flavor oscillation measurement also requires that there be a determination of Δt and a valid tag, based on the algorithms described in Sections 5 and 7. For the mixing result, more restrictive requirements $|\Delta t| < 20 \text{ ps}$ and $\sigma_{\Delta t} < 1.4 \text{ ps}$ are applied to the proper time-difference measurement. In addition, identified kaons in the B_{tag} decay are rejected in the reconstruction of the tagging vertex, as this is clearly a track which must originate from the secondary charm decay. These additional requirements are intended to reduce systematic errors on the precision Δm_d measurement. The final sample consists of 12310 fully-reconstructed and tagged B^0 candidates with $m_{\text{ES}} > 5.2 \text{ GeV}/c^2$, of which 7399 are in the signal region $m_{\text{ES}} > 5.27 \text{ GeV}/c^2$.

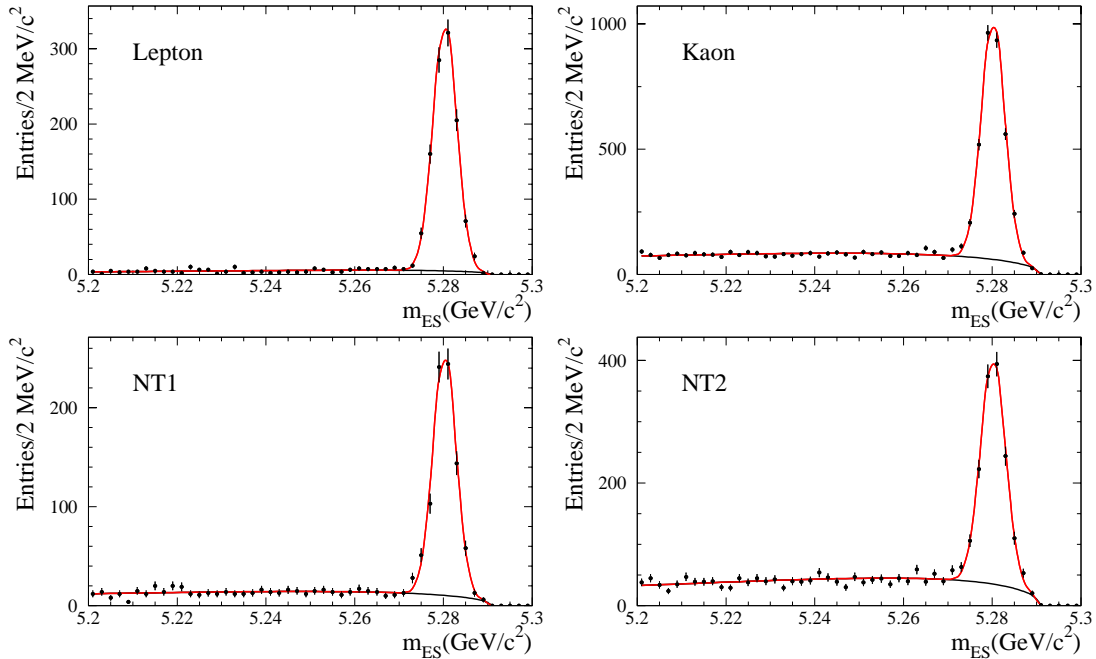


Fig. 63. Distribution of m_{ES} for mixing B_{flav} candidates in separate tagging categories (Lepton, Kaon, NT1 and NT2), overlaid with the result of a fit with a Gaussian distribution for the signal and an ARGUS function for the background. [BABAR]

The breakdown of this mixing B_{flav} sample into individual tagging categories is shown in Figure 63 as a function of m_{ES} . Superimposed on the observed mass spectra

are the results of the fits with a Gaussian distribution for the signal and an ARGUS function for the background. The tagging efficiency and signal purity for the individual tagging categories in data are extracted from fits to the m_{ES} distributions and are listed in Table 11. The efficiency for each tagging category is defined as the ratio of the number of signal events for each tag over the total number of signal events after imposition of vertex cuts. These fits are also used to assign a signal and background probability to each event in the sample, based on its reconstructed m_{ES} . These probabilities are then used as weights for signal and background terms in contributing to the likelihood.

Table 11. Tagging efficiencies for hadronic B^0 decays and signal purities in data, shown separately for the four tagging categories. Signal purities are estimated for $m_{ES} > 5.27 \text{ GeV}/c^2$.

Tagging Category	Efficiency [%]	Signal	Purity [%]
Lepton	11.8 ± 0.3	1097 ± 34	96.0 ± 0.7
Kaon	33.9 ± 0.5	3156 ± 63	84.6 ± 0.7
NT1	8.6 ± 0.3	798 ± 31	88.9 ± 1.2
NT2	13.9 ± 0.4	1293 ± 43	79.4 ± 1.3
Full sample	68.1 ± 0.4	6347 ± 89	85.8 ± 0.5

The Δt distributions of the signal ($m_{ES} > 5.27 \text{ GeV}/c^2$) and background ($m_{ES} < 5.27 \text{ GeV}/c^2$) candidates, overlaid with the projection of the likelihood fit, are shown in Figure 64. In Figure 65 the mixing asymmetry of Eq. 5 is plotted; the time-dependence of the mixing probability is clearly visible.

The tagging separation $Q = \epsilon_{tag}(1 - 2w)^2$ is calculated from the efficiencies and the mistag rates. Summing over all tagging categories, the combined effective tagging efficiency is $Q \approx 27\%$.

Two small corrections, which are described in more detail in Sections 9.3.2 and 9.3.4 together with their assigned systematic errors, are applied to the output of the fit. The value of Δm_d obtained after applying these corrections is

$$\Delta m_d = 0.516 \pm 0.016 \pm 0.010 \text{ ps}^{-1},$$

where the first error is statistical and the second systematic. This result is comparable

in precision to and in agreement with the world average prior to the B Factory experiments.¹⁸ Since the measurement uses all the ingredients required for the CP asymmetry determination, this result is also a crucial step in validating these studies as well.

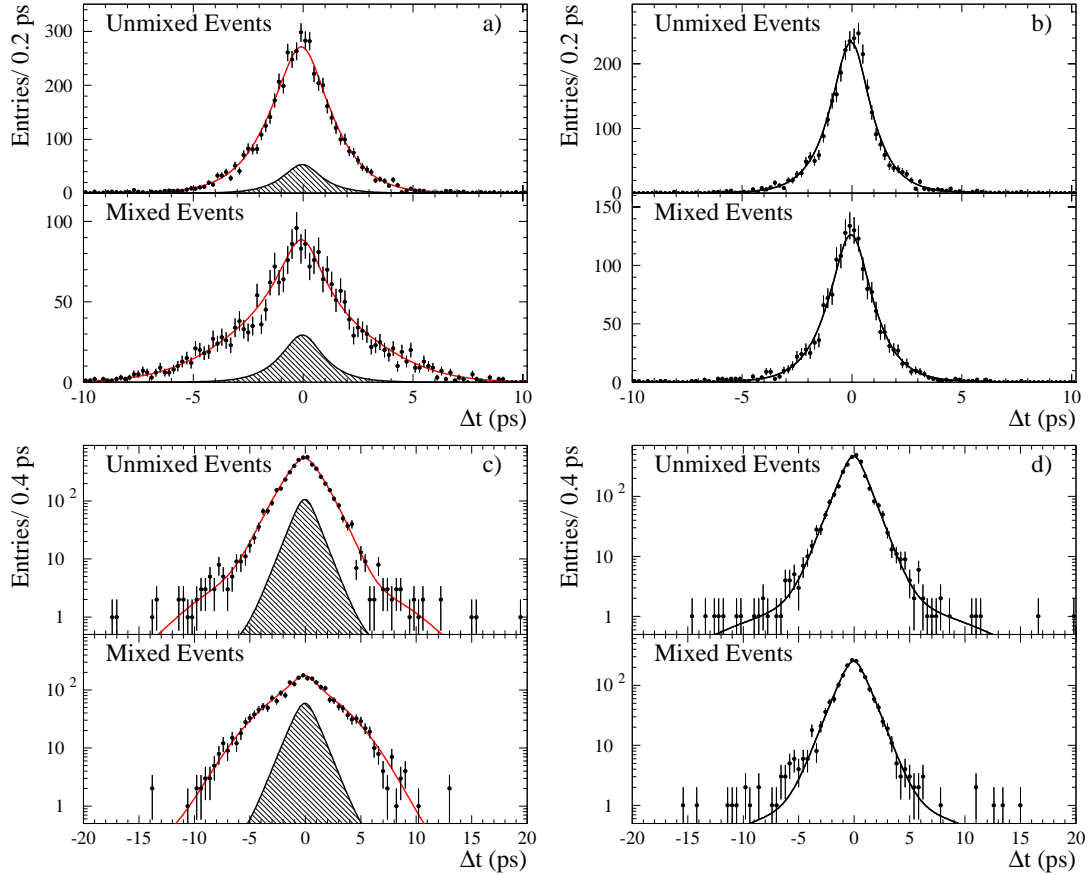


Fig. 64. Distributions of Δt for unmixed (upper panel) and mixed (lower panel) events in the hadronic B sample, divided into a signal region $m_{ES} > 5.27 \text{ GeV}/c^2$ with a) a linear and c) logarithmic scale, and a sideband region $m_{ES} < 5.27 \text{ GeV}/c^2$ with b) a linear and d) logarithmic scale. In all cases, the data points are overlaid with the result from the global unbinned likelihood fit, projected on the basis of the individual signal and background probabilities, and event-by-event Δt resolutions, for candidates in the respective samples. In a) and c), the Δt distributions obtained from the likelihood fit to the full sample are overlaid, along with the simultaneously determined background distribution shown as the curve in b) and d). [BABAR]

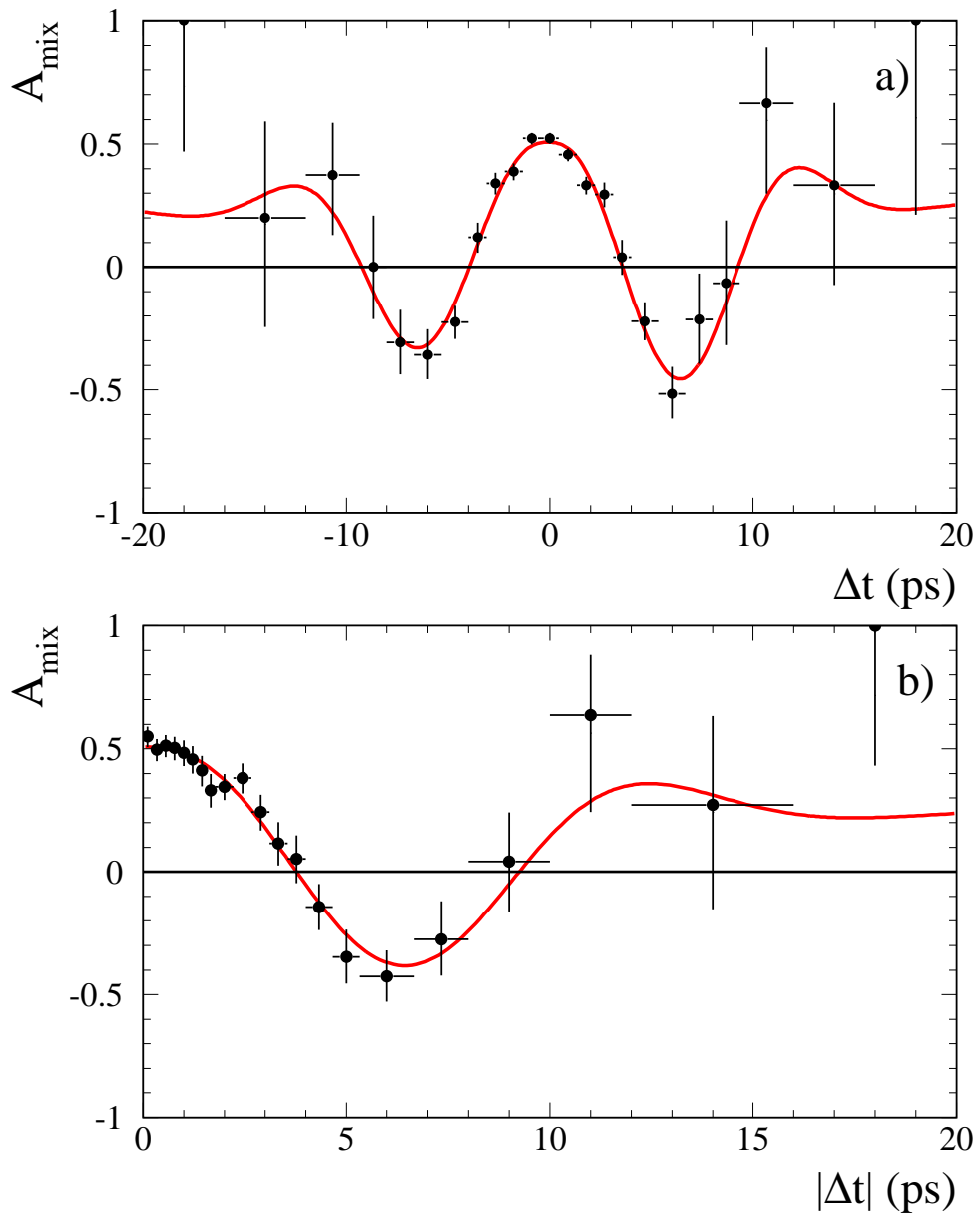


Fig. 65. Time-dependent asymmetry $\mathcal{A}(\Delta t)$ between unmixed and mixed events for hadronic B candidates with $m_{\text{ES}} > 5.27 \text{ GeV}/c^2$, a) as a function of Δt ; and b) folded as a function of $|\Delta t|$. The asymmetry in a) is due to the fitted bias in the Δt resolution function. [BABAR]

9.2 Result for Δm_d from Belle

A similar analysis of mixed and unmixed events with one B reconstructed in a flavor eigenstate mode has been done by Belle.²⁶ In this case the value for Δm_d and six dilution factors \mathcal{D}_i are determined from a simultaneous fit to the Δt distributions of mixed and unmixed events with $m_{\text{ES}} > 5.27 \text{ GeV}/c^2$. The likelihood function is analogous to that used for the *BABAR* measurement. However, the description of the background is in terms of a prompt and a lifetime component, whose parameters are fixed by sideband events in a separate fit. Likewise, the signal Δt resolution function and its parameters is obtained separately from the Belle lifetime fit described earlier. The selection of the B_{flav} candidates is made with the techniques described in Section 4.3.1 in a data sample equivalent to 29.1 fb^{-1} . The flavor oscillation measurement also requires that there be a determination of Δt and a valid tag, based on the standard Belle algorithms described in Sections 5 and 7. The final sample consists of 6660 fully-reconstructed and tagged B^0 candidates with $m_{\text{ES}} > 5.27 \text{ GeV}/c^2$ and $|\Delta E| < 3\sigma$, of which 2269 are in the mode $\bar{B}^0 \rightarrow D^+\pi^-$, 2490 in $\bar{B}^0 \rightarrow D^{*+}\pi^-$, and 1901 in $\bar{B}^0 \rightarrow D^{*+}\rho^-$.

The Δt distributions of the signal candidates ($m_{\text{ES}} > 5.27 \text{ GeV}/c^2$), overlaid with the projection of the likelihood fit, are shown in Figure 66. In Figure 67 the mixing asymmetry of Eq. 5 is plotted; the time-dependence of the mixing probability is clearly visible.

The value of Δm_d obtained from the fit is

$$\Delta m_d = 0.528 \pm 0.017 \pm 0.011 \text{ ps}^{-1},$$

where the first error is statistical and the second systematic. Again, this measurement is consistent with the world average value for Δm_d prior to the B Factory results.¹⁸ Note that both the *BABAR* and Belle results are statistics dominated, with almost five times the data sample already available.

9.3 Details of systematic error estimation at *BABAR*

Systematic errors are similar for the *BABAR* and Belle measurements and can be grouped into four categories: signal properties and description, background properties and description, fixed external parameters and statistical limitations of Monte Carlo validation tests of the fitting procedure. A summary of these sources for the hadronic B^0 sample at *BABAR* is shown in Table 12. In the following, the individual contributions are referenced by the lettered lines in this table.

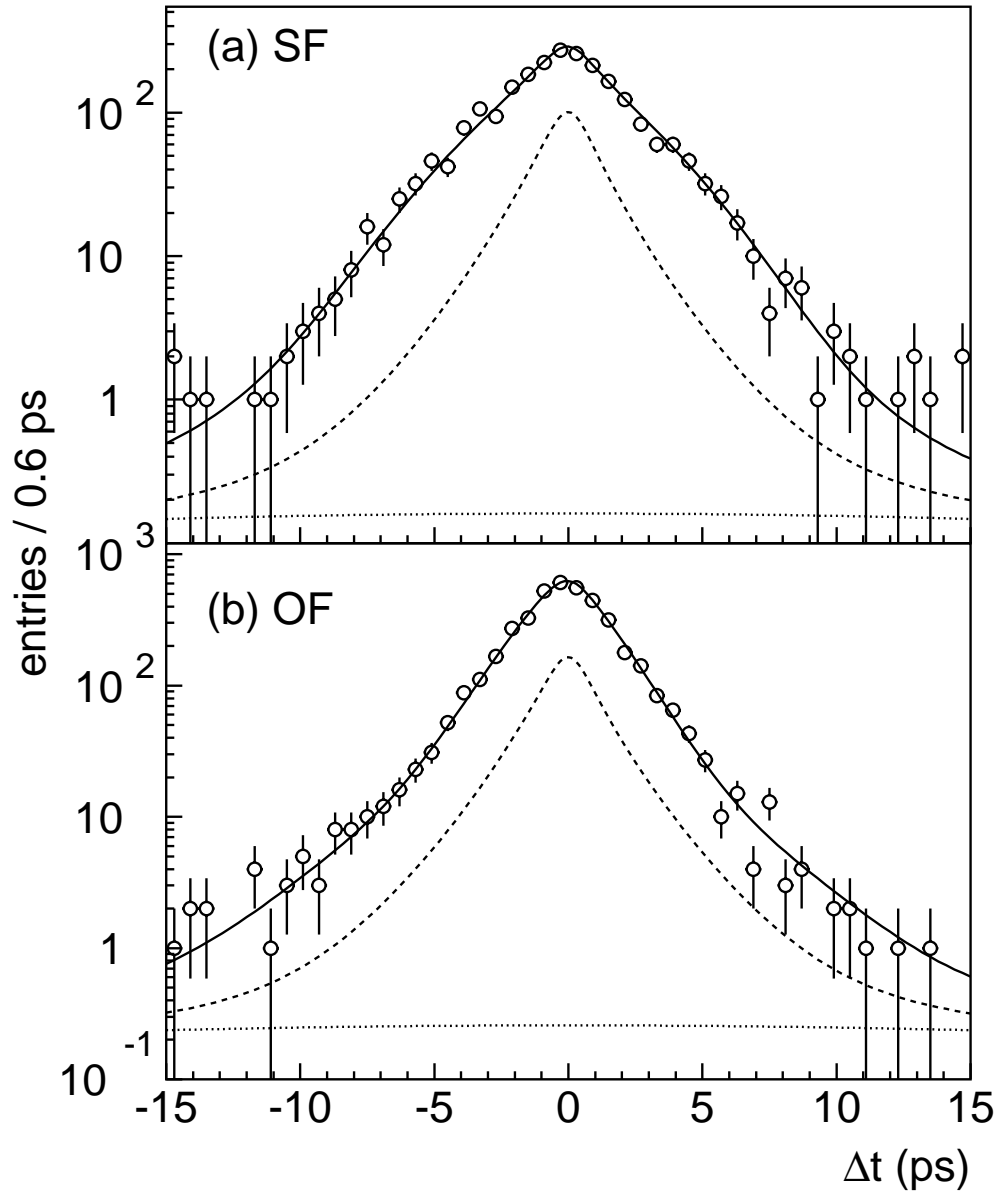


Fig. 66. Distributions of Δt for mixed or “Same Flavor” (SF or upper panel) and unmixed or “Opposite Flavor” (OF or lower panel) events in the hadronic B sample. In all cases, the data points are overlaid with the result from the global unbinned likelihood fit, projected on the basis of the individual signal and background probabilities, and event-by-event Δt resolutions, for candidates in the respective samples. [Belle]

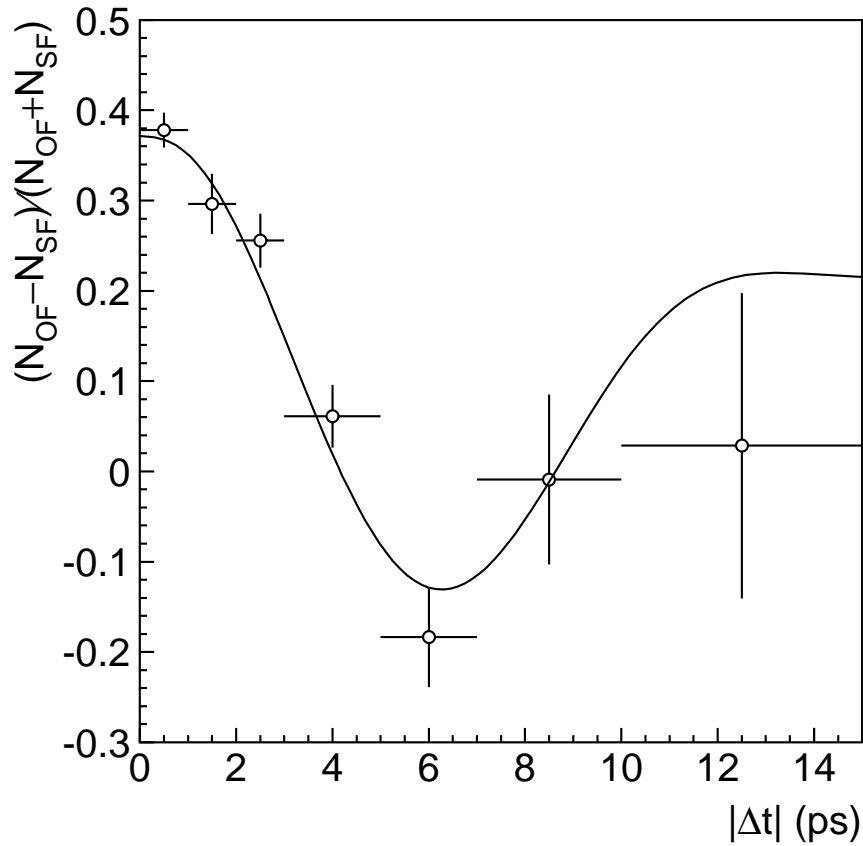


Fig. 67. Time-dependent asymmetry $\mathcal{A}(\Delta t)$ between unmixed (opposite flavor) and mixed (same flavor) events for hadronic B candidates with $m_{\text{ES}} > 5.27 \text{ GeV}/c^2$, folded as a function of $|\Delta t|$. [Belle]

9.3.1 Signal properties and description

For the signal events, the use of a double Gaussian plus outlier model for re-scaling the event-by-event Δt errors as part of the likelihood fit means that uncertainties in the vertex resolution are incorporated into the statistical error on Δm_d , including proper treatment of all correlations. Assuming that this model is sufficiently flexible to accommodate the observed distribution in data, no additional systematic error need be assigned. The contribution to the total statistical error due to the vertex resolution can be extracted by fitting the data twice: once holding all parameters except Δm_d fixed, and once allowing the resolution function parameters to vary in addition to Δm_d . Subtracting in quadrature the respective errors on Δm_d from the two fits shows that $\pm 0.005 \text{ ps}^{-1}$ of the statistical error can be attributed to the resolution parameters.

To determine the systematic error due to the assumed parameterization of the resolution model, a number of possible misalignment scenarios are applied to a sample of simulated events. By comparing the value of Δm_d derived from these misaligned samples to the case of perfect alignment, a systematic uncertainty of $\pm 0.004 \text{ ps}^{-1}$ (a) is derived.

An additional systematic error is attributed to uncertainties in the treatment of the small fraction of Δt outliers that are the result of misreconstructed vertices. The stability of the Δm_d result is examined under variation of the width of the third Gaussian component in the resolution function between 6 and 18 ps, and through replacement of the third Gaussian with a uniform distribution and varying the width between 8 and 40 ps. On this basis, a systematic uncertainty of $\pm 0.002 \text{ ps}^{-1}$ is attributed to the outlier treatment (b).

As described in detail in Section 5.1, the beamspot position is an integral part of the determination of Δt . Increasing its vertical size by up to $80 \mu\text{m}$, and systematically biasing its vertical position by up to $80 \mu\text{m}$, results in a corresponding variation of Δm_d by less than 0.001 ps^{-1} (c).

The requirement on the maximum allowed value of $\sigma_{\Delta t}$ is varied between 1 and 2.4 ps, and the observed variation of 0.003 ps^{-1} in Δm_d is assigned as a systematic uncertainty (d). The observed dependence is mainly due to correlations between tagging and vertexing, as described in Sec. 9.3.4.

9.3.2 Background properties

A systematic uncertainty in Δm_d arises from our ability to separate signal from background as a function of m_{ES} . This uncertainty can be estimated by varying the width and height of the fitted Gaussian peak in m_{ES} , the slope parameter of the ARGUS background shape, and the normalizations of the signal and backgrounds by one standard deviation around their central values, resulting in an uncertainty of $\pm 0.002 \text{ ps}^{-1}$ in Δm_d (e).

As discussed in Sec. 8.2.1, the Δt distribution of the background is described by the combination of a prompt component and a lifetime component. To estimate the systematic uncertainty due to this choice, an additional component is added, with its own separate lifetime, that is allowed to mix; the observed value of Δm_d changes by 0.001 ps^{-1} (f). Similarly, adding an additional Gaussian distribution to the Δt background resolution function changes Δm_d by no more than 0.001 ps^{-1} (g).

Table 12. Systematic uncertainties and contributions to statistical errors for Δm_d obtained with the likelihood fit to the hadronic B^0 sample.

Source	$\sigma(\Delta m_d)$ [ps ⁻¹]
Signal properties	
(a) SVT alignment	0.004
(b) Δt outlier description	0.002
(c) Beamspot position/size	0.001
(d) $\sigma_{\Delta t}$ requirement	0.003
Background properties	
(e) Background fraction	0.002
(f) Background Δt structure	0.001
(g) Background Δt resolution	0.001
(h) Sideband extrapolation	0.002
(i) Peaking B^+ background	0.002
External parameters	
(j) z scale	<0.002
(k) z boost (parameters)	0.001
(l) z boost (method)	0.001
(m) B^0 lifetime	0.006
Monte Carlo studies	
(n) Signal MC statistics	0.003
(o) Tag-side D composition & lifetime	0.001
(p) Right/wrong tag resolution differences	0.001
Total systematic error	0.010
Statistical error	0.016
Contribution due to resolution function	0.005
Contribution due to mistag rate	0.005
Total error	0.019

Finally, the composition of the background changes slightly as a function of m_{ES} , since the fraction of background due to continuum production slowly decreases towards the B mass. As a result, the Δt structure of the background could change as well. To study this dependence, the m_{ES} sideband region is split into seven mutually exclusive, $10 \text{ MeV}/c^2$ -wide intervals, and repeat the Δm_d fit with each of these slices in turn. The variation of Δm_d is then extrapolated as a function of the position of the sideband slice relative to the B mass. The value of Δm_d is corrected by -0.002 ps^{-1} as obtained from this extrapolation, and the statistical uncertainty of 0.002 ps^{-1} of this procedure is assigned as a systematic error on Δm_d (h).

A small fraction (about 1.5%) of the events attributed to the B^0 signal by the fit to the m_{ES} distribution consists of B^+ events, mainly due to the swapping of a soft π^0 with a charged pion as described in Section 4.3.1. The uncertainty on this peaking fraction is propagated to Δm_d , yielding a systematic error of 0.002 ps^{-1} (i).

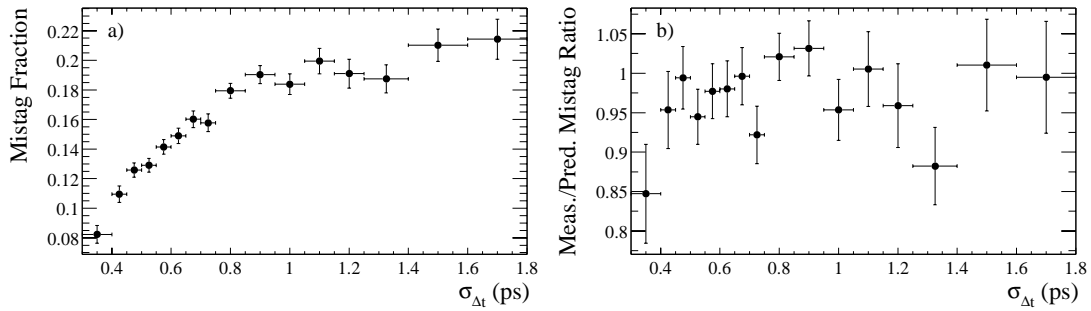


Fig. 68. a) Correlation between the event-by-event error on Δt ($\sigma_{\Delta t}$) and the mistag rate in the $K\pi$ category from Monte Carlo simulation; b) Dependence of mistag rate on $\sigma_{\Delta t}$ after scaling the mistag rate by $\sqrt{\sum p_t^2}$.

9.3.3 External parameters

An error in the boost of the $\Upsilon(4S)$ system (0.1%) or in the knowledge of the z scale of the detector, as described in Section 5.1, could bias the Δm_d measurement because these parameters are used to reconstruct the decay length difference Δz and to convert it to the decay time difference Δt . The uncertainties on these quantities are propagated to Δm_d and lead to systematic uncertainties of 0.001 ps^{-1} (l) and less than 0.002 ps^{-1} (j), respectively. In addition to these, the difference of 0.001 ps^{-1} (k) in the value of Δm_d obtained by using the Δz to Δt conversion described in Eq. 25 instead of Eq. 26

is assigned as a systematic error. Finally, in the likelihood fit, the B^0 lifetime is fixed to the PDG value.¹⁸ The present uncertainty on this value of ± 0.032 ps leads to a systematic error of ∓ 0.006 ps⁻¹ (m).

9.3.4 Monte Carlo validation of measurement technique

Candidate selection criteria, or the analysis and fitting procedure, could potentially cause systematic biases in the measurement of Δm_d . These potential biases are estimated by repeating the analysis with a large sample of Monte Carlo events, which are generated with the full GEANT3³⁷ detector simulation. In the Monte Carlo sample, the fitted result for Δm_d is shifted by $+0.007 \pm 0.003$ ps⁻¹ from the input value. A corresponding correction with this central value is applied to the fitted result with data, and the uncertainty is assigned as a systematic error (n).

The main cause of this bias is a small correlation between the mistag rate and the Δt resolution that is not modelled in the likelihood function. This correlation is seen most readily in data for K_{tag} and is shown for simulation in Figure 68a. It is found that both the mistag rate for kaon tags and the event-by-event error $\sigma_{\Delta t}$ depend inversely on $\sqrt{\sum p_t^2}$, where p_t is the transverse momentum with respect to the z axis of tracks from the B_{tag} decay. Correcting for this dependence of the mistag rate removes most of the correlation between the mistag rate and $\sigma_{\Delta t}$, as can be seen in Figure 68b. The mistag rate dependence originates from the kinematics of the physics sources for wrong-charge kaons. The three major sources of mistags are wrong-sign D^0 mesons from B decays to double charm, wrong-sign kaons from D^+ decays, and kaons produced directly in B decays. All these sources produce a spectrum of charged tracks that have smaller $\sqrt{\sum p_t^2}$ than B decays that produce a correct tag. The Δt resolution dependence originates from the $1/p_t^2$ dependence of σ_z for the individual contributing tracks.

Since the effect is small and well described by the Monte Carlo simulation, the impact of this correlation is treated as a correction, rather than building the effect into the likelihood function. Additional systematic errors related to the tag-side properties that could affect the accuracy of the description of this correlation in the simulation are included. In particular, the D^0 , D^+ , and D_s^+ meson branching fractions, the D meson lifetimes, and the wrong-sign kaon production rates in B meson decays are all varied. These studies lead to an assigned systematic error of ± 0.001 ps⁻¹ (o).

In addition, the possibility that correctly and incorrectly tagged events could have

different resolution functions is considered. Based on Monte Carlo studies of the variation in the fitted value for Δm_d with and without allowing for independent resolution functions for correctly and incorrectly tagged events, an uncertainty of $\pm 0.001 \text{ ps}^{-1}$ is assigned to this source (p).

10 CP violation in neutral B decays

10.1 Results for $\sin 2\beta$ from $BABAR$

At $BABAR$,²⁷ the value of $\sin 2\beta$, the dilution factors \mathcal{D}_i , the Δt resolution parameters \hat{a}_i , and the background fractions and time distribution parameters are extracted with a simultaneous unbinned maximum-likelihood fit to the flavor-eigenstate B_{flav} and B_{CP} samples with $m_{\text{ES}} > 5.2 \text{ GeV}/c^2$. The likelihood function has already been described in Section 8. The breakdown of fit parameters is summarized in Table 13. The B_{flav} and B_{CP} samples are obtained with the techniques described in Section 4 in a data sample equivalent to 81.3 fb^{-1} . The asymmetry measurement also requires that there be a determination of Δt based on the algorithms described in Section 5. The looser requirements $|\Delta t| < 20 \text{ ps}$ and $\sigma_{\Delta t} < 2.4 \text{ ps}$ are applied to the proper time difference measurement.

Table 13. Summary of parameters included in unbinned likelihood fit to the B^0 and \bar{B}^0 B_{CP} sample and the mixed and unmixed B_{flav} sample. For the signal and background resolution functions the number of parameters is doubled to allow a description of two different periods of vertex reconstruction performance.

Fit parameters	Number	Main sample
$\sin 2\beta$	1	CP
Mistag fractions for B^0 \bar{B}^0 tags	8	B_{flav}
Signal resolution function	8	B_{flav}
Description of background Δt	17	Sidebands
B lifetime, Δm_d from PDG2002	0	Fixed
Total	34	

The basic ingredients for flavor-tagging the second B decay in the event is described

in Section 7. For the summer 2002 result, additional study of the tagging algorithms resulted a 7% improvement in performance in $Q = \epsilon(1 - 2w)^2$. The basic strategy continues to be based on physics-motivated tagging categories, as illustrated in Figure 69. Seven sub-taggers are defined as input to a combined tagging neural network algorithm, whose output is organized into nine tagging categories. The tagging categories are further grouped into four tagging physics categories, without loss of statistical power. The sub-taggers identify electrons, muons, kinematic leptons, the three best kaons, slow-pions, kaon-pion correlations, and the highest center-of-mass track. The neural network output tagging categories range in purity from kaon-lepton, leptons, correlated kaon-soft pion combinations, two classifications of kaon tagging, and other tagging information.

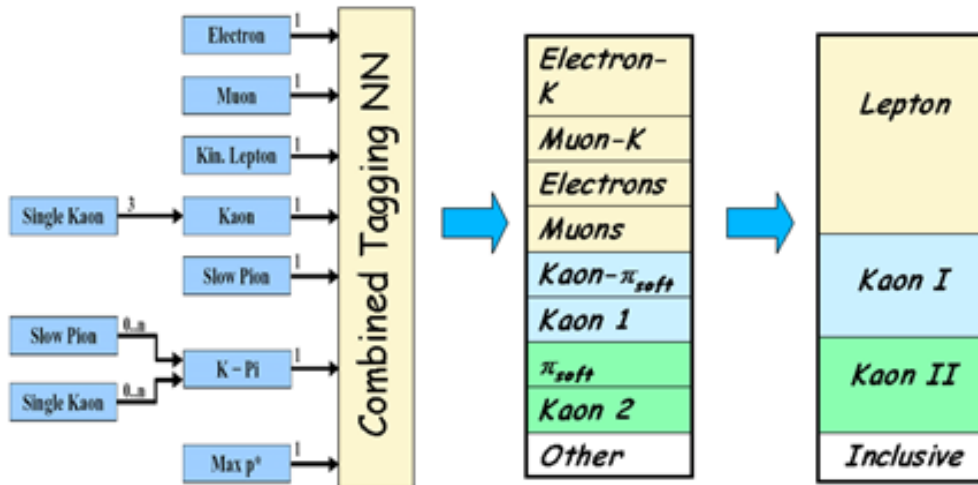


Fig. 69. Revised organization of tagging inputs to multivariate neural network analysis and new tagging categories employed by *BABAR* for the summer 2002 result on $\sin 2\beta$.

Figure 70 shows a comparison between the distribution of neural network outputs in the B_{flav} and B_{CP} samples, where the expected good agreement supports the underlying assumption that tagging performance in the two samples is identical. Likewise, there is excellent agreement between the distribution of the neural network variable in data and Monte Carlo simulation, although tagging performance is determined directly from the data.

The m_{ES} distribution for events in $\eta_{CP} = -1$ modes, separated into tagging categories, is shown in Figure 71. The signal and background probability assignments for each candidate in the $\eta_{CP} = -1$ sample is determined from these fits and the measured

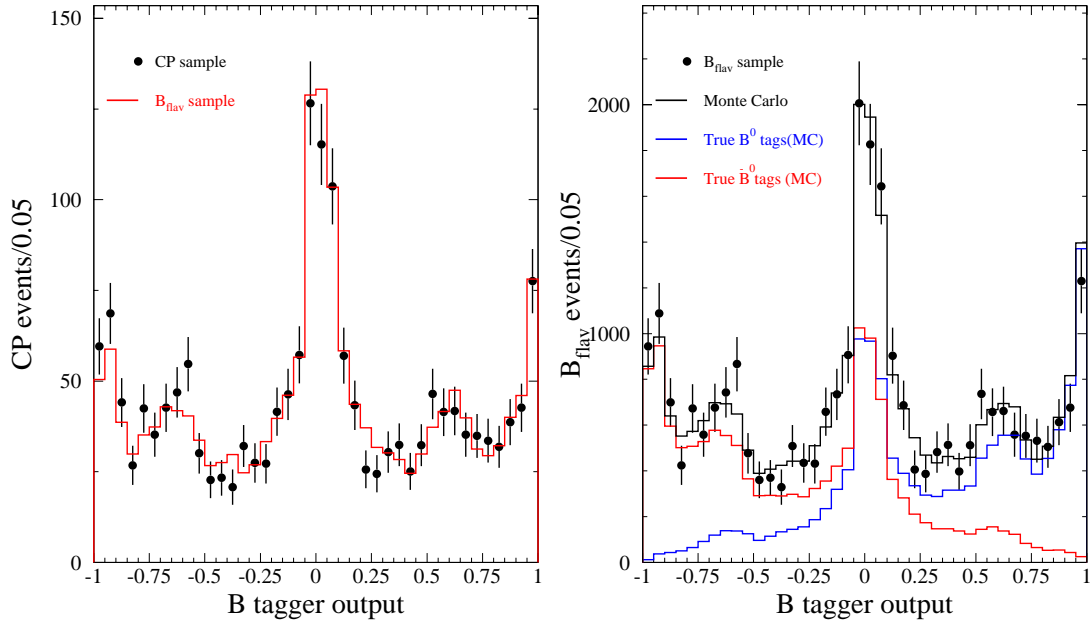


Fig. 70. Comparison tests with the new *BABAR* tagger algorithm. (Left) Distribution of the output variable from the *B* tagger neural network for the B_{rec} (histogram) and B_{CP} (points) samples. (Right) Distribution of the neural network output variable for the B_{CP} sample (points) and Monte Carlo simulation (histograms), including contributions from true B^0 and \bar{B}^0 decays.

value for m_{ES} . While the background level in all four tagging categories is rather small, this is particularly so for the Lepton tags.

The value of $\sin 2\beta$ obtained from the unbinned maximum likelihood fit to the combined $\eta_{CP} = -1$, $\eta_{CP} = +1$, and $J/\psi K^{*0}$ *CP* samples is

$$\sin 2\beta = 0.741 \pm 0.067 \pm 0.033,$$

where the first error is statistical and the second systematic. The mistag fractions and vertex parameters obtained at the same time are predominantly determined by the B_{flav} sample. The *CP* asymmetry and parameters describing the background for the *CP* events are determined by the *CP* sample. The distribution of events as a function of Δt for B^0 and \bar{B}^0 tags is shown in Figure 72 for the $\eta_{CP} = -1$ and $J/\psi K_L^0$ samples, while the visible asymmetries are provided with fit projections in Figure 73. For this purpose, only those events with $m_{\text{ES}} > 5.27 \text{ GeV}/c^2$ in the $\eta_{CP} = -1$ and $J/\psi K^{*0}$ samples or $\Delta E < 10 \text{ MeV}$ in the $\eta_{CP} = +1$ sample are included. Overlaid on the data are the projections of the signal and background Δt distributions obtained from the fit, where

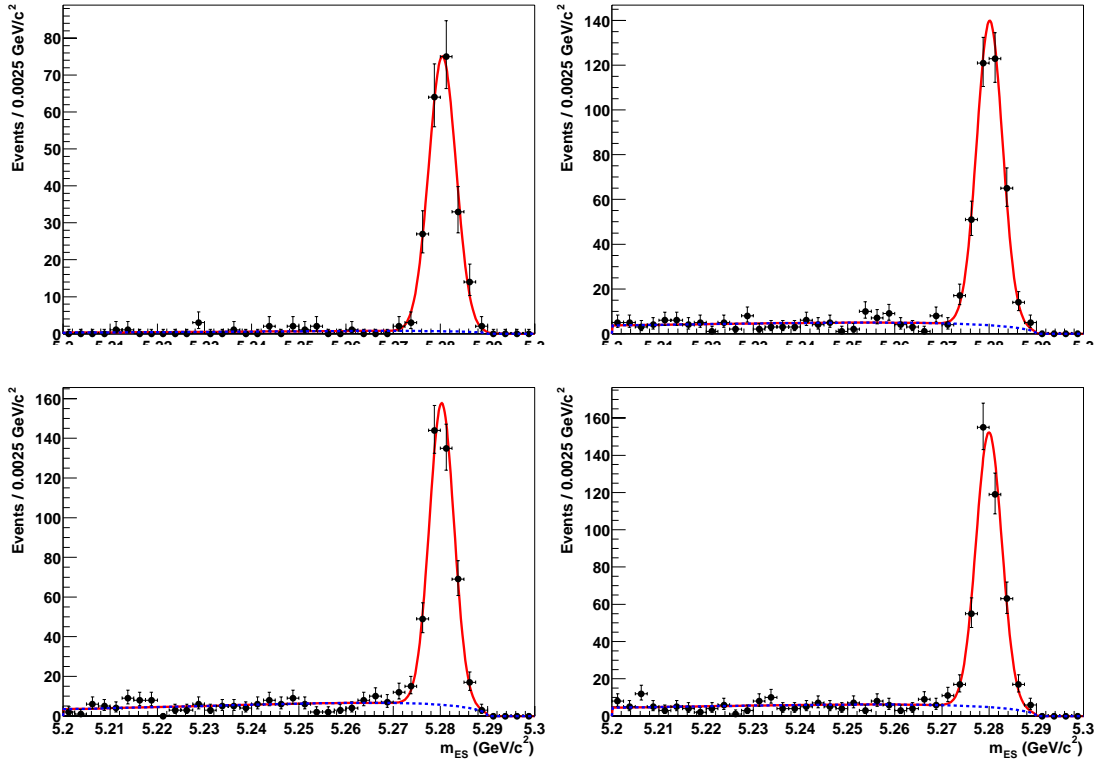


Fig. 71. Distribution of m_{ES} for $\eta_{CP} = -1$ candidates in separate tagging categories (Lepton, Kaon I, Kaon II and Inclusive), overlaid with the result of a fit with a Gaussian distribution for the signal and an ARGUS function for the background.

the latter is normalized to the projected background level. The results for individual CP channel, tagging category, B^0 versus \bar{B}^0 tag, J/ψ decay mode and data-taking period are all consistent, as shown in Figure 75 and Table 14.

One particular subset provides a beautiful demonstration of matter-antimatter asymmetry. Figure 74 shows the Δt distributions for 200 lepton-tagged events with $\eta_{CP} = -1$ sample. Since this sample has a 98% signal purity, a 3.3% mistag rate, and on average a 20% better Δt resolution the difference between the B^0 - and \bar{B}^0 -tagged is quite clearly visible. Indeed, this sample alone yields a value of $\sin 2\beta = 0.79 \pm 0.11$.

The average dilutions and dilution differences for B^0 and \bar{B}^0 tags obtained from the fit to the B^0 flavor eigenstate and full CP sample, and the corresponding tagging efficiencies, are summarized in Table 15. The total tagging efficiency is found to be $(65.6 \pm 0.5)\%$ (statistical error only). The lepton categories have the lowest mistag fractions, but also have low efficiency. The Kaon I and Kaon II categories, despite

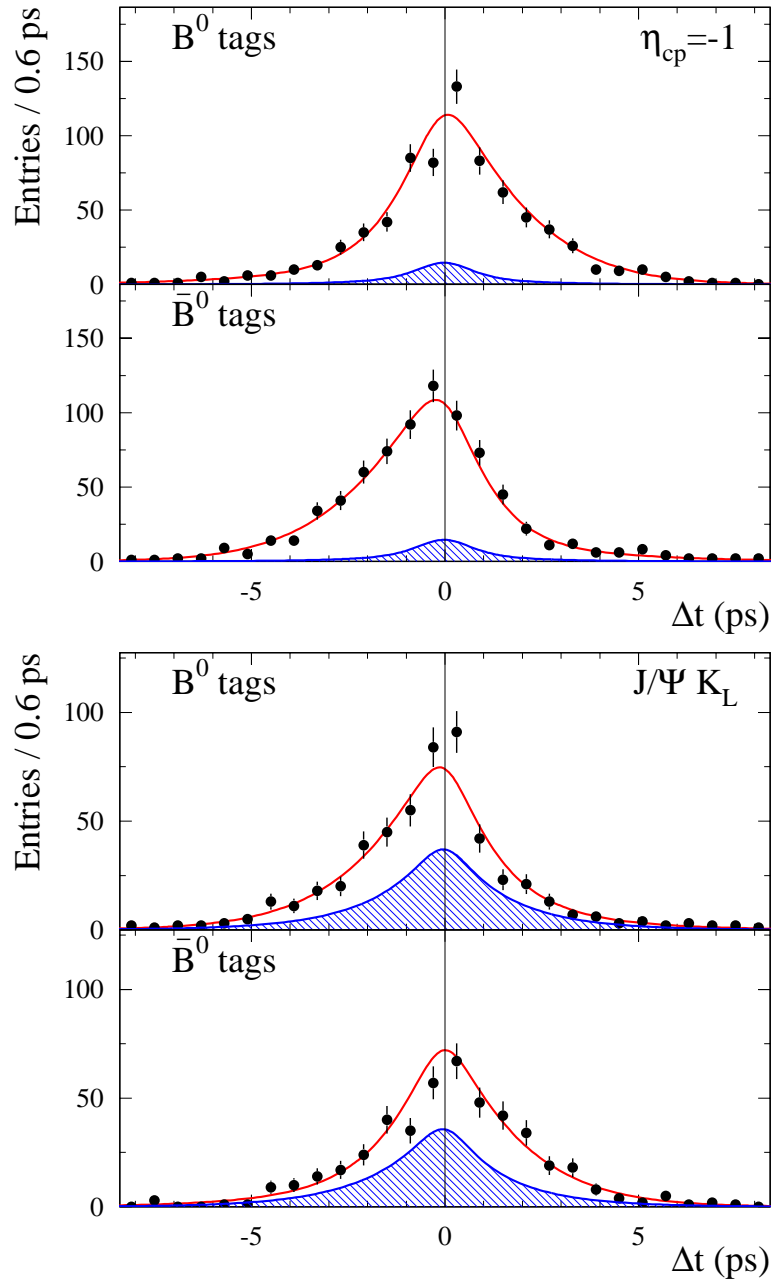


Fig. 72. Distribution of Δt for tagged events in the full CP sample at *BABAR*. The upper (lower) panel is the sum of B^0 (\bar{B}^0)-tagged events in the (a) $\eta_{CP} = -1$ and (b) $J/\psi K_L^0$ sample. In both cases, the data points are overlaid with the result from the global unbinned likelihood fit, projected on the basis of the individual signal and background probabilities, and event-by-event Δt resolutions, for candidates in the respective samples. Therefore, the curves correspond to $\sin 2\beta = 0.741$, rather than the fitted value obtained with the individual subsample. The probability-weighted Δt spectra of the background candidates obtained from the fit are indicated by the shaded areas.

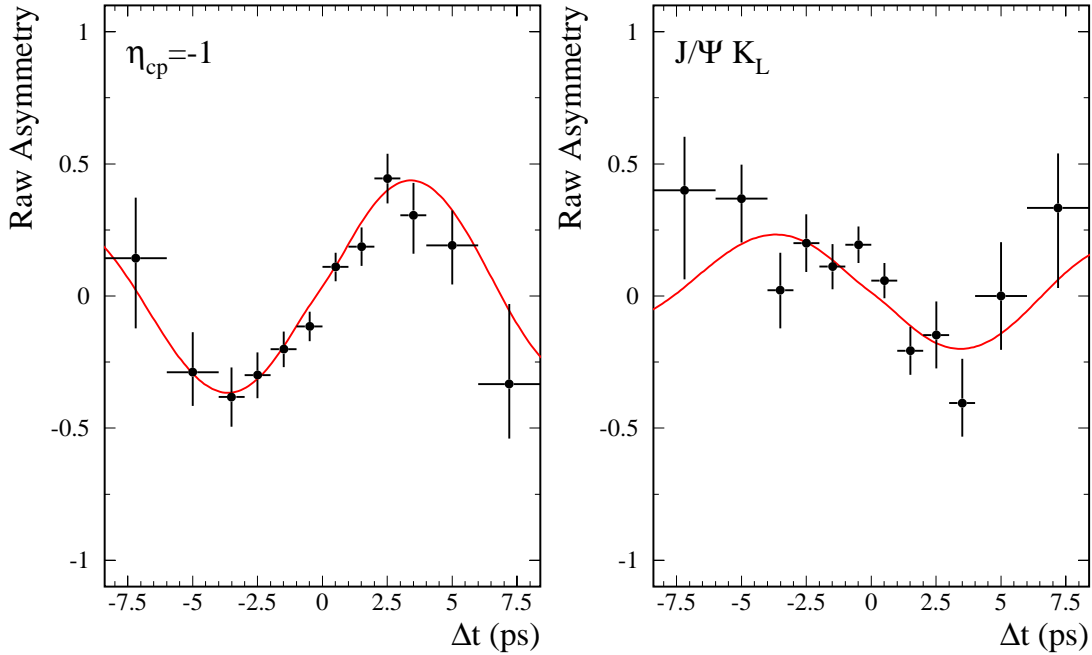


Fig. 73. Distribution of visible asymmetry as a function of Δt for tagged events in the full CP sample at *BABAR*. The upper (lower) panel is the sum of B^0 (\bar{B}^0)-tagged (a) $\eta_{CP} = -1$ and (b) $J/\psi K_L^0$ sample. In both cases, the data points are overlaid with the result from the global unbinned likelihood fit, projected on the basis of the individual signal and background probabilities, and event-by-event Δt resolutions, for candidates in the respective samples. Therefore, the curves correspond to $\sin 2\beta = 0.741$, rather than the fitted value obtained with the individual subsample.

having larger mistag fractions of (9.9%) and (20.9%), have a higher effective tagging efficiency; more than half of events are assigned to these categories. Altogether, lepton and kaon categories have an effective tagging efficiency $Q \approx 27.2\%$. The inclusive category increase the effective tagging efficiency by $\sim 0.9\%$ to an overall $Q = (28.1 \pm 0.7)\%$ (statistical error only).

A summary of the sources of systematic error on the $\sin 2\beta$ result is shown in Table 16. The dominant sources of systematic error are the uncertainties in the level, composition, and CP asymmetry of the background in the CP sample (0.023), the assumed parameterization of the Δt resolution function (0.017), due in part to residual uncertainties in the internal alignment of the vertex detector, and possible differences between the B_{flav} and B_{CP} mistag fractions (0.012). Most systematic errors are determined with data and will continue to decrease with additional statistics.

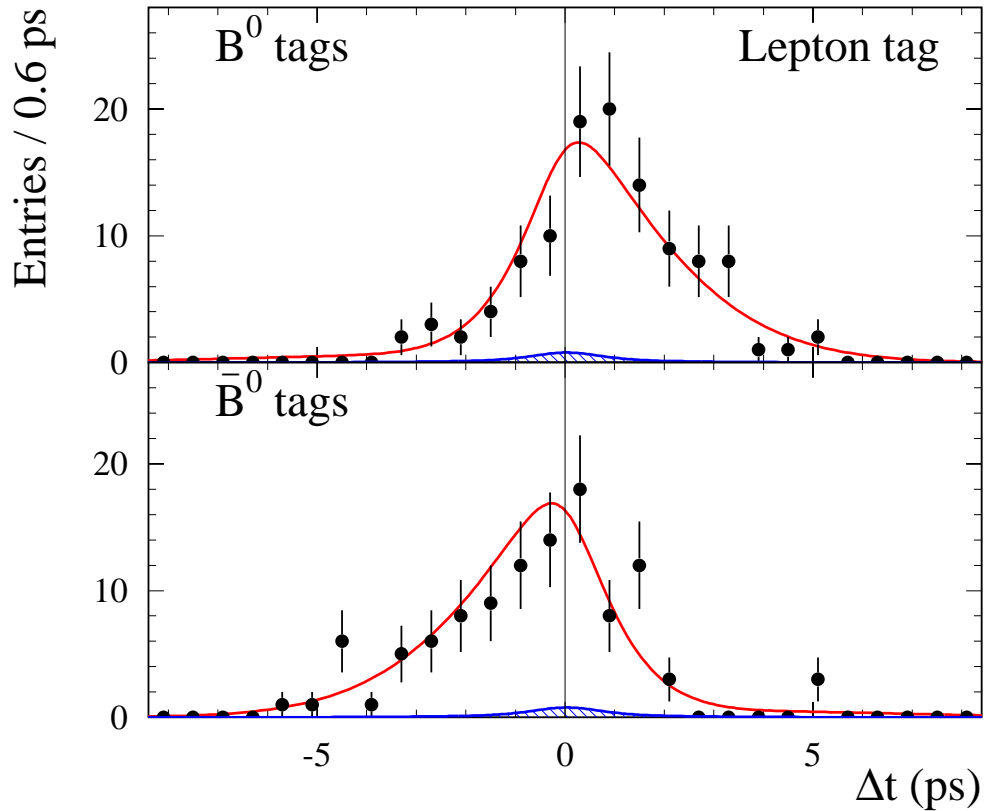


Fig. 74. Distribution of Δt for lepton-tagged events in the $\eta_{CP} = -1$ sample. The upper plot is for B^0 tags, while the lower is for \bar{B}^0 tags. [BABAR]

10.2 Results for $\sin 2\beta$ from Belle

Belle²⁸ employs a one-parameter maximum likelihood fit to the B_{CP} sample with $m_{ES} > 5.2 \text{ GeV}/c^2$ in order to extract a value of $\sin 2\beta$. The required dilution factors \mathcal{D}_i , Δt resolution parameters \hat{a}_i , and the background fractions and time distribution parameters are extracted with separate fits to flavor-eigenstate B_{flav} sample. The B_{flav} and B_{CP} samples are obtained with the techniques described in Section 4 in a data sample equivalent to 78 fb^{-1} . The mass distribution of candidates in the B_{CP} sample at Belle is shown in Figure 76 for the $\eta_{CP} = -1$ sample, while the $J/\psi K_L^0$ sample was shown earlier in Figure 45. The asymmetry measurement requires that there be a determination of Δt , which is based on the algorithms similar to those described in Section 5.

Although the underlying physics processes used for tagging are similar to those described in Section 7 for BABAR, the detailed implementation in the Belle analysis has some important differences. The basic organization of the track level and event level

Table 14. Number of events N_{tag} in the signal region after tagging and vertexing requirements, signal purity P , and results of fitting for CP asymmetries in the B_{CP} sample and in various subsamples, as well as in the B_{flav} and charged B control samples. Errors are statistical only. [BABAR]

Sample	N_{tag}	$P(\%)$	$\sin 2\beta$
$J/\psi K_S^0, \psi(2S)K_S^0, \chi_{c1}K_S^0, \eta_c K_S^0$	1506	94	0.76 ± 0.07
$J/\psi K_L^0$ ($\eta_f = +1$)	988	55	0.72 ± 0.16
$J/\psi K^{*0}$ ($K^{*0} \rightarrow K_S^0 \pi^0$)	147	81	0.22 ± 0.52
Full CP sample	2641	78	0.74 ± 0.07
$J/\psi K_S^0, \psi(2S)K_S^0, \chi_{c1}K_S^0, \eta_c K_S^0$ only ($\eta_f = -1$)			
$J/\psi K_S^0$ ($K_S^0 \rightarrow \pi^+ \pi^-$)	974	97	0.82 ± 0.08
$J/\psi K_S^0$ ($K_S^0 \rightarrow \pi^0 \pi^0$)	170	89	0.39 ± 0.24
$\psi(2S)K_S^0$ ($K_S^0 \rightarrow \pi^+ \pi^-$)	150	97	0.69 ± 0.24
$\chi_{c1}K_S^0$	80	95	1.01 ± 0.40
$\eta_c K_S^0$	132	73	0.59 ± 0.32
Lepton	220	98	0.79 ± 0.11
Kaon I	400	93	0.78 ± 0.12
Kaon II	444	93	0.73 ± 0.17
Inclusive	442	92	0.45 ± 0.28
B^0 tags	740	94	0.76 ± 0.10
\bar{B}^0 tags	766	93	0.75 ± 0.10
B_{flav} sample	25375	85	0.02 ± 0.02
B^+ sample	22160	89	0.02 ± 0.02

input is shown in Figure 77. Track-level look-up tables are used to identify slow pions from the D^{*+} transition, lambdas, kaons, and leptons, and to characterize the quality of the tag by the product of a continuous quality factor r , which varies from 0 to 1, and an integer tag type with $q = +1$ for a B^0 tag and $q = -1$ for a \bar{B}^0 tag. At the event level, the slow-pion and lepton with the largest r , and the lambda and kaon input with the largest $q \cdot r$ are input to an event-level look-up table to determine the B_{tag} flavor.

A comparison of the output variable from the event-level tagging decision is shown in Figure 78 for data and Monte Carlo simulation. The data points are for a sample of semileptonic B decays in the mode $\bar{B}^0 \rightarrow D^{*-} \ell^+ \nu$ and an hadronic B_{flav} sample.

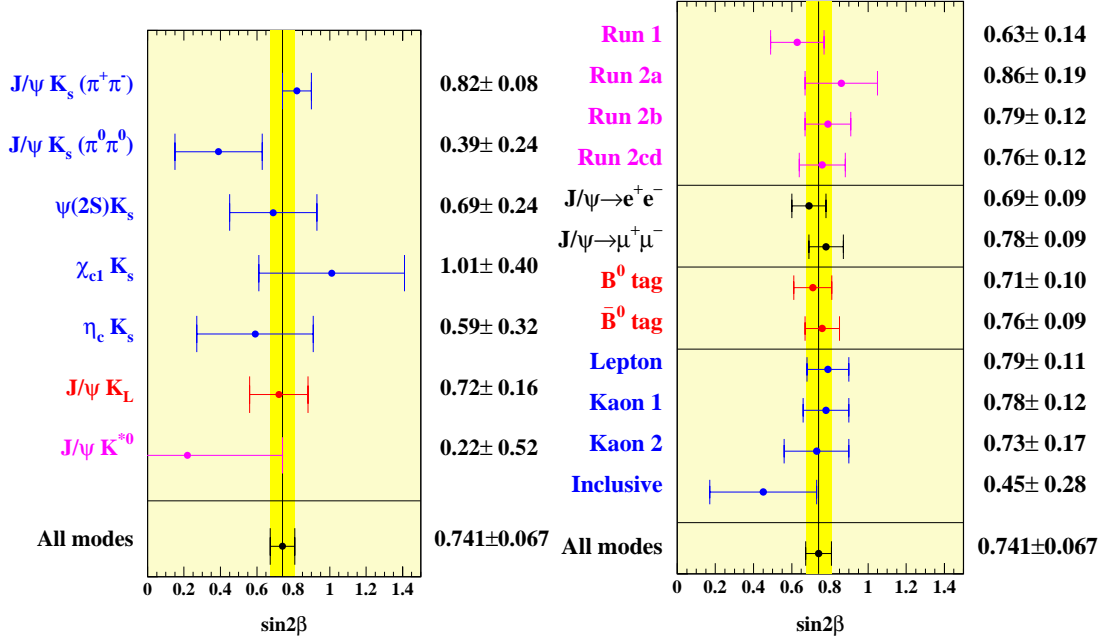


Fig. 75. Fitted value for $\sin 2\beta$ for individual channels (left) and other subsets (left) of the full CP sample [BABAR].

After determining the event level flavor information q and r , the tagging sample is divided into six discrete categories corresponding to six bins in r (0–0.25, 0.25–0.5, 0.5–0.625, 0.625–0.75, 0.75–0.875, 0.875–1.0). Since these are bins in r , a variety of physical tagging processes can contribute to each tagging category. The mistag rate in each category is determined from data, based on mixing fits to B_{flav} and $B^0 \rightarrow D^{*-} \ell^+ \nu$ samples. An example of fits to the time dependence of the mixing asymmetry in the $B^0 \rightarrow D^{*-} \ell^+ \nu$ sample is shown in Figure 79 for the six different tagging categories. Figure 80 shows that a linear relation between the measured dilution and the mean value of r for each tagging category.

The m_{ES} distribution for events in $\eta_{CP} = -1$ modes, separated into tagging categories, is shown in Figure 71. The signal and background probability assignments for each candidate in the $\eta_{CP} = -1$ sample is determined from these fits and the measured value for m_{ES} . While the background level in all four tagging categories is rather small, this is particularly so for the Lepton tags.

The value of $\sin 2\beta$ obtained by Belle from the unbinned maximum likelihood fit to the combined $\eta_{CP} = -1$, $\eta_{CP} = +1$, and $J/\psi K^{*0}$ CP samples is

$$\sin 2\beta = 0.719 \pm 0.074 \pm 0.035,$$

Table 15. Average mistag fractions w_i and mistag differences $\Delta w_i = w_i(B^0) - w_i(\bar{B}^0)$ at *BABAR*, as extracted for each tagging category i from the maximum-likelihood fit to the time distribution for the fully-reconstructed B^0 sample ($B_{\text{flav}} + B_{CP}$). The figure of merit for tagging is the effective tagging efficiency $Q_i = \epsilon_i(1 - 2w_i)^2$, where ϵ_i is the fraction of events with a reconstructed tag vertex that are assigned to the i^{th} category. ϵ_i is computed for the $\eta_{CP} = \pm 1$ samples as well as the combined B_{CP} and B_{flav} samples. Uncertainties are statistical only. The statistical error on $\sin 2\beta$ is proportional to $1/\sqrt{Q}$, where $Q = \sum Q_i$.

Tagging Category	Tagging Efficiency [%]	Mistag fraction w [%]	Mistag fraction difference Δw [%]	$Q = \epsilon(1 - 2w)$ [%]
Lepton	9.1 ± 0.2	3.3 ± 0.6	-0.9 ± 0.5	7.9 ± 0.3
Kaon I	16.7 ± 0.2	9.9 ± 0.7	-0.2 ± 0.5	10.7 ± 0.4
Kaon II	19.8 ± 0.3	20.9 ± 0.8	-2.7 ± 0.6	6.7 ± 0.4
Incl	20.0 ± 0.3	31.6 ± 0.8	-3.2 ± 0.6	0.9 ± 0.2
All	65.6 ± 0.5			28.1 ± 0.7

Table 16. Summary of contributions to the systematic error on $\sin 2\beta$ at *BABAR*.

Source	$\sigma(\sin 2\beta)$
Description of background events	0.017
<i>CP</i> content of background components	
Background shape uncertainties, peaking component	
Composition and <i>CP</i> content of $J/\psi K_L^0$ background	0.015
Δt resolution and detector effects	0.017
Silicon detector residual alignment	
Δt resolution model (GExp vs 3G, B_{flav} vs B_{CP})	
Mistag differences between B_{CP} and B_{flav} samples (MC)	0.012
Fit bias correction and MC statistics	0.010
Fixed lifetime and oscillation frequency	0.005
Total	0.033

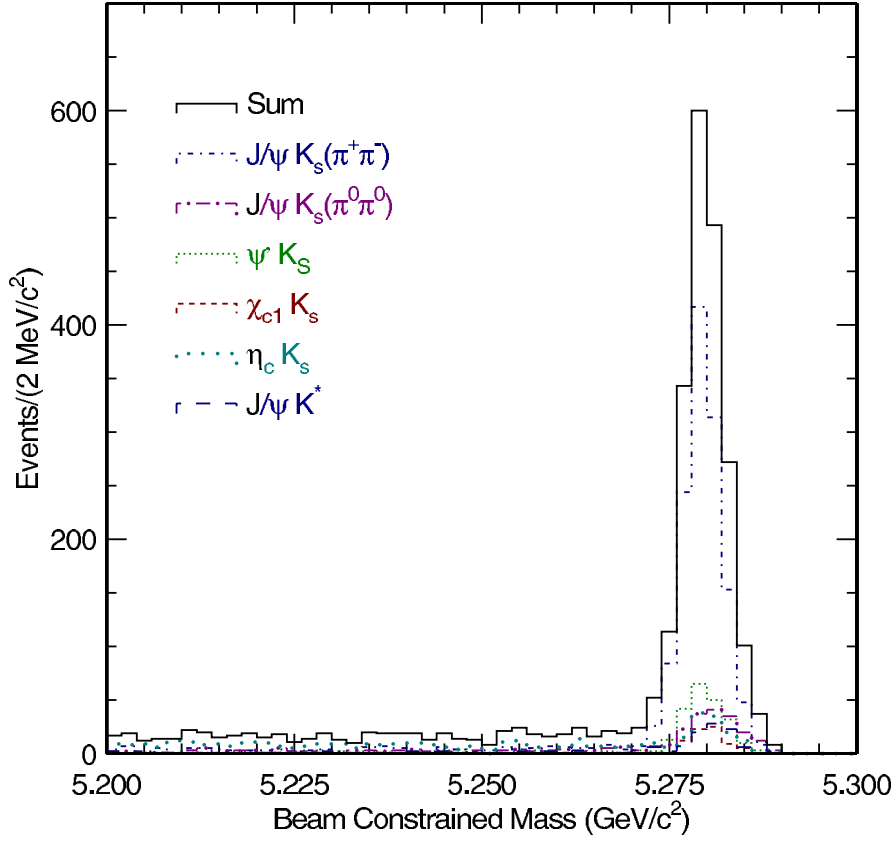


Fig. 76. Distribution of m_{ES} for the charmonium CP subsample [Belle]

where the first error is statistical and the second systematic. The distribution of events as a function of Δt for B^0 and \bar{B}^0 tags is shown in Figure 81 for the full B_{CP} sample, while the visible asymmetries are provided with fit projections in Figure 82 for the full CP sample, as well as the individual $\eta_{CP} = -1$ and $+1$ subsamples. The individual fitted values for $\sin 2\beta$

$$\begin{aligned} \sin 2\beta &= 0.716 \pm 0.083, & (\eta_{CP} = -1) \\ \sin 2\beta &= 0.78 \pm 0.17 & (\eta_{CP} = +1) \end{aligned}$$

are consistent. The systematic error on the combined result is dominated by uncertainties in the vertex reconstruction (0.022). Other significant contributions are the uncertainties on the mistag rates (0.015), the resolution function parameters (0.014), Monte Carlo tests of residual bias in the $\sin 2\beta$ fit (0.011), and the treatment of background for the $J/\psi K_L^0$ channel (0.010).

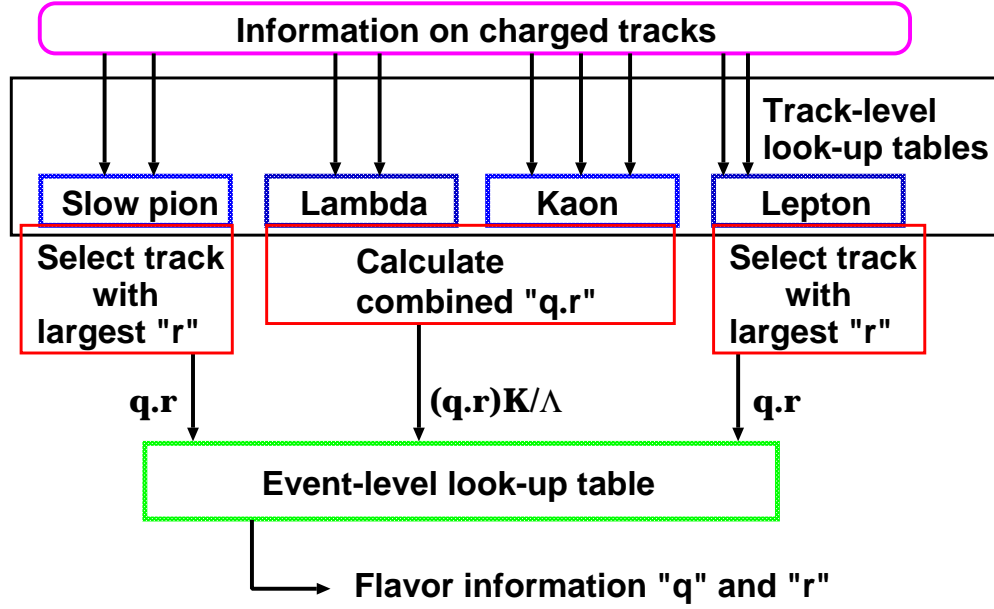


Fig. 77. Organization of track-level and event-level tagging information at Belle.

10.3 Validation studies and cross checks

One of the most compelling checks of the CP asymmetry analysis in data is the study of such asymmetries in the B_{flav} and B^+ control samples, where they are expected to be zero. For this check, the Δt resolution function parameters and the dilutions are fixed to the values obtained with the B_{flav} sample. The CP asymmetry and the fraction of prompt background (identical for each tagging category, as is the case for the fit to the CP data sample) are allowed to float. The observed Δt distributions for the B^0 - and \bar{B}^0 -tagged events in the B_{flav} sample is shown in Figure 83a, where good agreement is clearly visible. Figure 83b demonstrates that there is no visible asymmetry as a function of Δt . The fitted amplitude for the asymmetry in these channels is 0.02 ± 0.02 for both the B_{flav} and B^+ samples at *BABAR*. The corresponding distribution at Belle for a combined flavor sample with $B^0 \rightarrow D^{(*)-}\pi^+$, $D^{*-}\rho^+$, $J/\psi K^{*0}(K^+\pi^-)$, and $D^{*-}\ell^+\nu$ is shown in Figure 82d. The fitted asymmetry, $0.005 \pm 0.015(\text{stat})$, is again consistent with zero.

Control samples are also used to check the assumption that the Δt resolution function, which is primarily determined by the B_{flav} sample, can be applied to the charmonium decay modes in the CP sample. Figure 84 graphically compares the fitted Δt resolution function for the $B^+ \rightarrow D^{(*)}X$ control sample with that of the $B^+ \rightarrow c\bar{c}X$

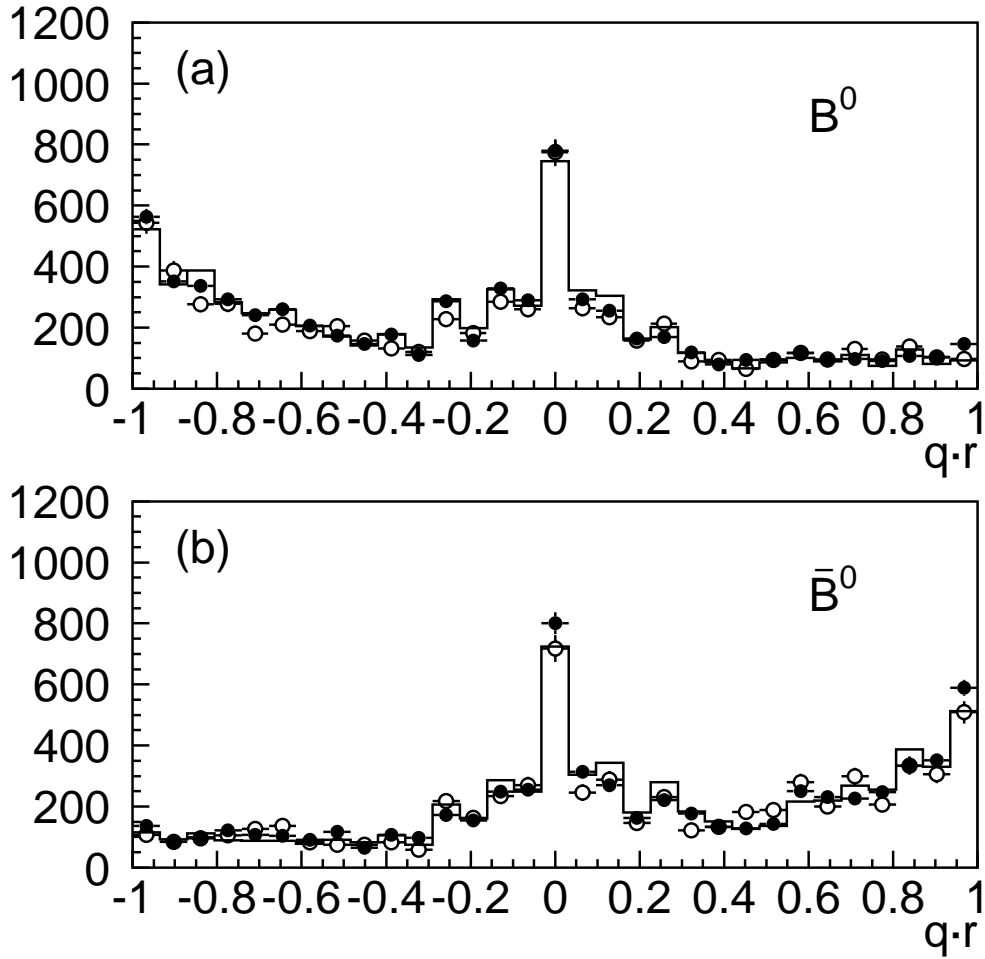


Fig. 78. Distribution of $q \cdot r$ for the B_{tag} decay in (a) B^0 and (b) \bar{B}^0 candidates in a $B^0 \rightarrow D^{*-}\ell^+\nu$ sample (closed circles), an hadronic B_{flav} sample (open circles), and Monte Carlo simulation (histogram).

control sample. A 1σ error envelope encompasses the fit to the $B^+ \rightarrow c\bar{c}X$ sample, which has five times fewer events. The level of agreement is acceptable. The same comparison between the $B^0 \rightarrow D^{(*)}X$ and $B^0 \rightarrow c\bar{c}X$ samples was inconclusive due to the low statistics of the $B^0 \rightarrow c\bar{c}X$ sample.

10.4 Fits results without assuming $|\lambda| = 1$

A more general description of the time evolution of neutral B decays to CP eigenstates contains a term proportional to $\cos \Delta m_d \Delta t$ (Eq. 9). The coefficient of the cosine term

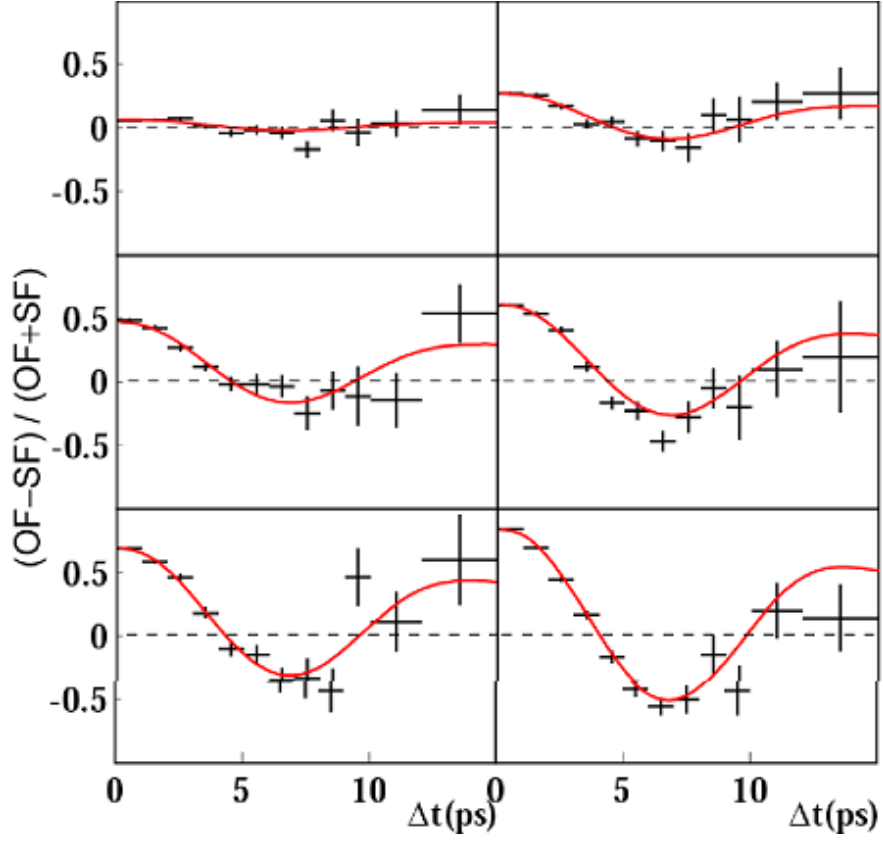


Fig. 79. Determination of the mistag rates in the six Belle tagging categories by means of a mixing fit to a tagged sample of $B^0 \rightarrow D^{*-}\ell^+\nu$ candidates.

is expected to be negligible in the Standard Model, where $|\lambda| = 1$. In order to search for a non-Standard Model effect, the $\eta_{CP} = -1$ sample is fit for $|\lambda|$ and $Im\lambda/|\lambda|$. The latter is equal to $\sin 2\beta$ if $|\lambda| = 1$. The $\eta_{CP} = -1$ sample has the advantage of having very little background, while the other CP modes have backgrounds that are both significantly larger and dominated by other B decay modes with possible direct CP contributions.

The sources of systematic error studies are similar to those described for the $\sin 2\beta$ fits. Detailed cross checks have also been performed, similar to those described in Section 10.3. In particular, large samples of parameterized simulation, as well as full Monte Carlo samples, have been used to verify the fitting procedure. The B_{flav} sample has also been used to demonstrate that no bias is introduced in the measurement. The relative normalization of the tagged events in the two flavors is in fact sensitive to the coefficient of the cosine term in Eq. 9, and therefore $|\lambda|$.

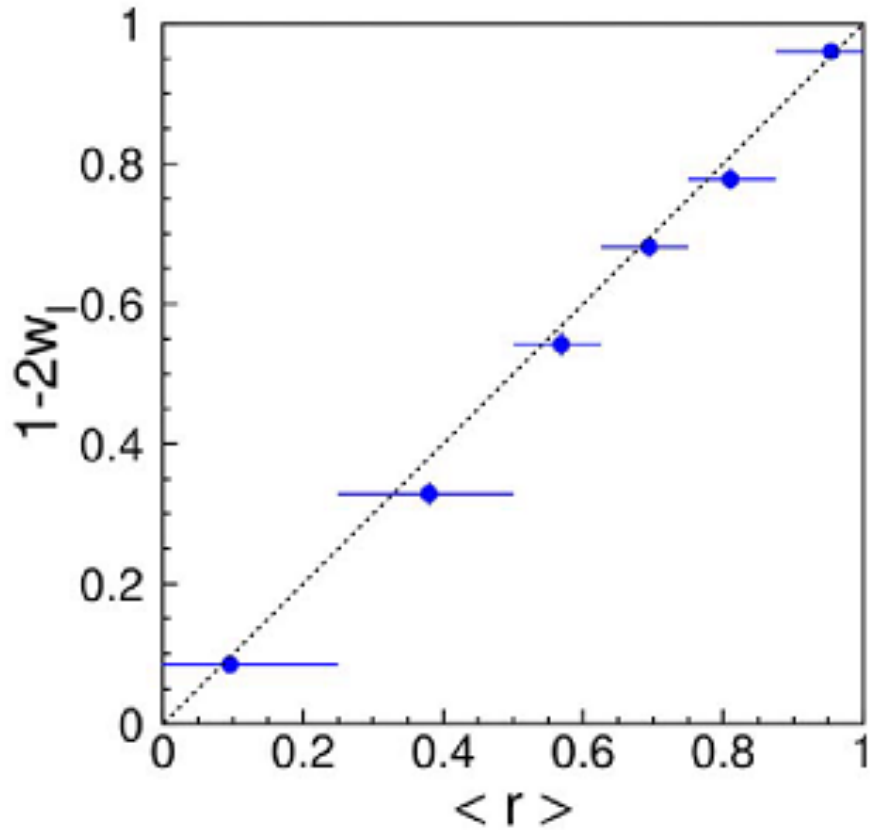


Fig. 80. Comparison of data measured dilution ($1 - 2w$) and the mean value of the tagging variable r for each of the six tagging categories.

Table 17. Summary of fits to the $\eta_{CP} = -1$ *BABAR* and Belle samples for $|\lambda|$.

Source	$ \lambda $	$Im\lambda/ \lambda $
<i>BABAR</i>	$0.948 \pm 0.051 \pm 0.017$	0.759 ± 0.074
Belle	$0.950 \pm 0.049 \pm 0.026$	0.720 ± 0.074

The fitted values for $|\lambda|$ and $Im\lambda/|\lambda|$ with the $CP = -1$ sample are summarized in Table 17. It is clear that on the basis of these measurements there is no evidence for direct CP violation in the $\eta_{CP} = -1$ sample and the value of $Im\lambda/|\lambda|$ is consistent with the result from the nominal CP fit with $|\lambda| = 1$.

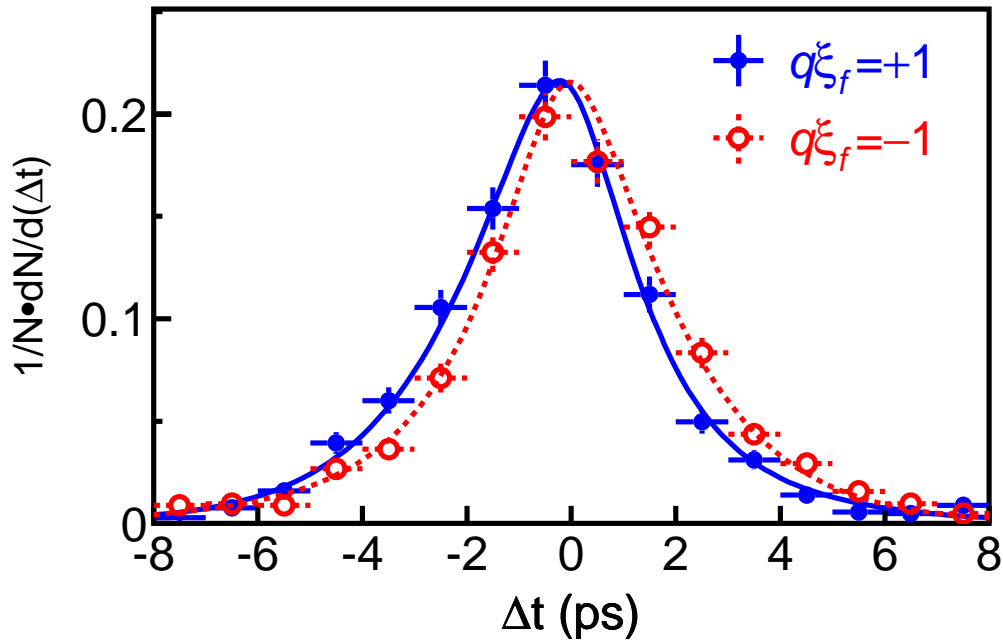


Fig. 81. Distribution of Δt for the full CP sample, where $\xi_f \equiv \eta_{CP}$ [Belle].

11 Conclusions and prospects

With the advent of the B Factories and, in particular, the rapid progress in time-integrated luminosity recorded by $BABAR$ and Belle, we have entered a period of experimental and theoretical renaissance in B physics. The data sets available as of the summer of 2002 approach 100 fb^{-1} for both experiments. This is five times larger than CLEO and will increase by another factor of five through about 2006. These data samples have been used to make measurements of B lifetimes and the B^0 - \bar{B}^0 mixing frequency Δm_d at a level of precision comparable to the PDG2000 world averages for these quantities. Thus, the measurements contribute significantly to the precision of the determined value for τ_B and Δm_d , two of the fundamental parameters constraining our knowledge of the CKM matrix. These measurements remain dominated by statistical errors that will improve with more data that is already available. In addition, these studies confirm that the Belle and $BABAR$ have a good understanding of B reconstruction, flavor tagging, and Δt resolution the B_{rec} samples that are closely related to the time-dependent CP asymmetry measurements.

In the summer of 2001, $BABAR$ and Belle presented the first observation of CP violation outside the neutral kaon system. These studies have evolved a year later into

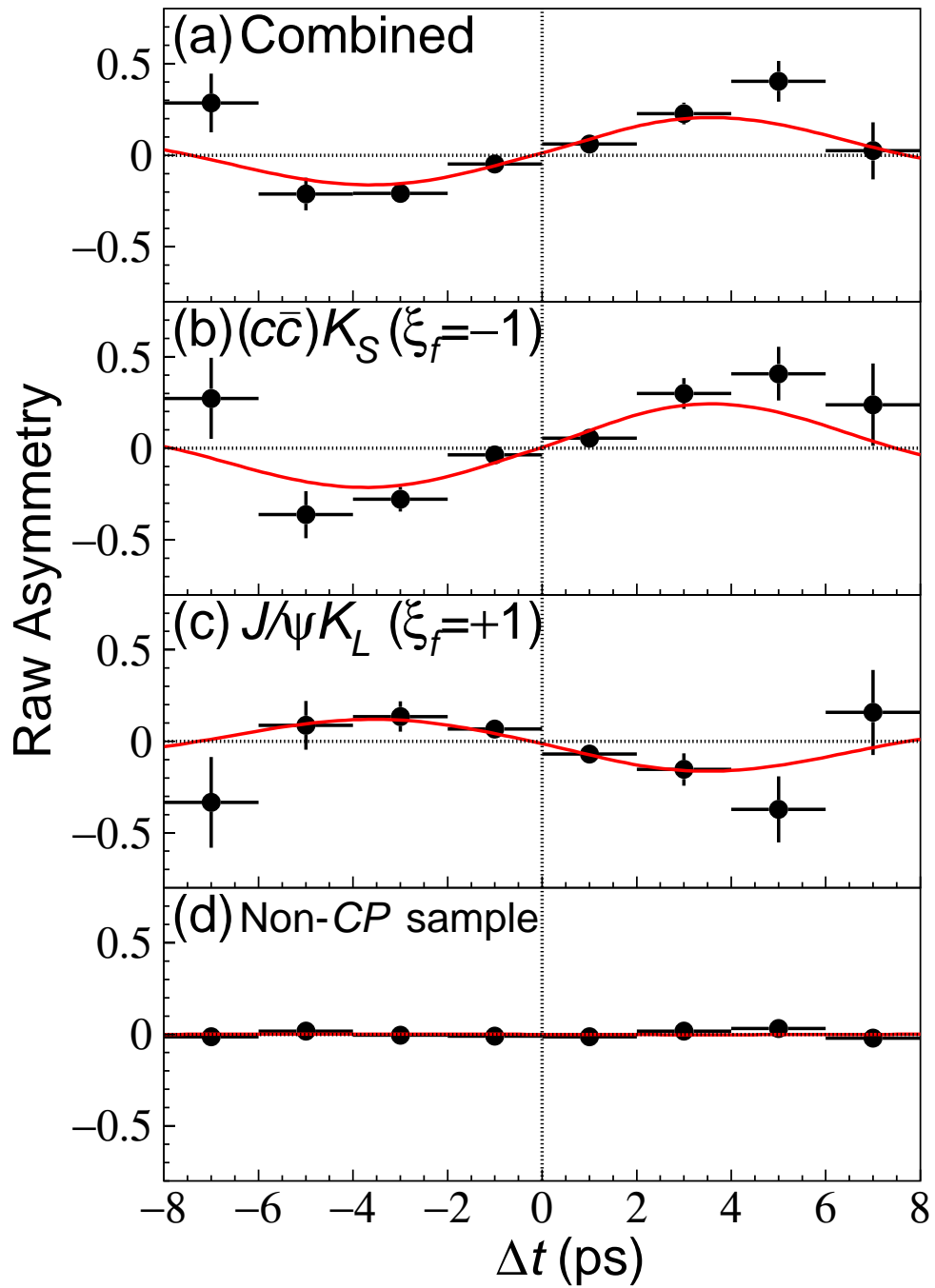


Fig. 82. Raw asymmetry distributions for (a) the full CP sample, (b) the $\eta_{CP} = -1$ subsample, (c) the $J/\psi K_L^0$ subsample, and (d) B_{flav} samples [Belle].

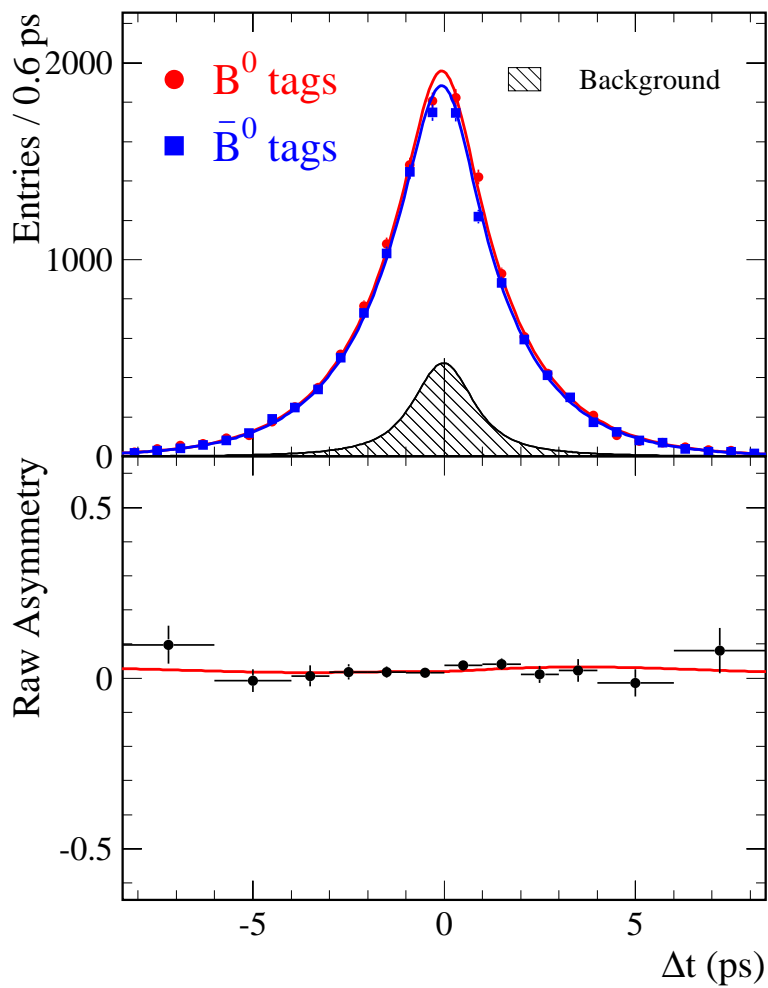


Fig. 83. a) Distribution in Δt for B^0 - and \bar{B}^0 -tagged and b) observed asymmetry for events in the flavor-eigenstate B^0 sample. The projections of the likelihood fit for the B^0 - and \bar{B}^0 -tagged samples are shown in a) as the overlapping solid lines. [BABAR]

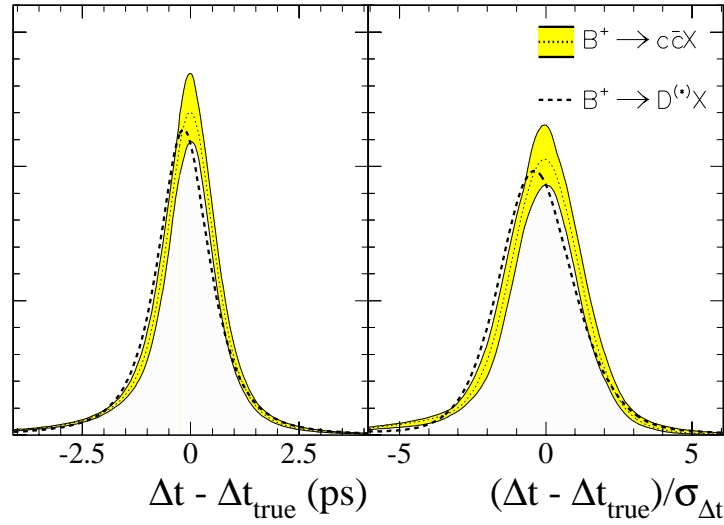


Fig. 84. Comparison of the fitted Δt resolution obtained with the data control samples $B^+ \rightarrow D^{(*)}X$ and $B^+ \rightarrow c\bar{c}X$, showing the fitted distribution for a) $\delta_t = \Delta t - \Delta t_{\text{true}}$ and b) the normalized difference $\delta_t/\sigma_{\Delta t}$. The one sigma error envelope from the fit to the $B^+ \rightarrow c\bar{c}X$ sample (shaded region), overlaps the central value for the five-times larger $B^+ \rightarrow D^{(*)}X$ sample (dashed line).

precision determinations of $\sin 2\beta$, as has been shown in detail in these lectures. The present world average value is found to be

$$\sin 2\beta = 0.734 \pm 0.055, \quad (39)$$

a level of precision better than the predicted range from indirect constraints. Figure 85 shows the history of $\sin 2\beta$ measurements. In part, the precision is the result of ongoing improvements to the analyses at *BABAR* and *Belle*, as shown in Figure 86. The observed value for $\sin 2\beta$ is currently limited by the size of the CP sample, allowing for substantial improvement as more data is recorded in the next few years. Searches for direct CP violation in charmonium decays are consistent with the Standard Model expectation of $|\lambda| = 1$.

As already noted in Section 1, measurements of CP asymmetries in B decays to charmonium can be used to constrain, with little theoretical ambiguity, the parameters of the CKM matrix. In the Standard Model with three families, the CKM matrix V^3 incorporates three real parameters and one phase δ generating CP violation if $\delta \neq 0$ or π . The Wolfenstein parameterization¹⁰ of V takes advantage of the observed hierarchy in the matrix elements in terms of the expansion parameter $\lambda_{CKM} = |V_{us}|$. The remaining

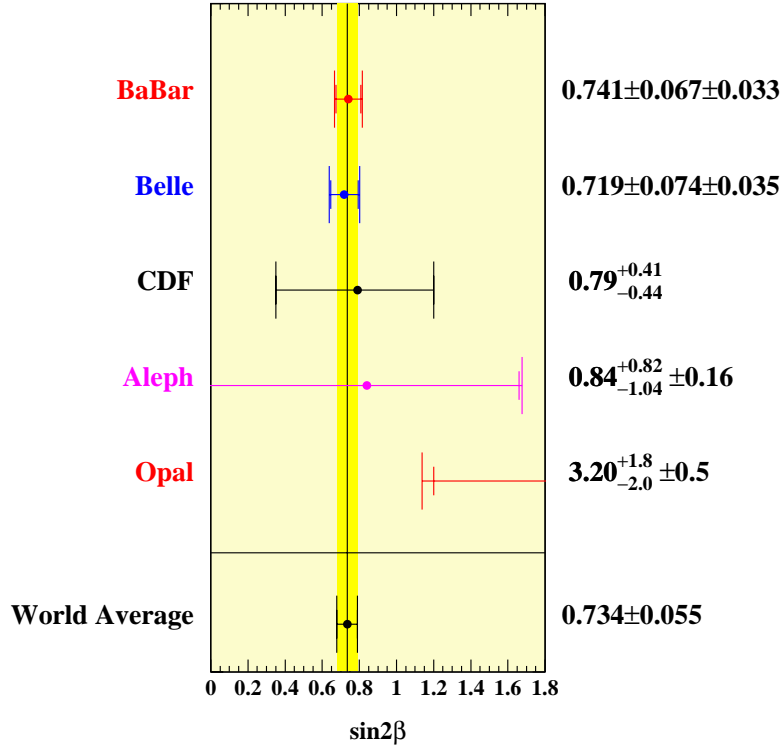


Fig. 85. Comparison of existing measurements of $\sin 2\beta$ and present world average result.³⁸

parameters in this representation are denoted A , ρ , and η , where CP violation requires $\eta \neq 0$.

The parameter λ_{CKM} is determined from semileptonic kaon decays and nuclear β decays. Semileptonic B meson decays to charm are used to determine the parameter A . Constraints on ρ and η are obtained from CP violation in mixing in the kaon sector $|\epsilon_K|$, the ratio $|V_{ub}/V_{cb}|$, and the oscillation frequency Δm_d for $B^0-\bar{B}^0$ mixing. The oscillation frequency Δm_s has not been measured, since $B_s^0-\bar{B}_s^0$ mixing has not been observed yet. However, the observed amplitude spectrum $\mathcal{A}(\Delta m_s)$ improves the constraints on ρ and η . Together, these measurements provide indirect constraints on $\sin 2\beta$.

Our overall knowledge of the CKM parameters is limited by the relatively large uncertainties in some of the theoretical quantities, mainly due to non-perturbative QCD effects. In particular, the constraints on ρ and η suffer from theoretical and systematic uncertainties in the determination of $|V_{ub}/V_{cb}|$ and from theoretical uncertainties in QCD parameters entering the prediction of $|\epsilon_K|$, Δm_d , and Δm_s . Recent analy-

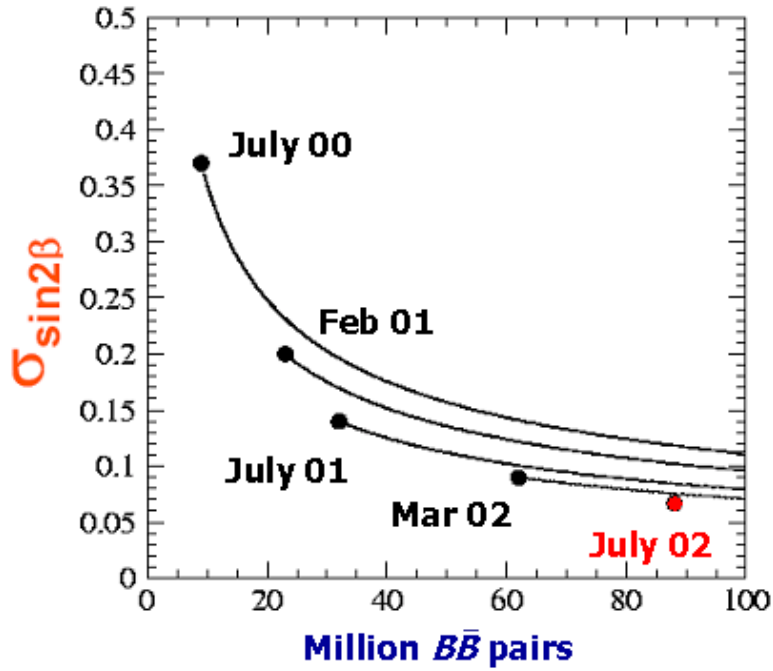


Fig. 86. Comparison of $1/\sqrt{N}$ scaling of reported errors on $\sin 2\beta$ versus actually achieved errors for a given sample size [BABAR].

ses constraining the CKM matrix have been performed with different statistical approaches.^{42–48} They mainly differ in the treatment of theoretical uncertainties and also in the choice of the input values and their errors.

Due to the four-fold ambiguity in the value of β obtained from the $\sin 2\beta$ measurement, there are four allowed regions in the ρ - η plane. One of these regions is found to be in agreement with the allowed ρ - η region obtained from CKM fits within the Standard Model. Figure 87, taken from Ref.,⁴² shows the direct measurements and the indirect constraints in the $\bar{\rho} - \bar{\eta}$ plane in terms of the renormalized parameters $\bar{\rho} = \rho(1 - \lambda_{CKM}^2/2)$ and $\bar{\eta} = \eta(1 - \lambda_{CKM}^2/2)$. The contributions of the individual measurements $|\epsilon_K|$, $|V_{ub}/V_{cb}|$, Δm_d , and Δm_s ⁴² are indicated, as well as the allowed region if all the constraints are considered simultaneously. Overlaid as the diagonally-hatched area are the regions corresponding to one and two times the one-standard-deviation experimental uncertainty on the world-average $\sin 2\beta$ measurement.

It should be emphasized that, beyond being a direct constraint on β , the measurement of $\sin 2\beta$ differs qualitatively in its interpretation from the indirect constraints on β obtained from $|\epsilon_K|$, $|V_{ub}/V_{cb}|$, Δm_d , and eventually Δm_s . For $\sin 2\beta$, the size of

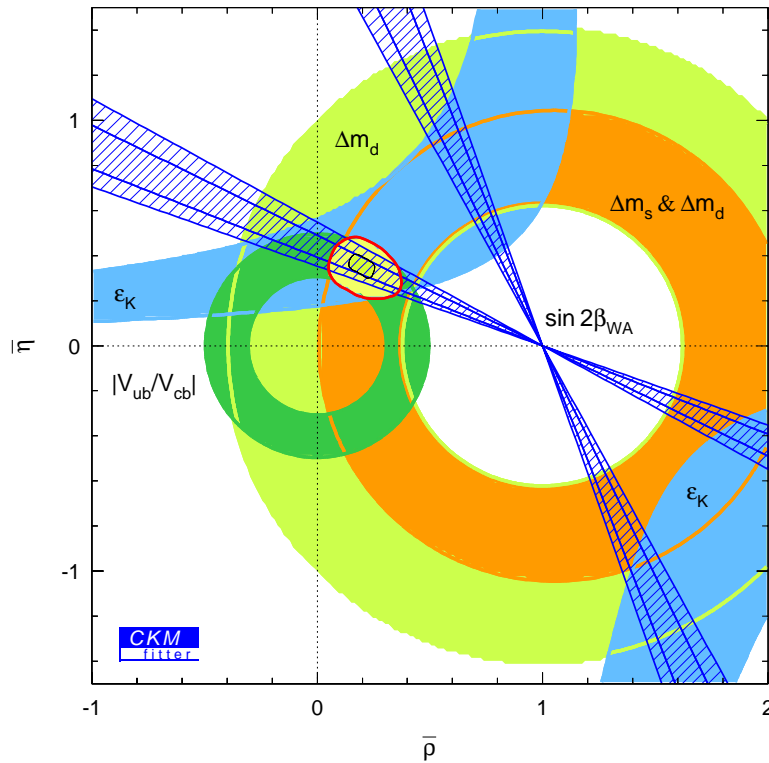


Fig. 87. Present indirect constraints on the position of the apex of the Unitarity Triangle in the $(\bar{\rho}, \bar{\eta})$ plane, not including the *BABAR* and *Belle* measurements of $\sin 2\beta$. The fitting procedure is described in Ref.⁴² The world result $\sin 2\beta = 0.734 \pm 0.055$ is represented by diagonally hatched regions, corresponding to one and two statistical standard deviations. The individual indirect constraints lie between the pairs of solid lines that are connected by the double-ended arrows with labels.

the allowed domain is determined by well-defined experimental uncertainties that are predominantly statistical in origin, while in contrast the region allowed by the indirect measurements is mostly defined by theoretical uncertainties, which makes a statistical interpretation difficult.

The current experimental uncertainty on $\sin 2\beta$ has now reached a level of precision that offers significant constraint on the Standard Model. Over the next few years there will continue to be substantial improvements in precision of the $\sin 2\beta$ determination, including measurements for other final states in which CP -violating asymmetries are proportional to $\sin 2\beta$. One scenario for the evolution of the PEP-II instantaneous and integrated luminosity is shown in Figure 88, based on funded collider improvements.

Comparable plans are underway at KEKB. These plans could lead to data samples in excess of 1 ab^{-1} towards the end of the decade. An example of projected errors on $\sin 2\beta$ for these larger data samples is provided in Table 18. The main $J/\psi K_s^0$ channel will reach the 3% level, with systematic errors still only half the size of statistical errors. However, channels such as $D^* D^*$ will not be at a level to allow a definitive test of the level of agreement on $\sin 2\beta$.

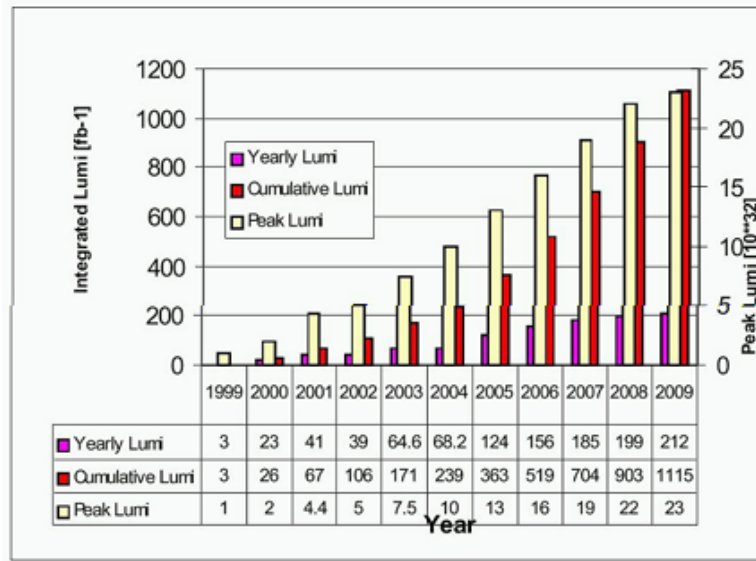


Fig. 88. Projected peak and integrated luminosity for the PEP-II B Factory, based on funded program of improvements to the collider. Comparable plans for KEKB are also underway.

Table 18. Estimates of projected statistical and systematic errors on $\sin 2\beta$ CP asymmetry measurements at $BABAR$.

Channel	56 fb^{-1}	0.5 ab^{-1}	2.0 ab^{-1}	10.0 ab^{-1}
$J/\psi K_s^0$	0.11/0.04	0.037/0.015	0.018/0.015	0.009/0.015
Charmonium	0.09/0.04	0.030/0.015	0.015/0.015	0.007/0.015
$D^* D^*$	0.45/0.06	0.15/0.04	0.08/0.03	0.034/0.03

Beyond this, studies of time-dependent asymmetries in modes involving $b \rightarrow u$ transitions have already begun^{49,50} and may provide additional constraints, although

here the interpretation in terms of $\sin 2\alpha$ from the Unitarity Triangle is likely to be made difficult due to significant penguin contributions. Nevertheless, these measurements and many other studies of time-dependent CP asymmetries will be able to directly test the validity of the CKM picture as the origin for the observed CP violation in neutral B decays.

References

- [1] J.H. Christenson *et al.*, Phys. Rev. Lett. **13**, 138 (1964); NA31 Collaboration, G.D. Barr *et al.*, Phys. Lett. **317**, 233 (1993); E731 Collaboration, L.K. Gibbons *et al.*, Phys. Rev. Lett. **70**, 1203 (1993).
- [2] A.D. Sakhorov, Pisma Zh. Eksp. Teor. Fiz. **5**, 32 (1967); Traduction JETP Lett. **5**, 24 (1967).
- [3] N. Cabibbo, Phys. Rev. Lett. **10**, 531 (1963); M. Kobayashi and T. Maskawa, Prog. Th. Phys. **49**, 652 (1973).
- [4] See, for instance, “Overall determinations of the CKM matrix”, Section 14 in “The *BABAR* physics book”, P. H. Harrison and H. R. Quinn, eds., SLAC-R-504 (1998), and references therein.
- [5] For an introduction to CP violation, see, for instance, “A CP violation primer”, Section 1 in “The *BABAR* physics book”, op. cit.,⁵ and references therein.
- [6] M.B. Gavela *et al.*, Mod. Phys. Lett. **A9**, 795 (1994) and Nucl. Phys. **B340**, 382 (1994); P. Huet and E. Sather, Phys. Rev. **D51**, 379 (1995).
- [7] S.W.Herb *et al.*, Phys. Rev. Lett. **39**, 252 (1977).
- [8] MAC Collaboration, E.Fernandez *et al.*, Phys. Rev. Lett. **51**, 1022 (1983).
- [9] Mark II Collaboration, N.S.Lockyer *et al.*, Phys. Rev. Lett. **51**, 1316 (1983).
- [10] L. Wolfenstein, Phys. Rev. Lett. **51**, 1945 (1983).
- [11] ARGUS Collaboration, H.Albrecht *et al.*, Phys. Lett. **B 192**, 245 (1987).
- [12] A.B. Carter and A.I. Sanda, Eur. Phys. Jour. **C 45**, 952 (1980); A.B. Carter and A.I. Sanda, Phys. Rev. **D 23**, 1567 (1981); I.I. Bigi and A.I. Sanda, Nucl. Phys. **B 193**, 85 (1981).
- [13] C. Jarlskog, in *CP Violation*, C. Jarlskog ed., World Scientific, Singapore (1988).

- [14] G.J. Feldman *et al.*, Proceedings of the Summer Study on High Energy Physics in the 1990s, p.561-571, World Scientific, 1988.
- [15] CUSB Collaboration, T. Böhringer *et al.*, Phys. Rev. Lett. **44**, 1111 (1980); G. Finchiario *et al.*, Phys. Rev. Lett. **45**, 222 (1980).
- [16] I.I. Bigi, Nuovo Cim. **109A**, 713 (1996).
- [17] M. Neubert, C.T. Sachrajda, Nucl. Phys. **B483**, 339 (1997).
- [18] Particle Data Group, D. E. Groom *et al.*, Eur. Phys. Jour. C **15**, 1 (2000).
- [19] UA1 Collaboration, C. Albajar *et al.*, Phys. Lett. **B186**, 247 (1987).
- [20] Throughout this paper, charged and neutral flavor-eigenstate decay modes also imply their charge conjugate.
- [21] *BABAR* Collaboration, B. Aubert *et al.*, Phys. Rev. Lett. **87**, 241801 (2001).
- [22] Belle Collaboration, K. Abe *et al.*, Phys. Lett. B **538**, 11 (2002).
- [23] *BABAR* Collaboration, B. Aubert *et al.*, Phys. Rev. Lett. **87**, 201803 (2001).
- [24] Belle Collaboration, K. Abe *et al.*, Phys. Rev. Lett. **88**, 171801 (2002).
- [25] *BABAR* Collaboration, B. Aubert *et al.*, Phys. Rev. Lett. **88**, 221802 (2002) and Phys. Rev. D **66**, 032003 (2002).
- [26] Belle Collaboration, K. Abe *et al.*, Phys. Lett. B **542**, 207 (2002).
- [27] *BABAR* Collaboration, B. Aubert *et al.* Phys. Rev. Lett. **86**, 2515 (2001); Phys. Rev. Lett. **87**, 091801 (2001); Phys. Rev. D **66**, 032003 (2002); and Phys. Rev. Lett. **89**, 201802 (2002).
- [28] Belle Collaboration, K. Abe *et al.* Phys. Rev. Lett. **86**, 2509 (2001); Phys. Rev. Lett. **87**, 091802 (2001); Phys. Rev. D **66**, 032007 (2002); and Phys. Rev. D **66**, 071192(R) (2002).
- [29] “PEP-II: An Asymmetric *B* Factory”, Conceptual Design Report, SLAC-418, LBL-5379 (1993).
- [30] “KEKB *B*-Factory Design Report”, KEK Report 95-7 (1995).
- [31] *BABAR* Letter of Intent for the study of *CP* violation and heavy flavor physics at PEP-II, D. Boutigny *et al.*, ed. D.B. MacFarlane and R. Schindler, SLAC-R-443 (1994); *BABAR* Technical Design Report, D. Boutigny *et al.*, ed. D.B. MacFarlane, SLAC-R-457 (1995).

- [32] Belle Letter of Intent, M.T. Cheng *et al.*, KEK Report 94-2 (1994); Belle Technical Design Report, KEK Report 95-1 (1995).
- [33] *BABAR* Collaboration, B. Aubert *et al.*, Nucl. Instr. Meth. A **479**, 1 (2002).
- [34] *BABAR* Collaboration, B. Aubert *et al.*, Nucl. Instr. Meth. A **479**, 117 (2002).
- [35] G.C. Fox and S. Wolfram, Phys. Rev. Lett. **41**, 1581 (1978).
- [36] ARGUS Collaboration, H. Albrecht *et al.*, Phys. Lett. **B241**, 278 (1990).
- [37] “GEANT, Detector Description and Simulation Tool”, CERN program library long writeup W5013 (1994).
- [38] Other results have been reported by OPAL³⁹ ($\sin 2\beta = 3.2_{-2.0}^{+1.8} \pm 0.5$) and CDF⁴⁰ ($\sin 2\beta = 0.79_{-0.44}^{+0.41}$). See also ALEPH’s preliminary result⁴¹ $\sin 2\beta = 0.93_{-0.88-0.24}^{+0.64+0.36}$.
- [39] OPAL Collaboration, K. Ackerstaff *et al.*, Eur. Phys. Jour. C **5**, 379 (1998).
- [40] CDF Collaboration, T. Affolder *et al.*, Phys. Rev. **D61**, 072005 (2000).
- [41] ALEPH Collaboration, ALEPH 99-099 CONF 99-54 (1999).
- [42] A. Höcker, H. Lacker, S. Laplace and F. Le Diberder, Eur. Phys. Jour. C **21**, 225 (2001).
- [43] S. Plaszczynski, M.-H. Schune, “Overall determination of the CKM matrix,” LAL-99-67, hep-ph/9911280; “*BABAR* physics book,” Chapter 14, SLAC-R-504, 1998.
- [44] M. Ciuchini *et al.*, JHEP 0107:013 (2001).
- [45] M. Bargiotti *et al.*, Riv. Nuovo Cim. **23N3**, 1 (2000).
- [46] P. Faccioli, Nucl. Instr. Meth. A **462**, 313 (2001).
- [47] D. Atwood and A. Soni, Phys. Lett. B **516**, 39 (2001).
- [48] A. Ali and D. London, Eur. Phys. Jour. C **18**, 665 (2001).
- [49] *BABAR* Collaboration, B. Aubert *et al.*, Phys. Rev. D **65**, 051502(R) (2002) and Phys. Rev. Lett. **89**, 281802 (2002).
- [50] Belle Collaboration, K. Abe *et al.*, Phys. Rev. Lett. **89**, 071801 (2002).